



Max-Planck-Institut für Intelligente Systeme
(ehemals Max-Planck-Institut für Metallforschung)
Stuttgart

Microstructure development during phase transformations: simulations and experiments

Eric A. Jäggle

Dissertation
an der
Universität Stuttgart

Bericht Nr. 237
Oktober 2011

Microstructure development during phase transformations: simulations and experiments

Von der Fakultät Chemie der Universität Stuttgart zur Erlangung der
Würde eines Doktors der Naturwissenschaften (Dr. rer. nat.)
genehmigte Abhandlung

Vorgelegt von
Eric A. Jägle
aus Tuttlingen

Hauptberichter
Mitberichter
Prüfungsausschussvorsitzender

Prof. Dr. Ir. E. J. Mittemeijer
Prof. Dr.-Ing. C. Mieke
Prof. Dr. T. Schleid

Tag der mündlichen Prüfung

05.10.2011

MAX-PLANCK-INSTITUT FÜR INTELLIGENTE SYSTEME
(EHEMALS MAX-PLANCK-INSTITUT FÜR METALLFORSCHUNG)
INSTITUT FÜR MATERIALWISSENSCHAFT DER UNIVERSITÄT STUTTGART

2011

Ever tried. Ever failed. No matter.
Try again. Fail again.
Fail better.

Samuel Beckett

Contents

1	Introduction	11
1.1	Interplay of the phase transformations and the microstructure of solids	11
1.1.1	Step 1: Modelling the phase-transformation mechanism	12
1.1.2	Step 2: Predicting the product microstructure	14
1.1.3	Scope of the thesis	15
1.2	Kinetic models	16
1.2.1	The classical JMAK and JMAK-like models; the modular approach	16
1.2.2	Beyond JMAK models; the case of non-random nucleation	18
1.3	Mesoscopic simulation methods	19
1.4	Investigated phase transformations	22
1.5	Organisation of the thesis	23
2	Predicting microstructures from phase transformation kinetics	25
2.1	Introduction	25
2.2	Modelling of Grain-Size Distributions	26
2.2.1	Methods for Microstructure Simulation	26
2.2.2	Method employed	28
2.2.3	Simulation Parameters and Validation of the Algorithm	32
2.3	Results and Discussion	33
2.3.1	Isochronal Heating	33
2.3.2	Isochronal Cooling	37
2.3.3	Discussion	40
2.4	Conclusions	42
3	Simulation of the kinetics of GBN phase transformations	45
3.1	Introduction	45
3.2	Kinetic Models	45
3.3	Simulation Method	47
3.4	Simulation Results	48
3.5	Discussion	50
3.6	Conclusions	52

4	Modelling of the kinetics of GBN phase transformations	53
4.1	Introduction	53
4.2	Kinetic Models	55
4.2.1	Random nucleation	55
4.2.2	Grain-boundary nucleation	56
4.2.3	Kinetic parameters	59
4.3	Geometric Simulations	60
4.3.1	Simulation Principle	60
4.3.2	Construction of the parent microstructure	61
4.4	Results and evaluation	61
4.4.1	General assessment of model appropriateness	63
4.4.2	Role of the ratio of the parent and product grain sizes	64
4.4.3	Role of the parent microstructure	66
4.4.4	Role of the type of GBN transformation kinetics	68
4.4.5	Simultaneous fitting of kinetic models to a set of non-isothermal transformation runs	70
4.5	General discussion	72
4.6	Conclusions	74
5	Phase-transformation kinetics: atomistic and mesoscopic simulations	77
5.1	Introduction	77
5.2	The modular model for transformation kinetics	78
5.3	Atomistic Simulations	80
5.3.1	Simulation algorithm	80
5.3.2	The activation energy for growth	82
5.3.3	Influence of the excess volume in the parent/product interface on interface migration	83
5.4	Mesoscopic microstructure simulations	85
5.4.1	Simulation algorithm	85
5.4.2	Prediction of grain-size distributions	87
5.4.3	Effects of non-random nucleation	91
5.5	Conclusions	94
6	Recrystallisation of copper: experimental evidence	97
6.1	Introduction	97
6.2	Literature survey	98
6.2.1	Kinetics	98
6.2.2	Microstructure	101
6.3	Experimental details and simulation method	103
6.3.1	Specimen preparation	103

6.3.2	Calorimetry	104
6.3.3	EBSD	105
6.3.4	Simulations	107
6.4	Results and evaluation	109
6.4.1	Calorimetry	109
6.4.2	EBSD	111
6.5	General Discussion	119
6.6	Conclusions	124
6.6.1	Recrystallisation of copper	124
6.6.2	Recrystallisation in general	125
7	Recrystallisation of copper: simulations	127
7.1	Introduction	127
7.2	Experimental results	129
7.3	Employed nucleation and growth models	131
7.3.1	“Nucleation”	131
7.3.2	Growth	133
7.4	Simulation method	135
7.4.1	Setup of the deformed microstructure	135
7.4.2	Cellular automaton algorithm	139
7.4.3	Nucleation	140
7.4.4	Growth	141
7.5	Results	143
7.5.1	Growth kinetics: anisotropic growth due to misorientation- dependent grain-boundary mobility	143
7.5.2	Influence of the subgrain-size distribution, the subgrain- energy distribution and the nucleation model	150
7.6	Concluding Discussion	157
7.7	Conclusions	159
8	Kinetics of the allotropic hcp-fcc phase transformation in cobalt	161
8.1	Introduction	161
8.2	Theoretical Background of Transformation Kinetics	162
8.2.1	The hcp \rightleftharpoons fcc Transformation Mechanism	163
8.2.2	Nucleation	166
8.2.3	Interface-controlled growth	169
8.2.4	Extended Fraction, Transformed Fraction and Impinge- ment	170
8.3	Experimental	170
8.3.1	Alloy Production	170

Contents

8.3.2	Differential Scanning Calorimetry	171
8.3.3	X-Ray Diffraction	171
8.3.4	Light Microscopy	172
8.4	Results and Evaluation	172
8.5	Analysis of the Transformation Kinetics	177
8.6	Discussion	181
8.6.1	Preceding transformation cycles	181
8.6.2	Kinetics	182
8.7	Conclusions	184
9	Summary	185
9.1	Summary in the English language	185
9.2	Zusammenfassung in der deutschen Sprache	188
	Bibliography	193

Chapter 1

Introduction

1.1 Interplay of the phase transformations and the microstructure of solids

This thesis is concerned with the interplay of the kinetics of solid-state phase transformations and the microstructure of materials: The kinetics of phase transformations depend on the parent microstructure and the resulting, product microstructure depends on the kinetics of the phase transformation. These interactions are investigated by the example of nucleation-and-growth, solid state transformations in elemental metals; in particular allotropic and recrystallisation transformations. In the analysis, kinetic models and mesoscopic simulations are employed.

Many industrially important materials undergo (desired) phase transformations in their manufacturing process, during which the microstructure which existed before the transformation (the parent microstructure) is deliberately replaced, partly or fully, by a new microstructure (the product microstructure). For engineering materials, this is often achieved by subjecting the material to a certain time-temperature program, i.e. a heat treatment, but also mechanical (e.g. hot or cold deformation) or chemical processes (e.g. metal-gas reactions) can be employed. Since the microstructure largely determines many important structural and functional properties of materials, phase transformations can be employed to tailor existing materials and to design new ones [1]. Well-known examples include the austenite \rightleftharpoons ferrite transformation in steels, precipitation transformations in aluminium-based light alloys and nickel-based superalloys, which all have an enormous influence on the mechanical properties, as well as the improvement of the magnetic properties of electrical steel by controlled deformation and subsequent recrystallisation¹.

¹In the context of this thesis, recrystallisation is classified as a phase transformation. Using a narrow definition of the term “phase”, it could be argued that the material before and after recrystallisation is in the same phase. However, without doubt there exists a recrystallisation front at which the physical properties of the material change abruptly. Hence in a broader definition of the term “phase”, the deformed and recrystallised do *not* belong to the same phase. Moreover, recrystallisation occurs via the processes of nucleation, growth and impingement

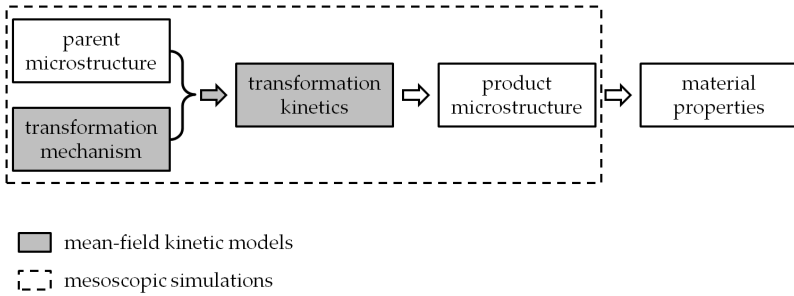


Figure 1.1: A schematic illustration of the relationship between microstructure and phase transformation kinetics. Mean-field kinetic models only address how the (experimentally accessible) transformation kinetics follows from the transformation mechanism, while mesoscopic simulations are able to take into account the influence of the parent microstructure and to predict the product microstructure. The way in which the product microstructure determines materials properties is beyond the scope of this thesis.

In order to employ phase transformations to influence the properties of materials, several steps are required. Firstly, a detailed knowledge about the thermodynamics and kinetics of the phase transformation is necessary to understand how a change in process parameters, e.g. the annealing temperature and time, influences the phase transformation, in particular the phase-transformation kinetics. Secondly, it must be established how the phase transformation controls the product microstructure and, thirdly, how the product microstructure affects the properties of the material. This thesis will be concerned with the first two of these steps. The relationship between parent microstructure, phase-transformation kinetics, product microstructure and material properties is shown schematically in figure 1.1.

1.1.1 Step 1: Modelling the phase-transformation mechanism

The driving force for phase transformations, i.e. its *thermodynamics* derives from the difference of the Gibbs energies of the parent and the product phase. In the case of allotropic transformations in elemental metals, the

and therefore can be described with the same modelling and simulation approaches as phase transformations.

1.1 Interplay of the phase transformations and the microstructure of solids

driving force and its temperature dependence are usually known or can be determined from experiments. The *kinetics* of a phase transformation involves the time dependence of the (volume) fraction transformed², $f(t)$. The kind of phase transformation which is the subject of this thesis proceeds by nucleation of the product phase in the matrix of parent phase and by subsequent growth of product-phase grains until they impinge onto each other. The laws governing each of these three concurrent processes constitute the “mechanism” of the phase transformation. This includes the rate at which new nuclei are formed and their spatial distribution, the shape of the growing grains, the connection between the driving force for the transformation and the velocity of the interphase boundaries, and the mode of impingement, i.e. whether a product grain is slowed down gradually when approaching another product grain, e.g. by overlap of diffusion fields, or whether a product grain continues to grow at unchanged rate until it makes contact with a neighbouring, growing product grain.

In general, nucleation, growth and impingement all depend on the parent microstructure existing before the phase transformation. In some cases, the parent microstructure can be assumed to be entirely homogeneous, so that the nucleation and growth rates are identical everywhere in a specimen. In other cases, more common in solids, however, the inhomogeneous nature of the parent microstructure strongly influences the transformation mechanism. If, for example, nucleation takes place on defects in the parent microstructure, such as grain boundaries, the nuclei are inhomogeneously distributed. This influences both the nucleation rate and the impingement. Similarly, if the driving force of the transformation is inhomogeneous in the parent microstructure, the growth rate varies from location to location. Therefore, the transformation mechanism and the parent microstructure *together* determine the phase transformation kinetics (see schematic in figure 1.1).

When the phase-transformation mechanism is formulated as a quantitative *kinetic model*, the transformed fraction as a function of time and temperature can be calculated, given a set of process parameters (e.g. the time-temperature program) and material parameters (e.g. the interface mobility) [2]. This is not a trivial procedure, since the constituting equations, e.g. the interface migration rate, are given for an individual grain while the transformed fraction, a scalar quantity, represents an average over all

²In the case of non-isothermal transformations, also the temperature is time-dependent, $T(t)$, which in turn influences the thermodynamics and kinetics of the transformation, i.e. the transformed fraction, $f[T(t)]$. Note that t and T are no independent variables (state variables) for the transformed fraction [1].

product grains of a specimen, which interact with each other by impingement. This problem can be overcome by employing a mean-field approach: the interaction of growing grains with the surrounding grains by impingement is replaced by the interaction of each grain with a mean field, i.e. the mean value of the transformed fraction in the whole specimen. Under some special conditions (including a spatially random distribution of nuclei and equi-axed, isotropic growth of grains; see section 1.2.1), this allows an *exact* analytical description of the transformation kinetics. The course of the transformed fraction over time thus obtained can then be compared directly with experimental results. If model prediction and measurement match, it can be stated with some confidence (but not with certainty; see the next section) that the mechanisms assumed in the construction of the kinetic model indeed operate during the phase transformation under consideration.

Mean-field models have severe limitations. They are only exactly valid if the parent microstructure is assumed to be a structureless continuum into which the product phase grows, thereby implying that the nucleation probability and the driving force (and therefore the nucleation and growth rates) are equal at each location in the parent microstructure. Even though extensions of these models are available which partially alleviate this limitation (see section 1.2.2), the treatment of the impingement problem is not exact in these cases. In circumstances where the mean-field approaches fail, there is no flexible and comprehensive approach available to treat impingement of growing grains and thus to derive kinetic models for phase transformations. However, in these cases mesoscopic simulations can be employed (see what follows).

1.1.2 Step 2: Predicting the product microstructure

Mean-field kinetic models only yield very limited information³ about the product microstructure, even though assumptions about the number and shape of product grains are made in their derivation. This information is essential if the properties of materials are to be optimised.

Moreover, if the identification of the operating mechanism of a phase transformation relies solely on the comparison of the kinetic model with experimentally determined kinetics, it is possible that wrong conclusions are drawn, in particular in cases of relatively low driving force (cf. chapter 6 of this thesis). Therefore, it is important to obtain agreement between the (product) microstructure predicted by a phase transformation mechanism

³The average grain size and higher moments of the grain-size distribution such as the variance are accessible [3,4].

1.1 Interplay of the phase transformations and the microstructure of solids

and the experimentally observed microstructure. If the mechanism of the transformation is not properly identified or if some approximations made in the construction of the kinetic model, e.g. for the impingement equation (see section 1.2.2), are not validated, it is possible that kinetic parameters inferred from model fits to experimentally determined transformation kinetics yield erroneous results. Therefore, it is important to compare both the predicted kinetics *and* the predicted microstructure with experimental results.

The restrictions of mean-field models can be lifted by employing mesoscopic simulations. Hereby, the impingement of grains is carried out explicitly in discretised time and space and the transformed fraction results simply from averaging over all discrete volume elements (called “voxels” in the case of three-dimensional simulations). The growth of grains is treated either by applying “global rules”, i.e. by prescribing a shape and a growth rate for each grain, or by applying “local rules”, i.e. by treating the migration of interfaces voxel-per-voxel (see section 1.3). Such simulations offer full information about the microstructure, e.g. the grain-size distribution, at all stages of the phase transformation, which is essential for the prediction of material properties. Additionally, they allow to take into account the influence of spatially non-random distributions of nuclei, of an inhomogeneous driving force etc., and thereby allow to describe a wide range of different transformation mechanisms.

1.1.3 Scope of the thesis

In this thesis, three different aspects of the interaction of the microstructure of a material undergoing a phase transformation and the corresponding transformation kinetics are dealt with.

- I. For a given kinetic model of a phase transformation, the influence of varied material parameters and process parameters on the resulting product microstructure is investigated (chapter 2).
- II. For a given kinetic model of a phase transformation, the influence of varied parent microstructure on the parent \rightarrow product kinetics is investigated (chapters 3, 4 and 5).
- III. By comparing the simulated kinetics and product microstructure with experimental results, the suitability of specific models to describe the kinetics of a phase transformation is investigated (chapters 6, 7 and 8).

All work presented in this thesis is restricted to (heterogeneous) solid-state phase transformations which transform the entirety of the parent microstructure into a new microstructure via the nucleation and growth of product-phase grains and subsequent impingement of the grains onto each other. This means that, e.g. precipitation reactions, where impingement of diffusion fields plays an important role, or spinodal de-mixing transformations, are beyond the scope of this thesis. All transformations are assumed to proceed with “interface-controlled growth”, i.e. for the migration of interfaces during the transformation, the rate-controlling process is the jump of atoms through the interface from the parent phase to the product phase. Phase transformations which proceed according to these criteria include e.g. the allotrop transformations in elemental materials and recrystallisation.

1.2 Kinetic models

1.2.1 The classical JMAK and JMAK-like models; the modular approach

The classical JMAK model (and JMAK-like models) for phase transformation kinetics go back to works in the 1930s by Kolmogorov, Avrami, Johnson and Mehl [5–7]. They are mean-field models which all assume homogeneous (spatially random) nucleation in the bulk of the parent phase [1, 8]. This allows to relate the real transformed (volume) fraction of a specimen, f , with the hypothetical, so-called extended transformed fraction, x_e , which is defined as the volume fraction of all growing grains if they could each nucleate and grow in an infinitely large parent phase in the absence of other (growing) nuclei. For the case of randomly dispersed nuclei which grow isotropically, the real transformed (volume) fraction can be related to the extended transformed fraction according to

$$df = (1 - f)dx_e. \quad (1.1)$$

After integration, this becomes

$$f = 1 - \exp(-x_e). \quad (1.2)$$

In other words, the increase in transformed fraction, df , can be calculated by considering the “interaction” of the increase of the extended transformed fraction, dx_e , (which can be calculated by treating each growing grain individually) with the “mean field” of all other grains, i.e. the transformed fraction, f .

The classical JMAK equation pertains to isothermal transformations and is valid only if a high driving force prevails and only for a limited set of nucleation and growth mechanisms (in addition to the conditions holding for Eq. (1.1)) [1]. By substitution of the specific expression of x_e in Eq. (1.2), the JMAK model leads to an equation of the type

$$f(t) = 1 - \exp(-kt^n), \quad (1.3)$$

where $k = k_0 \exp(-Q_{\text{eff}}/RT)$ is the rate constant which depends on the transformation temperature T via the effective, overall activation energy Q_{eff} and n is the Avrami, or growth exponent. Therefore, if a phase transformation kinetics obeys a JMAK model, plotting the transformed fraction as $\ln(-\ln(1-f))$ versus $\ln(t)$ in a so-called “double-logarithmic plot”, yields a straight line with the slope n .

In the JMAK model, the pre-exponential factor k_0 , the effective activation energy Q_{eff} and the growth exponent n are constant during the entire phase transformation. In JMAK-like models, Eq. (1.3) still holds, but k_0 , Q_{eff} and n are time or temperature dependent.

Without restrictions on the time/temperature dependencies of the nucleation and growth rates and for arbitrary annealing treatments, the transformed fraction can be calculated in the framework of the modular kinetic model (MKM) approach [8], as follows.

The extended transformed fraction as function of time, t , and temperature T , where T can depend on t in case of non-isothermal transformations, can be calculated straightforwardly by integrating the extended volume of grains nucleated at a certain time τ , denoted by $Y_e(\tau, t)$, times the nucleation rate per unit volume prevailing in the specimen at that time, $\dot{N}_V(T(\tau))$, with respect to the nucleation time τ

$$x_e(t) = \int_0^t \dot{N}_V(T(\tau)) Y_e(\tau, t) d\tau. \quad (1.4)$$

Adopting the case of isotropically growing grains, the extended radius of one grain, $R_e(\tau, t)$, can be obtained by integrating its growth rate/interface velocity from the time of nucleation, τ , until the current time, t . The extended volume of one grain can then be calculated by taking the radius to the d -th power (for d -dimensional growth) and by multiplying with an appropriate shape factor g ($= 4/3\pi$ for growing spheres):

$$Y_e^{\text{ex}}(\tau, t) = g [R^{\text{ex}}(\tau, t)]^d = g \left[\int_{\tau}^t v(T(t')) dt' \right]^d. \quad (1.5)$$

Note that this last equation only holds for interface-controlled (linear) growth, which is the only growth mode considered in this thesis. Adopting additionally the case of random nucleation, the transformed fraction can be calculated from Eqs. (1.2), (1.4) and (1.5), provided the nucleation and growth rate of product-phase grains are known.

1.2.2 Beyond JMAK models; the case of non-random nucleation

Often, it is not possible to describe experimentally determined phase transformation kinetics with models of the type presented above, or a fit of the model to the experimental data yields physically unrealistic values. Discrepancies between experimental results and JMAK-like models are usually attributed to a breakdown of one of the model assumptions, e.g. isokinetic behaviour, hard impingement or a random spatial distribution of nucleation sites.

One part of this thesis is focused on the influence of the parent microstructure on the parent→product kinetics; in particular on the influence of spatially non-random nucleation. For the modelling of this situation, it was suggested [8–10] to modify Eq. (1.1) to take into account the “strength” of impingement. Two different modifications were proposed, namely

$$df = (1 - f)^{\zeta} dx_e \quad (1.6)$$

and

$$df = (1 - f^{\varepsilon}) dx_e. \quad (1.7)$$

In these equations, ζ and ε are impingement parameters which do not have an *a priori* physical meaning. For both parameters, as compared to “random nucleation” (and isotropic growth), a value larger than one leads to stronger impingement and a value smaller than one leads to weaker impingement. These impingement equations can be incorporated in the MKM approach.

A more physical model for the description of a specific case of non-random nucleation, namely the nucleation on parent-phase grain boundaries, was developed by Cahn [11]. In this approach, parent-phase grain boundaries are approximated as planes which are randomly distributed in space. Nucleation takes place randomly on these planes and growth of product grains occurs isotropically into both adjacent parent “grains”. The impingement problem is rendered tractable by approximating it as a combination of two separate impingement processes: First, the (lateral) impingement of grains originating from *one* grain boundary is addressed. Since nucleation occurs randomly on grain boundaries, this can be done using Eq. (1.1). After

having accounted for the impingement of grains originated from *one* grain boundary, the effect of impingement of product phase grains growing from *all* grain boundaries is treated next. Because the grain boundaries are assumed to be randomly distributed in space, the volume of all grains nucleated on one grain boundary can be treated as the extended volume in this second impingement problem. Again, an equation analogous to Eq. (1.1) is applied and the total transformed volume fraction is obtained.

In contrast to Eqs. (1.6) and (1.7), which are of empirical nature, this last impingement model has a physical background. Nevertheless, the assumption of randomly distributed *planes* as parent grain-boundaries in this model may not be a valid approximation for nucleation on a realistic grain-boundary *network*. This question is addressed in chapter 4.

1.3 Mesoscopic simulation methods

Phase transformations can be simulated with a variety of techniques. At the atomistic level, simulation methods such as molecular statics, molecular dynamics, kinetic Monte Carlo or the crystal phase-field method are used to investigate the migration of short interface segments over a short period of time. Atomistic simulations are briefly touched upon in chapter 5, where the results of previously published kinetic Monte Carlo simulations of the fcc-bcc phase transformation in pure iron are reviewed.

Simulation techniques which operate at a length scale above that of individual atoms, but below that of entire workpieces are called mesoscopic simulations. They are designed to capture the microstructural development of materials during various processes, e.g. phase transformations or grain growth, and are therefore applicable to the subject of this thesis. Various mesoscopic simulation algorithms are available, including geometric algorithms [12–14], (Potts-) Monte Carlo algorithms [15], Cellular Automata algorithms [16,17], and phase-field algorithms [18].

Geometric algorithms are most closely connected with kinetic models. They need the nucleation rate, the growth rate and the shape of the growing grains (usually assumed to be spherical) as input values, thereby adopting “global rules” for the simulation. Nucleation and growth are carried out in discretised space and time. For each time step, the number of nuclei which should be formed is calculated from the nucleation rate and the radius of the grains (in the absence impingement) is calculated from the growth rate. Impingement is treated by not allowing grains to grow further once they touch

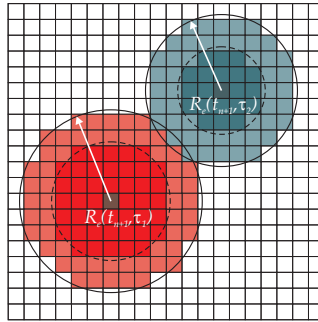


Figure 1.2: Schematic illustration of a growth step in a geometric simulation. Two different grains are shown which grow as circles (in this two-dimensional schematic). Their radius in the previous time step is shown as dashed line and their radius in the current time step is shown as full line. Note that some pixels could have been transformed by both grains at the emerging grain boundary; they are assigned to the grain which reaches them first.

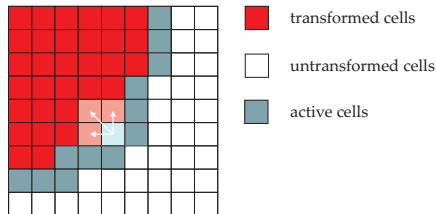


Figure 1.3: Schematic illustration of a Cellular Automaton growth step. At the interface between transformed and untransformed material, it is checked for each cell at the interface between transformed and untransformed regions (the “active” cells) whether the transformation front can advance into the neighbouring cells. One of the active cells and the neighbouring transformed cells, which could cause the active cell to become transformed (arrows), are highlighted.

each other (see figure 1.2). Geometric simulations are computationally very efficient, since, dependent on the instantaneous growth rate, a grain can grow across many pixels in one time step. If the algorithm is adapted for parallel execution on a multi-processor computer, it is possible to simulate the nucleation and growth of about 50 000 grains in a simulation cube consisting of 600^3 voxels in approximately 10 minutes on a modern workstation with 6 CPUs. The symmetry of the lattice used for the spatial discretisation cannot introduce propagating errors into the simulations, since the geometry of the growing grains is given by the global transformation rules.

However, geometric simulations are also the least flexible of the algorithms mentioned above. Since the shape of the growing grains is a part of the simulation algorithm, they cannot deal e.g. with local variations in the growth rate of grains. Geometric simulations are best suited to determine the microstructure resulting from a phase transformation for which a kinetic model has been established (see chapter 2). Additionally, they can be used to study the influence of a spatially non-random distribution of nuclei on the phase transformation kinetics and microstructural development (see chapters 3 and 4).

Cellular Automata algorithms and (Potts-) Monte Carlo algorithms are related simulation methods which operate with local rules describing what is happening at a lattice point of the simulation cube (transformation or not) only on the basis of its current state and the state of the neighbouring lattice points (see figure 1.3). While in Cellular Automata, each lattice point ("cell") is checked once at each time step, the lattice points are visited in random order in Monte Carlo simulations. In both methods, the simulation can be sped up by only considering untransformed, "active" cells at the interface between transformed and untransformed regions. The switching rules determining whether an active cell should be transformed or not in a certain time step can be deterministic or probabilistic ones in both simulation methods. In this thesis, Cellular Automata simulations with deterministic switching rules will be employed. They are more computationally intensive than geometric simulations, since (on average) it takes several time steps for the transformation front to advance by one cell (i.e. generally several time steps elapse from the time at which a cell becomes active until the time at which an active cell is transformed). This is the case because the time step must be chosen small enough to minimise the influence of the symmetry of

the lattice used for the spatial discretisation⁴. One simulation consisting of about 1 000 grains growing in a simulation cube of 450^3 voxel lasts approximately 90 minutes, running on a single CPU.

Cellular Automata simulations offer the possibility to include a growth rate which varies locally, e.g. by varying the driving force of the phase transformation from cell to cell. Therefore, anisotropic growth can be investigated with such simulations. In this thesis, they are used to study the kinetics and microstructural development of the recrystallisation of pure copper (see chapter 7).

Phase-field simulations formulate the growth of grains in a framework of partial differential equations as the temporal evolution of the location-dependent transformed fraction (the “phase field”). They are computationally intensive, but allow to flexibly treat phase transformations which involve the interaction of several externally applied fields (e.g. a temperature and a stress field) and the phase field. Additionally, they are well suited for the simulation of diffusion-controlled phase transformations, such as the solidification of alloys or precipitation transformations, where the phase field and the concentration field (i.e. the location-dependent concentration) interact during the transformation, but they do not offer advantages in the simulation of the kind of interface-controlled transformations (lacking long-range diffusion) considered in this thesis.

1.4 Investigated phase transformations

Three different phase transformations are investigated in this thesis and compared with the results of kinetic models and mesoscopic simulations:

Fcc \rightleftharpoons bcc transformation in pure iron. In a certain range of cooling rates, the austenite (fcc) \rightleftharpoons ferrite (bcc) transformation in pure iron occurs as a massive transformation. This means that it is an interface-controlled transformation, controlled by *uncorrelated* atomic jumps across the interface, in which no specific crystallographic orientation relationship is preferred between parent and product phases. The results of atomistic simulations on the migrating fcc/bcc interface are briefly reviewed in this thesis (see chapter 5).

⁴The influence of the discretising lattice is strongest if only the first neighbour shell is used in the decision whether a cell transforms or not. If second- and third-nearest neighbours are included, the grains grow almost unaffected by the lattice symmetry

Recrystallisation of pure copper. This transformation occurs upon annealing of cold-worked copper by migration of high-angle grain boundaries. Both the experimentally determined kinetics and the product microstructure are analysed. The influence of the inhomogeneous driving force (i.e. the stored energy due to cold working) and the influence of the orientation relationship between deformed matrix and recrystallised grains on the nucleation and the growth mechanisms are investigated using Cellular Automata simulations (see chapters 6 and 7).

Fcc \rightleftharpoons hcp transformation in pure cobalt. This martensitic (also interface-controlled) transformation, in this case involving *correlated* atomic jumps across the interface, relating two close-packed crystal structures occurs via the ordered glide of Shockley partial dislocations. Since the partial dislocations cannot cross high-angle grain boundaries, the parent microstructure plays an important role in the kinetics of this phase transformation. The influence of repeated cycling on the phase-transformation kinetics is investigated and a kinetic model is developed (see chapter 8).

1.5 Organisation of the thesis

The thesis consists of several parts. In the first part, (*chapter 2*), geometric simulations are employed to investigate how changing parameters of the kinetic model and of the temperature program influence the microstructure, in particular the grain-size distribution. The algorithm used in the geometric simulations is described and then applied to phase transformations from a supersaturated matrix upon isochronal heating and cooling.

The next part (*chapters 3 and 4*) deals with phase transformations in which nucleation occurs spatially non-randomly on grain-boundaries in the parent microstructure. The influence of the parent microstructure, namely the mean parent grain size and the parent grain-size distribution, as well as the influence of the parent \rightarrow product kinetics, is investigated using geometric simulations. A new modification to kinetic models for grain-boundary nucleated phase transformations is proposed which can be reliably used to infer kinetic parameters from experimentally determined phase transformation kinetics.

In *chapter 5*, the results of chapters 2–4 are summarised and discussed in the context of previously published atomistic simulation results concerning the mobility of the fcc/bcc-interface during the massive austenite-to-ferrite transformation in pure iron.

Chapter 1 Introduction

In the next part, (*chapter 6 and 7*), the recrystallisation of pure copper is investigated by experiments and simulations. The kinetics of recrystallisation is recorded using differential scanning calorimetry and the microstructural development during recrystallisation is characterised by electron backscatter diffraction. The experimental findings are contrasted with the results of geometric simulations (*chapter 6*). The influence of an inhomogeneous deformed state (before recrystallisation) and thus local variations in growth rate on recrystallisation kinetics and microstructural development are examined using Cellular Automata simulations and compared with experimental results (*chapter 7*).

In the last part (*chapter 8*), the allotropic hcp/fcc phase transformation in pure cobalt is investigated by X-ray diffraction and differential scanning calorimetry. The influence of the parent microstructure on the transformation kinetics is discussed and a suitable kinetic model to describe the kinetics is developed.

Chapter 2

Predicting microstructures from phase transformation kinetics: The case of isochronal heating and cooling from a supersaturated matrix

2.1 Introduction

Phase transformations play a key role in the manufacturing process of many materials. They have a great influence on the microstructure and hence on the properties of the material. A detailed knowledge about the mechanisms of phase transformations is therefore necessary to design new materials and to optimize their properties (for a recent example, see Ref. [19]). This knowledge can be obtained by observing and analysing the kinetics of the concerned phase transformation. Often it is attempted to describe the kinetics of (nucleation-and-growth) solid-state transformations by the classical model by Johnson, Mehl, Avrami and Kolmogorov (JMAK) that describes the nucleation and subsequent growth of a product phase in the matrix of the parent phase until the whole parent phase is transformed [5–7]. The JMAK model holds only under severe constraints; extension to more complex nucleation, growth and impingement modes as well as arbitrary temperature-time programs is provided by the modular kinetic model described in Ref. [8].

The kinetic parameters of the transformation model are usually determined by fitting the degree of transformation as calculated by the model to the experimentally determined time-temperature dependence of the degree of transformation (for a recent example, see Ref. [20]). Once the kinetic parameters are known, the kinetic model can be used to derive a much more detailed picture of the evolving microstructure than that provided by the transformed fraction, which is a single number. This can be done in various ways. Already the first authors who treated phase transformation kinetics rigorously were concerned with determining average grain sizes and grain-size distributions (GSDs) from kinetic models applied to isothermal transformations [7, 21]. Meijering [3] and Gilbert [4] calculated the first and second moments of several geometric properties (e.g. grain volume,

grain surface) of microstructures, again resulting from isothermal transformations, with nuclei that are uniformly distributed in space and that are either already present at the beginning of the transformation (a situation termed either “pre-existing nuclei”, “site saturation” or “cell model”) or that form with constant nucleation rate per unit volume of untransformed material (“continuous nucleation” or “Johnson-Mehl-model”). Generally, it is possible to simulate the microstructure evolving during a phase transformation by taking into account the geometrical assumptions made in the kinetic model and applying one of several established simulation schemes as described in section 2.2.1.

The purpose of this chapter is to explore the microstructures, as reflected in grain-size distributions, resulting from *nonisothermally* conducted phase transformations. It will be shown that large differences occur between the microstructures resulting from transformations upon (isochronal) heating and from transformations upon (isochronal) cooling. After a short overview of methods for microstructure simulation and analysis (section 2.2.1), the method used in this work is presented (section 2.2.2). Subsequently, it is applied to the cases of transformations during isochronal heating and cooling (sections 2.3.1 and 2.3.2). Finally, a general discussion of the observed results is given and different methods for analysing the obtained microstructures are compared (section 2.3.3).

2.2 Modelling of Grain-Size Distributions

2.2.1 Methods for Microstructure Simulation

The average grain volume, $\langle V \rangle$, of a microstructure is given by the inverse of the average number of grains per unit volume (the grain density, ρ_{grains})

$$\langle V \rangle = \rho_{\text{grains}}^{-1}. \quad (2.1)$$

In the case of site saturation, the grain density is equal to the number of nuclei per unit volume present at the beginning of the transformation. For continuous nucleation and generally for all models in which nucleation takes place during the transformation, however, nuclei can only form in regions that are still untransformed, so that the nucleation rate, $\dot{N}(t)$, i.e. the number of nuclei that form per unit time and per unit volume, must be multiplied by the untransformed fraction $(1 - f(t))$ and integrated over the whole transformation time to yield the final density of nuclei and thus, product grains:

$$\rho_{\text{grains}} = \int_0^{\infty} \dot{N}(t)(1 - f(t))dt. \quad (2.2)$$

2.2 Modelling of Grain-Size Distributions

In the case of constant nucleation rate, \dot{N} , and constant (linear and isotropic) growth rate, v , as could occur during isothermal transformations, equation (2.2) can be evaluated to [3,7]

$$\rho_{\text{grains}} = 0.8960 (\dot{N}/v)^{3/4}. \quad (2.3)$$

For simple nucleation and growth models, grain-size distributions can be calculated analytically. In the case of site saturation, for example, the resulting microstructure is called Voronoi-tessellation and its GSD (the probability p of finding a grain of normalised volume between $y = V/\langle V \rangle$ and $y + dy$) is described by the Kiang conjecture [22] (see also Figure 2.3 in section 2.2.3)

$$p(y) = \frac{c^c}{\Gamma(c)} (y)^{c-1} \exp(-cy), \quad (2.4)$$

where Γ is the Gamma-function and c is a constant. This conjecture was analytically proven to be correct for the one-dimensional case ($c = 2$), but for the three-dimensional case the value of $c = 5.586$ could only be determined by Monte-Carlo simulations [23, 24]. This specific GSD does not depend on the time or temperature dependency of the growth rate and is therefore identical for transformations upon isochronal heating, isochronal cooling and upon isothermal annealing.

To find analytical descriptions for GSDs resulting from more complicated nucleation and growth mechanisms is very difficult [24, 25] and generally impossible. However, a numerical approach is usually possible by casting a phase-transformation model in the form of an iterative algorithm that simulates nucleation, growth and impingement of grains on a discretised lattice following certain rules. Such calculations were done in the past using Monte Carlo algorithms [15,26], cellular automata [16,17] as well as geometric models [12–14, 27]. While the former two classes of models operate with local rules describing what is happening at a lattice point (transformation or not) only on the basis of its current state and the state of the neighbouring lattice points, the latter class of models uses “global” rules to decide if a lattice point should transform or not. These global rules are given by the nucleation and growth rate prevailing in the sample at a given time (and temperature). These nucleation and growth rates can be taken from an underlying kinetic model.

There are two main advantages of global growth models over local growth models: First, their computational efficiency is better. In local growth models, the duration of one time step must be less than the time that the interface between transformed and untransformed material needs to move over the

width of one voxel in order to avoid discretisation errors. In global growth models, the time step can be much larger than this without introducing a propagating error into the simulation, since the position of the interface is calculated independent of the used lattice. Second, the symmetry of the lattice used for the spatial discretisation cannot introduce propagating errors into simulations based on a global growth model, since the geometry of the growing grains is given by global rules.

Geometric models have been used in the past to simulate the microstructure resulting from various nucleation and growth modes, in particular for isothermal transformation (i.e. for constant nucleation and growth rates), see Ref. [12] for an early example, and for isochronal heating transformations, see Ref. [28] for a recent example.

It should be noted that for all transformations which can be correctly described by the kind of kinetic model used here, the presented geometrical method is able to predict the final microstructure of the material. The usage of more sophisticated (and more laborious) simulation methods, e.g. the phase field method, does not provide significant additional insight and is therefore not necessary in the present context.

2.2.2 Method employed

In the present work, a geometric algorithm is employed to simulate three-dimensional microstructures resulting from transformations of a supersaturated parent phase. The global transformation rules are given by a modular kinetic model [8] for the underlying phase transformation kinetics.

Each simulation run begins by calculating the kinetics, i.e. the dependency of the transformed fraction on time, $f(t)$, or temperature, $f(T)$. Note that temperature and time are in general no state variables for the transformation: $f = F(T(t))$ [29]. All simulations in this chapter were performed either isochronally (heating/cooling rate $\Phi = \text{const.}$) or isothermally ($\Phi = 0$), so that the temperature as a function of time is given by

$$T(t) = T_0 + \Phi t, \quad (2.5)$$

with the starting temperature (or the isothermal temperature) T_0 . Therefore, the degree of transformation can always be expressed as $f(t)$ because for an isochronally conducted annealing, a change in time prescribes a change in temperature according to equation (2.5). Two modes of nucleation are considered in this chapter: site saturation and continuous nucleation. In the case of site saturation, all nuclei exist from the beginning of the transformation (i.e. pre-existing nuclei) and no nucleation takes place while growth

occurs. In the case of continuous nucleation, nuclei form during the phase transformation with a certain rate per unit volume of untransformed material. This continuous nucleation rate is constant for isothermal transformations, but not for nonisothermal transformations. An Arrhenius-type temperature dependency is assumed in this chapter for both the nucleation rate and the interface velocity of growing grains $v(t)$. This (usual) assumption implies that the chemical driving force is large and does not influence the kinetics [2, 8]. This holds for example for the interface controlled austenite-ferrite transformation in ultralow-carbon steel [30] or the crystallisation of amorphous alloys [31, 32]. Thus:

$$\dot{N}(t) = N_0 \exp\left(-\frac{Q_N}{k_B T(t)}\right) \quad \text{and} \quad v(t) = v_0 \exp\left(-\frac{Q_G}{k_B T(t)}\right) \quad (2.6)$$

with k_B as the Boltzmann constant, N_0 and v_0 as pre-exponential factors and Q_G and Q_N as the activation energies for nucleation and growth (interface movement), respectively.

The radius of an isotropically growing grain, if unhindered by impingement, the so-called "extended radius" of a specific grain, $R_e(\tau, t)$, is given by integrating the interface velocity with respect to time from the nucleation time τ of the grain considered until the current time t :

$$R_e(\tau, t) = \int_{\tau}^t v(t') dt' \quad (2.7)$$

For interface-controlled growth, the interface velocity v is only dependent on the temperature [cf. equation (2.6)]. The "extended volume" of a grain, $Y_e(\tau, t)$, is accordingly defined as the volume of the sphere with radius R_e . The extended transformed fraction, $X_e(t)$, can now be obtained by multiplying the extended volume for grains nucleated at certain times τ with the nucleation rate at that time and integrating with respect to the nucleation time from zero to the current time (and dividing by the sample volume, V_{tot} , which is taken as constant).

$$x_e(t) = \frac{1}{V_{\text{tot}}} \int_0^t \dot{N}(\tau) Y_e(\tau, t) d\tau. \quad (2.8)$$

Finally, assuming impingement according to randomly dispersed nuclei, the transformed fraction is given by

$$f(t) = 1 - \exp(-x_e(t)), \quad (2.9)$$

which, in case of isothermal transformations, leads to the well-known JMAK-equation. For a "JMAK"-equation in the case of nonisothermal transformations, see Ref. [8, 29].

In the computer program, $f(t)$ is calculated by numerical integration of the integrals in equations (2.7) and (2.8) employing an efficient algorithm specifically developed for this problem [8]. The quantities necessary for the microstructure simulation, i.e. the nucleation rate per unit volume of untransformed material, $\dot{N}(t)$, and the extended grain radius, $R_e(\tau, t)$, are calculated and stored.

It must be stressed that the presented method is by no means restricted to the nucleation and growth mechanisms considered here; other time, temperature or grain-radius dependencies of the interface velocity and other nucleation laws could be used without modifications to the algorithm. The chosen nucleation and growth mechanisms serve merely to illustrate the differences of typical GSDs that can be expected to result from phase transformations upon heating and cooling.

The microstructural evolution is simulated next. The transforming specimen is modelled as a cube with periodic boundary conditions applied in all three dimensions. The specimen is divided into cubic voxels that all carry the number "0" (the untransformed state) at the beginning of the transformation. For each discrete time step Δt , it is calculated how many nuclei emerge according to the nucleation rate given by equation (2.6) and a corresponding number of nucleation sites are chosen randomly from the whole specimen. If the voxel at a designated nucleation site is still in the untransformed state, nucleation is carried out there by assigning a unique grain number to the voxel (thereby changing it to the transformed state) and recording its position and nucleation time. Subsequently, growth of all product grains takes place as follows. For each grain of known nucleation time τ_i (which is always smaller than the current time t), the extended radius $R_e(\tau_i, t)$ is looked up and all voxels lying within a sphere of this radius around the nucleus voxel of the grain are determined. All of those voxels that are still untransformed and that lie within the R_e -sphere of only the considered growing grain are assigned the grain number. For all of those voxels that are still untransformed and that lie within the R_e -spheres of several growing grains, it is checked to which of the growing grains such a voxel should be assigned by calculating two distances for each of the growing grains. First, the distance between the centre of the concerned voxel and the centre of the nucleus voxel, $R_{\text{voxel-nucleus}}$, is determined. Then, the difference ΔR between $R_e(\tau_i, t)$ and $R_{\text{voxel-nucleus}}$ is calculated. The voxel is then assigned to the grain with the highest value of ΔR . Omitting this comparison of ΔR -values and assigning the voxel randomly to one of the growing grains in whose R_e -spheres it lies, leads to a "rough" interface between grains and an artificially high number of one- or two-voxel-wide grains, but

otherwise does not affect the accuracy of the simulated grain-size distributions.

The thus simulated three-dimensional microstructure is analysed to determine the grain-size distribution. It is also possible to extract further information from the simulated microstructure, like the number of grain edges per grain or the total grain-boundary area. However, the discussion in this chapter is restricted to grain-size distributions as a sensitive, albeit not unique means to characterise the microstructure. Three measures for grain size are employed in this work: D_V , D_A and D_L , as follows.

The value of the volume-weighted size of a grain, D_V , is defined by the the diameter of the sphere with the same volume V as the grain:

$$D_V = \left(\frac{6V}{\pi} \right)^{1/3}. \quad (2.10)$$

The volume-weighted GSD is calculated by summing the number of voxels carrying the same grain number and applying equation (2.10) and is represented as function of the normalised grain size $D_V/D_{\langle V \rangle}$. The volume-weighted size of a grain of average volume, $D_{\langle V \rangle}$, can be calculated by substituting the average grain volume $\langle V \rangle$ given by equation (2.1) into equation (2.10).

The area-weighted grain size, D_A , is determined by the diameter of the circle with the same area A as the surface occupied by the grain in a planar cross section through the specimen

$$D_A = \left(\frac{4A}{\pi} \right)^{1/2}. \quad (2.11)$$

The area-weighted GSD is calculated by making several cross sections in several directions perpendicular to each other through the specimen and determining the surface occupied by the grains in all these cross sections. It is expressed as function of the normalised grain size $D_A/D_{\langle A \rangle}$ with $D_{\langle A \rangle}$ corresponding to the average grain area $\langle A \rangle$ in all cross sections.

Finally, the line-weighted grain size D_L is determined by a line-intercept method according to [33], where the width spanned by grains along straight lines through the specimen ("intercept lengths") is measured. The GSD is obtained by drawing many lines in directions perpendicular to each other through the sample and measuring the resulting intercept lengths. It is represented as function of the normalised grain size $D_L/D_{\langle L \rangle}$ with $D_{\langle L \rangle}$ corresponding to the average intercept length.

Table 2.1: Parameters determining the numerical precision which were used in all simulations.

voxels per simulation cube edge	600
time steps (integration of equations (2.7) and (2.8))	10 000
time steps (microstructural evolution)	100
desired number of grains (N_{grains})	50 000

2.2.3 Simulation Parameters and Validation of the Algorithm

The input parameters governing the numerical precision of the simulation that are used in this work have been gathered in Table 2.1. In order that the same statistical precision and the same precision of the space and time discretisation is obtained for all combinations of kinetic parameters, the simulations should pertain to the same number of product grains, irrespective of the average grain size (that depends on the kinetic parameters and applied transformation conditions as heating or cooling rate). The value of the grain density (for completed transformation), ρ_{grains} , is given by equation (2.2) and is known in advance of the microstructure simulation. For a fixed desired number of grains, N_{grains} , in the simulation, the necessary edge length of the simulation cube L_{specimen} can therefore be calculated by

$$L_{\text{specimen}} = \left(\frac{N_{\text{grains}}}{\rho_{\text{grains}}} \right)^{1/3}. \quad (2.12)$$

Thus, N_{grains} can be used as an input parameter of the simulation instead of L_{specimen} , as desired.

Several parameters describing the kinetics of the transformation were held constant in all presented calculations; they are given in Table 2.2. The parameters were chosen to be physically reasonable for typical interface-controlled phase transformations (see [8]), but for the current work their values can be conceived as arbitrary because this work does not aim to reproduce one specific phase transformation; moreover (almost) all results are presented as normalised quantities. Figure 2.1 shows examples of the microstructure resulting from simulations. In Figure 2.1 a) and b), results of isothermal annealing (pre-existing nuclei and continuous nucleation, respectively) are shown while the microstructures in Figure 2.1 c) and d) result for isochronal heating and continuous nucleation (ratio of activation energies for nucleation and growth $Q_G/Q_N = 0.01$ and 100, respectively).

Table 2.2: Parameters determining the transformation kinetics which were used in all simulations. For the relevance of the numerical values, see text.

growth mode	interface-controlled and isotropic
growth geometry	spherical
N_0	$10^{20} \text{ m}^{-3} \text{ s}^{-1}$
v_0	10^{10} m s^{-1}
T_0 (heating)	0 K
T_0 (cooling and isothermal)	700 K
Φ	(10, 0, -10) K s^{-1}

The algorithm can be validated by comparing the transformed fraction calculated according to equation (2.9) with the transformed fraction determined in the simulation as the fraction of transformed voxels as a function of time. Examples of thus obtained results are presented in Figure 2.2. The agreement is excellent.

The grain-size distribution obtained from a simulation with pre-existing nuclei can be compared with that predicted by the Kiang conjecture (2.4): see Figure 2.3. Good agreement occurs. It has also been verified that the current model, applied to *isothermal* transformations gives results compatible with [3, 4, 12, 13, 27]. In particular, in agreement with [27], it was found that the GSD resulting from isothermal transformations, if represented as function of normalised grain size [cf. equation (2.10)], is independent of the used input parameters such as transformation temperature, activation energies and pre-exponential factors. In the following, the focus is on *nonisothermal* transformations.

2.3 Results and Discussion

2.3.1 Isochronal Heating

The only input parameter that has an influence on the normalised GSD is the ratio of the activation energies of nucleation and growth, in agreement with recent results [28]. Parameters such as heating rate, pre-exponential factors or the absolute values of Q_G and Q_N (for a fixed value of Q_G/Q_N) influence the average grain size but not the GSDs as expressed as function of *normalised* grain size. The change of the (volume-weighted) GSDs upon varying Q_G/Q_N is shown in Figure 2.4.

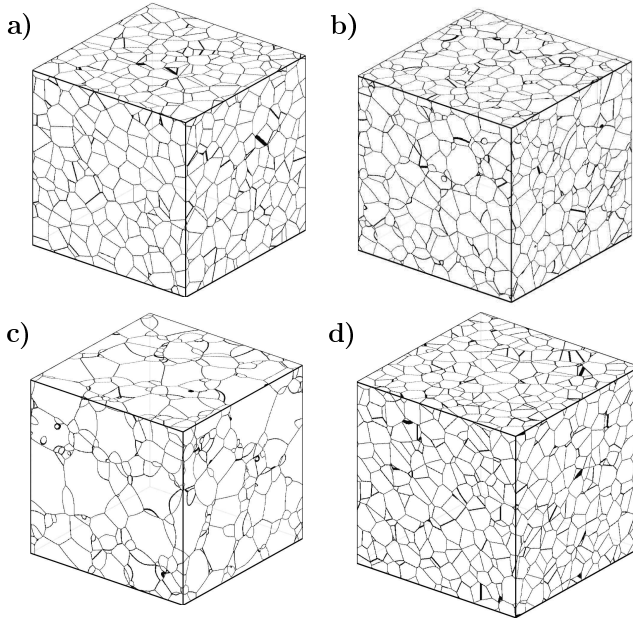


Figure 2.1: Example microstructures generated by the simulation algorithm (cf. the grain-size distributions in Figure 2.4): a) generated using pre-existing nuclei; b) generated using a constant nucleation rate (both isothermal annealing); c) generated during isochronal heating with continuous nucleation and a ratio of activation energies $Q_G/Q_N = 0.01$ (see section 2.3.1); d) as before but with $Q_G/Q_N = 100$. Shown, for all cases, is only a small part of a typical simulation cube.

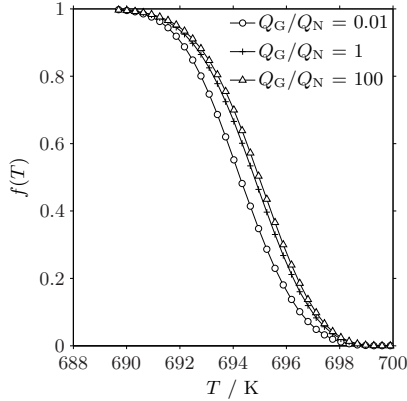


Figure 2.2: Transformed fraction as function of temperature for transformations upon cooling (at -10 K s^{-1}) with the continuous nucleation mode for various ratios of the activation energies for growth and nucleation, Q_G and Q_N . The symbols are the results of microstructure simulations (only every third symbol has been plotted to improve legibility), while the solid lines have been obtained by numerically integrating equation (2.9).

For low ratios Q_G/Q_N , the simulated microstructure consists of many small grains (that nucleated late) and only few large grains (that nucleated early). If the activation energies for nucleation and growth are equal, i.e. $Q_G/Q_N = 1$, a broad distribution with approximately equal numbers of large and small grains results. When Q_G/Q_N is increased further, the GSD becomes narrow and exhibits a sharp maximum at large grain sizes (i.e. many grains nucleated early). These results can be understood as follows.

Upon heating from 0 K, the rates for nucleation and growth are initially both zero. With rising temperature, the process with the lower activation energy first achieves rates significantly larger than zero. If this is the nucleation process (i.e. $Q_G/Q_N > 1$), nuclei are formed, but they cannot grow because the growth rate is still negligibly small. As the temperature continues to rise, growth eventually becomes significant. All nuclei formed so far then begin to grow simultaneously while nucleation continues. This leads to a grain-size distribution skewed to small grain sizes, i.e. a GSD with many large grains and few small grains. This distribution is very similar to the

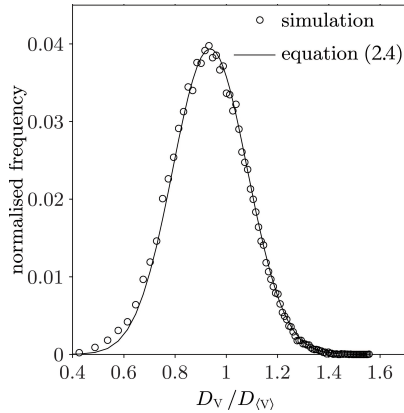


Figure 2.3: Grain-volume distribution of a microstructure resulting from an isothermal transformation with pre-existing nuclei (site saturation). Symbols represent the results of one simulation run and the solid line has been computed according to the Kiang conjecture (2.4)

narrow one observed for transformations with pre-existing nuclei⁵ (shown as dashed line in Figure 2.4). If, however, growth is the process with the lower activation energy (i.e. $Q_G/Q_N < 1$), nothing happens at low temperatures because there are no nuclei present that could grow. Upon further heating, the first few nuclei that form can grow relatively rapidly. This leads to a GSD skewed to large grain sizes, i.e. a GSD with many small and a few large grains.

If both activation energies are equal (i.e. $Q_G/Q_N = 1$), the *ratio* of nucleation rate and growth rate does not depend on temperature, i.e. it remains constant throughout the transformation. This leads to a GSD which is isomorphous with a distribution obtained by isothermal transformations (shown with a thick solid line in Figure 2.4).

⁵Note that the GSD obtained upon heating for $Q_G/Q_N > 1$ will never entirely coincide with the GSD for site saturation, because, even though a large number of nuclei begins to grow at the same time, as for site saturation, here nucleation continues at a high rate during the “growth stage” of the transformation, different from site saturation.

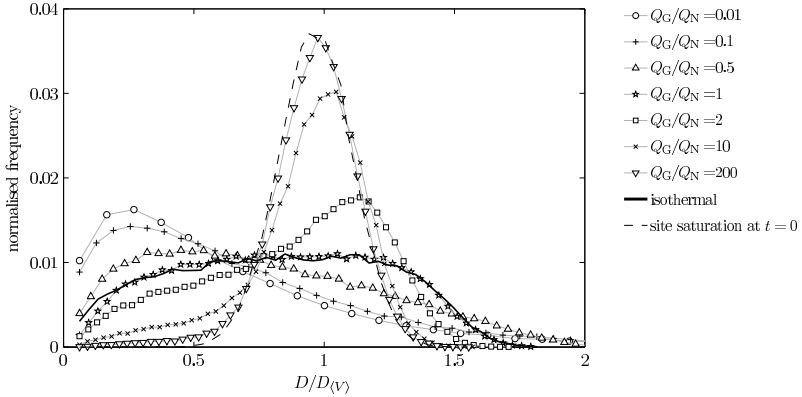


Figure 2.4: GSDs for transformations (continuous nucleation) upon isochronal *heating* as function of the ratio of the activation energies for growth and nucleation, Q_G and Q_N . The GSDs for isothermal transformation (continuous nucleation, solid line) and transformation with site saturation (dashed line) are shown as well. For used parameters, see Table 2.2 .

2.3.2 Isochronal Cooling

Upon cooling, the transformation starts at a temperature above 0 K, so nucleation and growth rates [cf. equation (2.6)] are nonzero at the beginning of the simulated transformations. Because of the exponential nature of the equations (2.6), the nucleation and growth rates are monotonically increasing with temperature and hence there is no “natural” starting temperature. Instead, a starting temperature must be chosen artificially. For the simulations of transformations upon heating, the natural starting temperature is 0 K (cf. section 2.3.1). Note that in the current model, the chemical driving force is large and therefore does not influence the kinetics, although its value may depend on temperature [see discussion above equation (2.6)]. For all simulations during cooling presented here, a starting temperature of 700 K was chosen.

In strong contrast with transformations upon heating, the cooling rate and the absolute values of the activation energies of nucleation and growth pronouncedly influence the GSDs resulting from transformations upon cooling. This partly is a trivial effect: For a fixed starting temperature, on the one

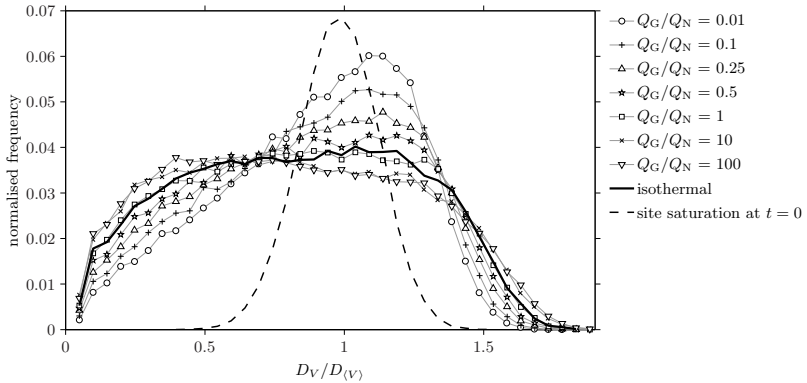


Figure 2.5: GSDs for transformations (continuous nucleation) upon isochronal cooling as function of the ratio of the activation energies for growth and nucleation, Q_G and Q_N . The GSDs for isothermal transformation (continuous nucleation, solid line) and transformation with site saturation (dashed line) are shown as well. The frequencies of the distribution for the site saturation case have been multiplied by $1/2$ to improve comparability. For used parameters, see Table 2.2.

hand, absolute values of the activation energies can be chosen “too large” so that only a sluggish transformation can be initiated, and because nucleation and growth rates decrease further during cooling, the transformation will not be able to complete (or to start at all). On the other hand, for “too small” absolute values of the activation energies, the transformation runs to completion in extremely short time, making the transformation effectively an isothermal one. Therefore, the following discussion is based on a consideration of only ratios of activation energies; absolute values of the activation energies were chosen such that the transformations can be compared for Q_G/Q_N varying over several orders of magnitude. The corresponding procedure was devised as follows.

1. T_0 and Φ are fixed.
2. For each ratio of the activation energies Q_G/Q_N , the absolute values of Q_G and Q_N are set to very small initial values.
3. The absolute values of Q_G and Q_N are increased by multiplication

with a certain factor until the reaction is not able to complete any more upon cooling.

4. Steps 2. and 3. are repeated several times, thereby improving the choice of initial activation energy values and reducing the multiplication factor in each consecutive iteration.

The results obtained on this basis are independent of the cooling rate. They are shown in Figures 2.5 and 2.6.

The simulations for transformations upon cooling lead to results strikingly different from those obtained for heating, for otherwise identical conditions (Tables 2.1 and 2.2). For cooling, large values of Q_G/Q_N lead to GSDs with their (less pronounced) maximum at small (normalised) grain sizes, whereas for small values of Q_G/Q_N GSDs are obtained with their maximum at large (normalised) grain sizes.

Upon cooling, the process with the higher activation energy ceases first. If this is nucleation (i.e. $Q_G/Q_N < 1$), all grains nucleated so far continue to grow which leads to a GSD of rather large grains of similar size (see Figure 2.5). This situation is similar to site saturation (pre-existing nuclei): very many nuclei are formed at the beginning of the transformation and subsequently grow simultaneously. Indeed, the GSDs for small values of Q_G/Q_N (Figure 2.5) are similar to the GSD for a transformation with pre-existing nuclei (but never fully approach it, cf. footnote 1). The nucleation rate at the end of the transformation has fallen to less than a tenth of its value at the beginning of the transformation (see Figure 2.6), whereas the growth rate is almost constant during the whole course of the transformation (quasi-isothermal growth).

If the activation energy for growth is higher and growth ceases first while nucleation continues, the reaction could only complete by filling up untransformed space with new non-growing nuclei, which is highly unlikely to succeed before the temperature drops to values making also further nucleation impossible. Therefore, transformations with $Q_G/Q_N > 1$ can only complete if the absolute value of Q_G is low enough, so that growth is possible over the whole course of the transformation. This implies that the absolute value of Q_N is even lower than Q_G ; evidently, for (very) low values of Q_N , quasi-isothermal nucleation occurs (see Figure 2.6).

If $Q_G/Q_N = 1$, the temperature dependencies of the nucleation and growth rate are the same, both rates decrease by the same amount during the transformation and hence the data points for $v(T)$ and $\dot{N}(T)$ coincide (see Figure 2.6 and cf. the results in Figures 2.4 and 2.5 for $Q_G/Q_N = 1$).

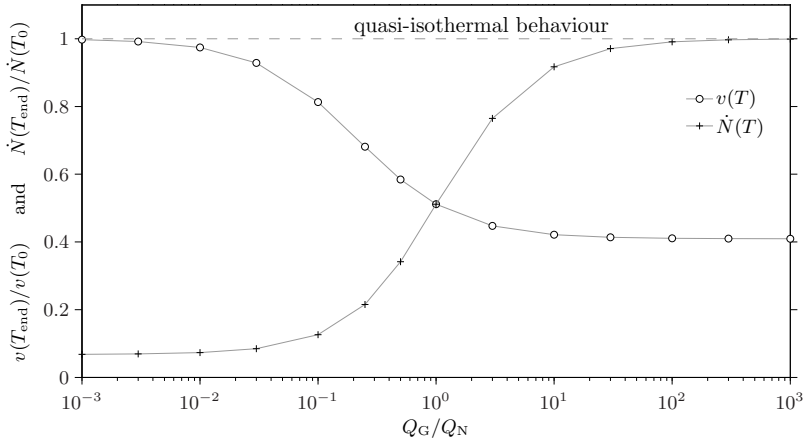


Figure 2.6: For transformations upon isochronal *cooling*, the ratio of the rates of growth at the beginning and at the end of the transformation, $v(T_{\text{end}})/v(T_0)$, (○) and the ratio of the rates of nucleation at the beginning and at the end of the transformation, $\dot{N}(T_{\text{end}})/\dot{N}(T_0)$, (+), both as function of the ratio of the activation energies of growth and nucleation, Q_G/Q_N .

2.3.3 Discussion

In this chapter, the focus is on transformations occurring in a distinctly supersaturated matrix, implying that nucleation and growth rates can be described by equation (2.6). Such transformations occur in practice upon heating from a quenched-in metastable state or, departing from an equilibrium state, upon cooling or heating (passing a phase-equilibrium temperature) so quickly that significant transformation only occurs at a temperature where the chemical driving force for the transformation has become large (cases of undercooling or superheating). In all cases in which the values for the nucleation and growth rates are finite (i.e. larger than zero) at the start temperature of the transformation, a similar discussion as in section 2.3.2 for transformations upon cooling can be given.

If the chemical driving force is not large (e.g. upon slowly passing a phase-equilibrium temperature from an equilibrium state), its influence on phase transformation kinetics is not negligible any more and equation (2.6) is not applicable. Then, the start temperature of the transformation (and of a sim-

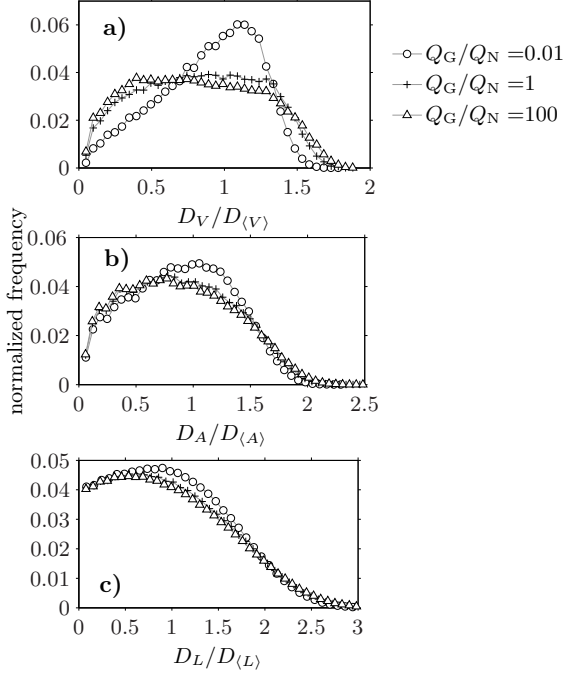


Figure 2.7: GSDs for three different ratios of activation energies (continuous nucleation and isochronal cooling). In a), the volume-weighted grain size is shown [cf. equation (2.10)], in b) the area-weighted grain size [cf. equation (2.11)] and in c) the grain size determined by the line-intercept method.

ulation thereof) is the phase-equilibrium temperature.

The results presented in this chapter have relevance for phase transformations in commercially interesting materials as these often take place employing cooling rates such that a large supersaturation drives the transformation.

The GSDs resulting from transformations upon cooling for three different ratios of growth and nucleation activation energies have been presented in three different ways in Figure 2.7: The histograms for volume-weighted grain size [cf. equation (2.10)], for area-weighted grain size [cf. equation (2.11)] and for line-weighted grain size are shown in Figures 2.7 a), b) and

c), respectively. The differences between the three GSDs caused by varying Q_G/Q_N is pronounced for the volume-weighted grain size, whereas the GSDs for the line-weighted grain size differ in a minor way. This is the case because, mathematically, the GSDs in c) are the product of folding the grain-volume distribution with the distribution that results for the line-weighted grain size of a single grain (of typical shape) [34]. Therefore, the GSDs in Figure 2.7 c) are smeared versions of the GSDs in Figure 2.7 a). The easy-to-apply line-intercept method is widely used but appears to be not sensitive enough to reveal the dependence of the phase transformation kinetics on the value of the ratio of activation energies of nucleation and growth. The volume-weighted GSD can only be obtained experimentally by laborious methods (e.g. using serial cross-sectioning) but evidently provides the preferred means to expose the kinetic mechanisms of the underlying phase transformation. On the other hand, distinction of different nucleation modes may already be possible by considering GSDs for line-weighted grain size: for example, site saturation leads to a characteristically narrow GSD much different from the broad GSD resulting from transformations with continuous nucleation (cf. Figures 2.4 and 2.5).

2.4 Conclusions

- The microstructure resulting from both isothermally and nonisothermally conducted phase transformations, controlled by specific nucleation, growth and impingement modes, can be simulated realistically on the basis of global rules derived from an analytical or numerical phase-transformation model.
- The grain-size distributions (GSDs), once expressed as function of the normalised grain size, can be characterised in particular by the ratio of the activation energy for growth and the activation energy for nucleation.
- The microstructures derived for transformations upon cooling and heating differ strikingly: When the ratio of activation energies of growth and nucleation is increased, the GSDs resulting for transformations upon heating show a shift of the most frequent grain size (the GSD maximum) from small to large size values. For transformations upon cooling, the opposite behaviour is observed: The most frequent grain size decreases when the ratio of activation energies of growth and nucleation increases. The GSD maximum is less pronounced in the case

of cooling than in the case of heating.

- The GSD differences upon heating and cooling are direct consequences of the temperature dependencies of the nucleation and growth rates: For transformations upon heating, both rates are virtually nil at the beginning and subsequently increase (with different rates), whereas for transformations upon cooling, both rates have finite (different) values at the beginning of the phase transformation and subsequently decrease, becoming virtually nil at different stages of transformation.
- The GSD for the volume-weighted grain size is best suited to exhibit the effect of variable ratio of the nucleation and growth activation energies on the phase transformation kinetics; the (smeared) GSD for line-weighted grain size may still be capable to expose the effect of differences in nucleation mechanisms.

Chapter 3

Simulation of the kinetics of grain-boundary nucleated phase transformations

3.1 Introduction

For nucleation-and-growth phase transformations, the assumption of homogeneous (i.e. spatially random) nucleation, even though often used in modelling, does not hold in many cases. Nucleation often occurs heterogeneously on container walls or on microstructural features of the parent phase like inclusions or defects, such as grain boundaries. This should be reflected in the modelling of phase transformations, since mean-field kinetic models are usually derived assuming homogeneous nucleation. This chapter is concerned with an investigation of the kinetics of phase transformations and the resulting microstructure, by means of geometric simulations, if nucleation occurs on grain boundaries of the parent phase.

First, kinetic models for random nucleation and for grain-boundary nucleation are briefly discussed, then the simulation method is described and finally, the influence of the main factors on the kinetics and resulting microstructure are discussed.

3.2 Kinetic Models

Nucleation-and-growth phase transformations with random, bulk nucleation can be modelled with mean-field kinetic models which go back to works by Johnson, Mehl, Avrami and Kolmogorov [5–7] (see also Ref. [8] for a recent review). These “JMAK-like” models all have in common that the assumption of a spatially random arrangement of nuclei allows to relate the real transformed (volume) fraction of a specimen, f , with the hypothetical, so-called extended fraction, f^{ex} , which is defined as the volume fraction of all growing grains if they could grow without impingement (i.e. if they could grow “through” each other). Thus:

$$df = (1 - f)dx_e. \quad (3.1)$$

The calculation of the extended transformed fraction can be done straightforwardly if specific models for nucleation and growth are adopted; i.e. the nucleation rate per unit volume of untransformed material, \dot{N}_V , and the growth rate v must be known. Additionally, the dimensionality, d , of the growth and the shape of the growing grains (expressed by the shape factor g) need to be known, as well as whether linear or parabolic growth prevails [expressed by the exponent m , which equals 1 for linear (e.g. interface-controlled) and 2 for parabolic (e.g. diffusion-controlled) growth]:

$$x_e(t) = \int_0^t \dot{N}_V(\tau) g \left(\int_\tau^t v(t') dt' \right)^{d/m} d\tau, \quad (3.2)$$

where $\dot{N}_V(\tau)$ refers to the grains nucleated at time τ , which grow with velocity v from time τ until the current time t . equation 1 cannot be used if nucleation occurs on grain boundaries. Cahn [11] proposed a model for nucleation on grain boundaries by approximating grain boundaries as planes which are randomly distributed in space. Since nucleation is supposed to occur randomly on these planes, the impingement of growing grains on *planes* can be described, in analogy to equation 1, by

$$dO = (1 - O)dO_e, \quad (3.3)$$

where O denotes the transformed area fraction on a plane (parallel to or on a grain boundary), and O_e the corresponding extended area fraction. Likewise, since planes are randomly distributed, the impingement of material growing *from different planes* can be described by equation 1. For such a model of grain-boundary nucleation, the nucleation rate needs to be expressed per unit area of grain boundary, \dot{N}_O ; the grain boundary area per unit volume is denoted by S_V^{GB} . For a detailed description of the model, see Refs. [2, 11]. In the case of linear growth of spherical product grains, Cahn's model is given by

$$f(t) = 1 - \exp \left\{ -S_V^{GB} \int_{-\infty}^{+\infty} \left[1 - \exp \left(- \int_0^t \pi (v^2(t-\tau)^2 - y^2) \dot{N}_O(\tau) d\tau \right) \right] dy \right\} \quad (3.4)$$

The assumption of randomly distributed planes in this grain-boundary nucleation model may not be a valid approximation of a realistic grain-boundary network.

3.3 Simulation Method

The method to simulate the kinetics of phase transformations and the resulting microstructure which is used in this work can be called geometric simulation method [12]. The corresponding algorithm discretises time in time steps and space in voxels (on a three-dimensional, cubic grid); see Ref. [35]. It needs input values for the nucleation and growth rate prevailing in the simulated specimen. For each time step, the number of nuclei that should emerge according to the nucleation rate is determined and as many nucleation positions are chosen; either randomly in the whole specimen or from a list of available nucleation sites (see below). For each nucleus, be it formed in the current or in a previous time step, the radius that the grain, originating from this nucleus, would have without interaction with other grains is determined by integrating the growth rate from the time of nucleation until the current time. Within a sphere of this radius around each nucleation position, it is checked for each voxel if it has already been transformed. If this is the case, transformation cannot take place. If the voxel is untransformed yet, it is transformed now and is assigned to the considered nucleus/grain. This algorithm thus corresponds to the assumption of hard impingement.

If nucleation doesn't occur randomly in the whole specimen, a list of permitted nucleation sites needs to be generated. In the simulations compatible with the assumptions of Cahn's model for grain-boundary nucleation, this is realised by generating randomly a certain number of planes cutting the simulation cube and by determining the voxels that are cut by each plane. For simulations using more realistic grain-boundary arrangements, two simulations are performed: First, a simulation with nuclei randomly distributed in the bulk is done and the microstructure (denoted "parent microstructure") resulting from this simulation is then used in a second simulation to investigate the effect of grain-boundary nucleation. A voxel of the parent microstructure is defined to be a grain-boundary site and hence a valid nucleation position in the second simulation ("parent→product transformation") if it has exactly two different grains in its neighbourhood (of 26 surrounding voxels).

In all simulations, interface-controlled (i.e. linear) growth is assumed. Nucleation is assumed to occur continuously in the untransformed volume (with one exception, where pre-existing nuclei are assumed). The temperature is either held constant during the transformation (i.e. isothermal annealing) or increased at a constant rate (i.e. isochronal annealing). Arrhenius-dependencies are assumed for the nucleation and growth rates with the activation energies Q_N and Q_G for nucleation and growth, respectively.

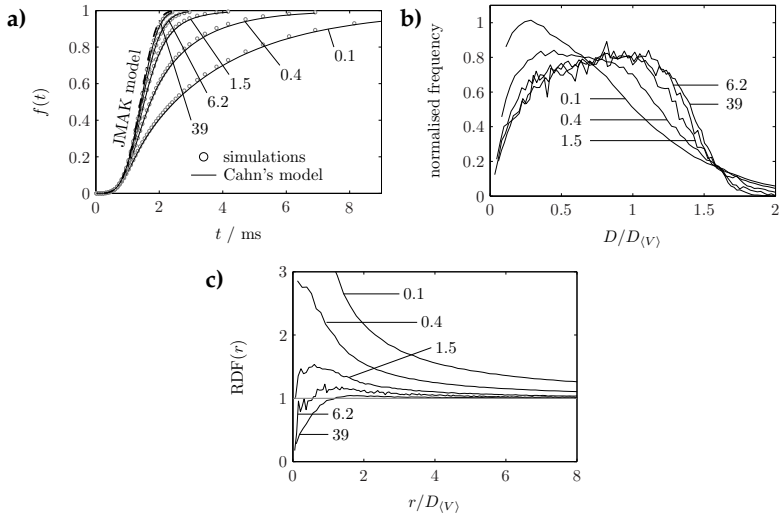


Figure 3.1: The results of simulations with random nucleation on randomly distributed planes for varied ratio S_V^{GB}/\dot{N}_O (values indicated in the figures). a) The transformed fraction as a function of time (symbols) together with the predictions of Cahn's model (solid lines) and a JMAK-like model (dash-dot line). b) The resulting grain-size distributions. c) The radial distribution function of nucleation positions.

3.4 Simulation Results

Influence of the GB area density. The influence of the grain boundary area density is revealed by the results shown in Figure 3.1 a) together with the predictions of Cahn's model (equations 1, 3 and 4) and a JMAK-like model (based on spatially random nucleation; equations 1 and 2) for the corresponding input parameters. Since S_V^{GB} and \dot{N}_O have opposing effects on the kinetics, the ratio S_V^{GB}/\dot{N}_O was varied while keeping the value of $S_V^{GB} \times \dot{N}_O = \dot{N}_V$ constant. This ensures that the JMAK-like model predicts the same kinetics for all simulations. For all input parameters, the simulations agree well with the predictions of Cahn's model.

For high values of the ratio S_V^{GB}/\dot{N}_O , the simulated phase transformation kinetics (as well as the prediction of Cahn's model) become identical to the prediction of the JMAK-like model; the smaller the ratio S_V^{GB}/\dot{N}_O is, the

slower the transformation and the larger the deviation from the prediction of the JMAK-like model becomes. The grain-size distributions resulting for the same set of simulations are shown in Figure 3.1 b). The smaller the ratio S_V^{GB}/N_O is, the broader the product grain-size distribution gets and the more its maximum moves towards small grain sizes.

Influence of the parent microstructure. Departing from various parent microstructures, the transformation was carried out using the same parent→product kinetics (isothermal transformations). By adjusting the length scale of the simulated parent microstructure, it was ensured that all simulations pertain to the same grain boundary area density.

The grain-size distributions of all employed parent microstructures are shown in Figure 3.2 a), including the (extreme) grain-size distribution that results if the space between randomly distributed planes is filled up and defined as grains. The resulting simulated kinetics are shown in Figure 3.2 b), together with the predictions by Cahn’s model and the JMAK-like model. All simulated kinetics lie in between these two extremes. Only the results of the simulation with nucleation on grain boundaries of a parent microstructure, the grain-size distribution of which is very broad and has its maximum at small grain sizes, comes close to the prediction by Cahn’s model. Generally, the broader the parent grain-size distribution is, the more the simulated kinetics deviates from the prediction of the JMAK-like model.

The grain-size distributions of the product microstructures are shown in Figure 3.2 c). They differ distinctly from the grain-size distribution that is obtained for a simulation with random nucleation in the bulk. The shape of the parent grain-size distribution doesn’t have a strong influence on the product grain-size distribution.

Influence of the parent→product kinetics. The results of the simulations for varied parent→product kinetics (parent microstructure generated by an isothermal transformation) are shown in a plot of the simulated transformed fraction versus the transformed fraction according to the JMAK-like model (Figure 3.3 a). Thus, any deviation from the diagonal in Figure 3.3 a) means a deviation from the kinetics according to the JMAK-like model. The normalised cumulative number of nuclei/grains, as generated in the simulation, has been plotted as function of the simulated transformed fraction in Figure 3.3 b). By comparing Figures. 3.3 a) and 3.3 b) it follows that the simulated kinetics deviate most from JMAK if the nucleation predominantly or entirely takes place at the beginning of the transformation.

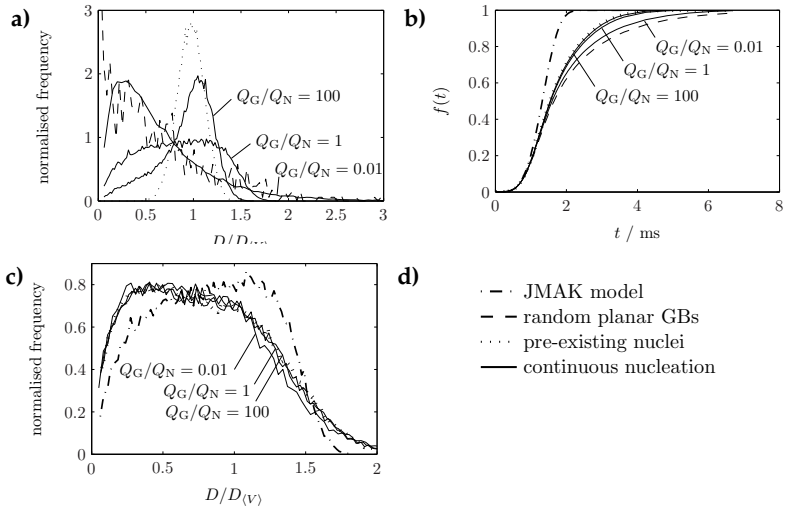


Figure 3.2: a) The grain-size distributions of parent microstructures for subsequent simulations. All were derived using the assumption of spatially random nucleation, but varying the parent kinetics. b) The resulting simulated parent \rightarrow product kinetics. For all calculations, the same constant nucleation and growth rates were assumed. c) The resulting grain-size distributions of the product microstructure.

3.5 Discussion

The radial distribution function of nucleation sites, $RDF(r)$, represents the probability of finding one nucleus at a certain distance, r , from another nucleus. It equals one for all r for a random arrangement of nuclei (ignoring the size of a nucleus). The $RDFs$ for the simulations presented in Figure 3.1 are shown in Figure 3.1 c). It can be seen that even for high ratios S_V^{GB} / \dot{N}_O , where the simulated kinetics coincide with the JMAK-like model, the RDF does not equal one for all r . This can be understood as follows. In the simulations, a constant nucleation rate per untransformed unit volume is assumed throughout the transformation. However, after the specimen has partially transformed, nuclei can only form in untransformed regions and hence can only occur *at a certain minimum distance* from the, already existing, nuclei. Therefore, a *negative* correlation between nucleation positions

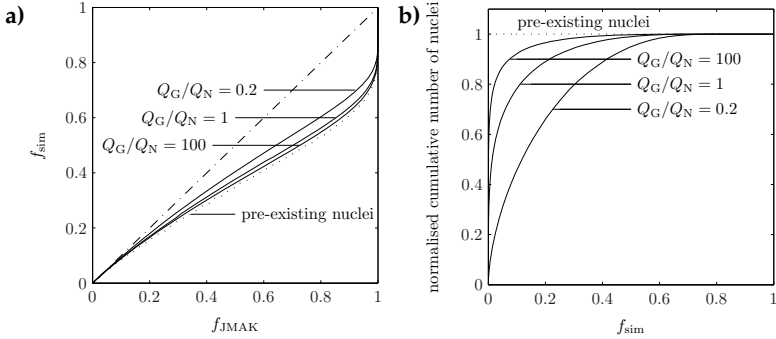


Figure 3.3: The results of simulations using the same product microstructure (derived using a constant nucleation and growth rate) and final number of nuclei, but varying the parent \rightarrow product kinetics. a) Simulated transformed fraction as function of the transformed fraction predicted by the JMAK-like model and b) normalised cumulative number of nuclei/grains during the simulation as function of simulated transformed fraction.

occurs, indicated by an *RDF* smaller than one at small distances between pairs of nuclei. A truly random arrangement can only be realised by adopting pre-existing nuclei (i.e. all nuclei are present before the onset of transformation). For decreasing ratios of S_V^{GB}/\dot{N}_O (and the same nucleation rate \dot{N}_V , see above), the same number of nuclei must form on a more and more restricted grain-boundary area and therefore nuclei are more likely to appear close to each other. This *positive* correlation of nucleation positions is exhibited in Figure 3.1 c) and is the reason for the retardation of the transformation kinetics as observed (Figure 3.1 a): The closer to each other nuclei form, the sooner they impinge which leads to slow transformation kinetics and a high number of small grains.

A similar reasoning can be used to explain that transformations nucleating on parent microstructures with a broad grain-size distribution with many small grains are relatively slow (Figure 3.2): Small parent grains lead to many nuclei which are close to each other and impinge early in the transformation. Moreover, for such parent microstructures, the last part of the transformation is further slowed down because there are a number of very large parent grains (which can be transformed only by product grains nucleated at grain boundaries of these grains).

If a substantial part of the nucleation occurs late during the transformation, the negative correlation of nucleation positions, as a consequence of the necessity that nucleation can only occur in untransformed regions, and the positive correlation of nucleation positions, due to their confinement to the remaining, unoccupied parent grain-boundary area, compensate each other partly, so the deviation from JMAK-like kinetics in such a case is not as strong as for pre-existing nuclei (see Figure 3.3).

3.6 Conclusions

The kinetics of grain-boundary nucleated phase transformations and the resulting grain-size distributions were analysed by means of geometrical simulations and compared with a JMAK-like model (assuming spatially random nucleation) and Cahn's model for grain-boundary nucleation. If the grain size of the parent microstructure is smaller than the grain size of the product microstructure (i.e. the ratio S_V^{GB} / \dot{N}_O is large), the kinetics and resulting microstructure is identical to results obtained assuming spatially random nucleation. If S_V^{GB} / \dot{N}_O is small, JMAK-like models and Cahn's model for grain-boundary nucleated transformations give upper and lower bounds for the development of the transformed fraction; both models cannot describe the simulated kinetics correctly. The transformation kinetics is most strongly influenced by grain-boundary nucleation if *i*) the parent microstructure has a broad grain-size distribution with many small grains and *ii*) if nucleation takes place predominantly at the beginning of the transformation.

Chapter 4

The kinetics of grain-boundary nucleated phase transformations: Simulations and modelling

4.1 Introduction

In the design of new materials and the optimisation of existing ones, phase transformations are of great importance, since, to a large extent, they control the microstructure and hence the properties of the material. Therefore, it is desirable to know the mechanisms and the kinetics of phase transformations [1]. Often, it is attempted to extract the kinetic parameters relevant to a phase transformation, as, for example, the activation energies of the nucleation and growth processes, from experimental data gained by observing the overall kinetics of the transformation [8,36]. Experimental techniques used include differential scanning calorimetry, dilatometry and X-ray diffraction. To infer kinetic parameters from experimental data, a kinetic model for the observed transformation must be adopted and fitted to the data. The kinetics of (nucleation-and-growth) solid-state transformations is most often described by the classical model by Johnson, Mehl, Avrami and Kolmogorov (JMAK) that treats the nucleation and subsequent growth of a product phase in the matrix of the parent phase until the whole parent phase is transformed [5–7]. The JMAK model holds only under severe constraints (see section 4.2); numerous extensions of the JMAK model are available in the literature, e.g. to incorporate the influence of a distribution of growth rates in a specimen [37] or to treat the kinetics of several simultaneous phase transformations [38]. For extensions to complex nucleation, growth and impingement modes, as well as arbitrary temperature-time programs, the modular kinetic model (MKM) approach described in Ref. [8] is particularly suitable. The present paper is focused on interface-controlled transformations during isothermal annealing and isochronal heating.

Fitting of kinetic models to experimentally determined data often fails, and this failure is usually attributed to the breakdown of one or several of the assumptions made in the derivation of the kinetic model. Such often made assumptions are a homogeneous, infinitely large specimen, isotropic growth of the product phase and homogeneous, i.e. spatially random nucle-

ation of product grains (For some examples out of a large body of literature, see Refs. [39–41]). Especially the last assumption is often violated: perfectly homogeneous nucleation is rarely observed in nature. Instead, nucleation often takes place on container walls or on microstructural features of the parent phase as inclusions or defects, in particular grain boundaries [2]. Heterogeneous nucleation, as on grain boundaries, becomes the more important the lower the driving force of the transformation is.

Several approaches are possible to describe the kinetics of grain-boundary nucleated phase transformations. First, within the framework of the MKM, impingement corrections different from the classical JMAK impingement equation can be used. Secondly, Cahn introduced a model in which parent-grain boundaries are described as randomly oriented planes. Both approaches are dealt with in this chapter. Recently, another approach, based on the time-cone method, which was first applied to the problem of non-random nucleation by Cahn [42], was developed [43,44]: Using the methods of statistical geometry, the kinetics of a phase transformation can be calculated if expressions for the (position-dependent) extended fraction can be derived which subsequently have to be integrated. This approach is cumbersome to apply in practice. Therefore, the present paper focuses on the MKM and Cahn models and extensions of the latter, which can be easily implemented without additional assumptions about the parent microstructure.

Using mesoscopic simulations, the influence of the spatial arrangement of nuclei on the phase-transformation kinetics can be investigated, while keeping all kinetic parameters, like the nucleation and growth rate, constant. Such simulations are therefore useful to decide which kinetic models are suitable to describe phase transformations exhibiting non-random nucleation.

Grain-boundary nucleated phase transformations were simulated in the past by a number of researchers using cellular automata or geometric algorithms [45–50]. With one exception (Ref. [49]), all these simulations were performed only in two dimensions. The parent microstructures ranged from simple arrangements such as a set of parallel lines as grain boundaries to parent microstructures generated by simulations with homogeneous nucleation assuming pre-existing nuclei or continuous nucleation. For the parent \rightarrow product kinetics, site saturation (at $t = 0$, i.e. pre-existing nuclei) was usually assumed. Neither the influence of the parent grain-size distribution, nor the influence of the various types of parent \rightarrow product kinetics was studied systematically in these investigations.

In this chapter, the kinetics of phase transformations which occur by nucleation on grain boundaries of the parent microstructure are revealed and

analysed by geometric simulations. Next, mesoscopic kinetic models are fitted to such simulated transformation-kinetics data. The available kinetic models which have been modified or specifically developed to describe grain-boundary nucleated phase transformations are presented in section 4.2. The employed simulation method is described in section 4.3. The results of the simulations and the results of fitting the above mentioned mesoscopic kinetic models to the simulated kinetics are presented and evaluated in section 4.4. Finally, the findings are discussed and resulting recommendations for the kinetic modelling of grain-boundary nucleated phase transformations are given in section 4.5.

4.2 Kinetic Models

4.2.1 Random nucleation

The classical JMAK model and extensions thereof are mean-field models which all assume homogeneous (spatially random) nucleation in the bulk of the parent phase [1,8]. This allows to relate the real transformed (volume) fraction of a specimen, f , with the hypothetical, so-called extended transformed fraction, x_e , which is defined as the volume fraction of all growing grains if they could each nucleate and grow in an infinitely large parent phase in the absence of other (growing) nuclei. Thus, for the case of randomly dispersed nuclei which grow isotropically, the real transformed (volume) fraction can be related to the extended transformed fraction according to

$$df = (1 - f)dx_e. \quad (4.1)$$

After integration, this becomes

$$f = 1 - \exp(-x_e). \quad (4.2)$$

The classical JMAK equation, that results by substitution of the appropriate expression of x_e in equation (4.2), pertains to isothermal transformations and is valid only if a high driving force prevails and only for a limited set of nucleation and growth mechanisms (in addition to the conditions holding for equation (4.1)). Instead, the transformed fraction can be calculated in the framework of the MKM approach for arbitrary time/temperature dependencies of the nucleation and growth rates and arbitrary annealing treatments, as follows.

The extended transformed fraction as function of time, t , and temperature T , where T can depend on t in case of non-isothermal transformations,

can be calculated straightforwardly by integrating the extended volume of grains nucleated at a certain time τ , denoted by $Y_e(\tau, t)$, times the nucleation rate per unit volume prevailing in the specimen at that time, $\dot{N}_V(T(\tau))$, with respect to the nucleation time τ

$$x_e(t) = \int_0^t \dot{N}_V(T(\tau)) Y_e(\tau, t) d\tau. \quad (4.3)$$

Adopting the case of isotropically growing grains, the extended radius of one grain, $R_e(\tau, t)$, can be obtained by integrating its growth rate/interface velocity from the time of nucleation, τ , until the current time, t . The extended volume of one grain can then be calculated by taking the radius to the d -th power (for d -dimensional growth) and by multiplying with an appropriate shape factor g ($= 4/3\pi$ for growing spheres):

$$Y^{\text{ex}}(\tau, t) = g [R^{\text{ex}}(\tau, t)]^d = g \left[\int_{\tau}^t v(T(t')) dt' \right]^d. \quad (4.4)$$

Note that this equation only holds for interface-controlled (linear) growth, which is the only growth mode considered in this thesis (For diffusion-controlled growth, the extended radius is calculated by taking the square root of the integrated interface velocity). Adopting additionally the case of random nucleation, the transformed fraction can be calculated from equations (4.1)-(4.4), provided the nucleation and growth rate of product-phase grains are known. Only if the specific, additional constraints of isothermal annealing and pre-existing nuclei *or* continuous nucleation are satisfied, the classical JMAK equation is recovered.

The above variant of the MKM approach with the same impingement correction as in the classical JMAK model (cf. equation (4.1)) will be called "MKM+rnd model", where "rnd" indicates "random nucleation" in the following.

4.2.2 Grain-boundary nucleation

If nuclei are not randomly distributed in the specimen, equation (4.1) does not hold any more, since the extended transformed fraction now varies spatially and cannot be approximated by a mean value any more [43]. If nucleus positions are positively correlated (clustered), i.e. if it is more likely than average to find a nucleus in the vicinity of another one, impingement is stronger than as described by equation (4.1), and the transformation will take longer to finish as predicted by the MKM+rnd model. This situation is for example realised if nucleation takes place on grain boundaries of the

parent microstructure. On the other hand, if nuclei are negatively correlated, e.g. if they are arranged on a regular grid or if there is a certain exclusion region around each nucleus in which no further nucleation can occur, impingement will be weaker than described by equation (4.1) and the reaction will finish faster than as predicted by the MKM+rnd model [51, 52]. It was therefore suggested [8–10, 40, 53] to modify equation (4.1) to take into account the “strength” of impingement. Two different modifications were proposed, namely using the impingement parameter ζ [8–10, 40, 53, 54],

$$df = (1 - f)^\zeta dx_e, \quad (4.5)$$

and using the impingement parameter ϵ [8, 31],

$$df = (1 - f^\epsilon) dx_e. \quad (4.6)$$

The impingement parameters ζ and ϵ do not have an *a priori* physical meaning, even though they have been interpreted in the past in terms of e.g. anisotropic growth, non-random nucleation and the Gibbs-Thompson effect [8, 31, 40]. For both parameters, as compared to “random nucleation”, a value larger than one leads to stronger impingement and a value smaller than one leads to weaker impingement. For $\zeta = \epsilon = 1$, the MKM+rnd model is recovered. For $\zeta = 2$, the so-called Austin-Rickett equation [55] results. The kinetic models using the MKM approach employing the above impingement equations will be referred to as “MKM+ ζ ” and “MKM+ ϵ ” models.

A more physical model for the description of non-random nucleation was developed by Cahn [11]. In this approach, parent-phase grain boundaries are approximated as *planes* which are randomly distributed in space. Nucleation takes place randomly on these planes and growth of product grains occurs isotropically into both adjacent parent “grains”⁶. The impingement problem is rendered tractable by approximating it as a combination of two separate impingement processes: First, the (lateral) impingement of grains originating from *one* grain boundary is addressed. Since nucleation occurs randomly on grain boundaries, this can be done using equation (4.1). Consider a planar grain boundary, a collection of spherical grains nucleated on this grain boundary, and a “probe plane” which is parallel to the grain boundary plane and a distance y away from it. At time t , the area of intersection of a grain, nucleated at time τ , with the probe plane is given by

$$O_e(t, \tau, y) = \pi \left(v(t - \tau)^2 - y^2 \right). \quad (4.7)$$

⁶Cahn’s approach is in principle able to treat nucleation on triple lines and vertices of grain boundaries; the discussion in this chapter is focused on grain-boundary (plane) nucleation.

This is an extended area, because impingement with the other grains nucleated on the considered grain boundary is not taken into account yet. Analogous to equation (4.3), the extended area fraction of all grains nucleated on the considered grain boundary, for the probe plane considered, can be calculated by multiplying with the nucleation rate and integrating over all nucleation times τ from zero to the current time

$$x_{e,O}(t,y) = \int_0^t O_e(t,\tau,y) \dot{N}_O(T(\tau)) d\tau \quad (4.8)$$

Here, $\dot{N}_O(\tau)$ is the (temperature-dependent) nucleation rate per unit area of (parent) grain boundary. It can be transformed to the nucleation rate per unit volume (as used in equation (4.3)) by multiplication with the parent grain-boundary area per unit volume, S_V^{GB} . Thus: $\dot{N}_V = \dot{N}_O S_V^{GB}$. The transformed area fraction on the probe plane can be obtained by applying equation (4.2):

$$f_O(t,y) = 1 - \exp(-x_{e,O}(t,y)). \quad (4.9)$$

Integration over all distances y of the probe plane yields the total volume fraction of all grains originated from one grain boundary

$$f^{\text{one GB}}(t) = \int_{-\infty}^{+\infty} f_O(t,y) dy. \quad (4.10)$$

After thus having accounted for the impingement of grains originated from *one* grain boundary (per unit area of this grain boundary), the effect of impingement of product phase grains growing from *all* grain boundaries is treated next. Because the grain boundaries are assumed to be randomly distributed in space, the volume of all grains nucleated on one grain boundary is multiplied by the grain-boundary area per unit volume, S_V^{GB} , and treated as the extended volume in this second impingement problem: $f^{\text{one GB}} S_V^{GB} \equiv x_e^{\text{all GBs}}$. Again an equation analogous to equation (4.1)/equation (4.2) is applied and finally, the total transformed volume fraction is obtained as

$$df = (1 - f) dx_e^{\text{all GBs}} \quad \text{or} \quad f = 1 - \exp(-x_e^{\text{all GBs}}). \quad (4.11)$$

In contrast to equations (4.5) and (4.6), which are of empirical nature, this impingement model has a physical background. Nevertheless, the assumption of randomly distributed *planes* as parent grain-boundaries in this model may not be a valid approximation for nucleation on a realistic grain-boundary *network*. Against this background, it appears reasonable to modify Cahn's model in a way similar to the prescriptions of equations (4.5) and (4.6). If random nucleation *on* grain boundaries can still be assumed, the

modification must be applied only to equation (4.11), concerned with the impingement of product phase regions *from different* grain boundaries. Equation (4.11) thus becomes

$$df = (1 - f)^\zeta dx_e^{\text{all GBs}} \quad (4.12)$$

or

$$df = (1 - f^\epsilon) dx_e^{\text{all GBs}} \quad (4.13)$$

In the following, these models will be referred to as “Cahn+ ζ ” and “Cahn+ ϵ ”, respectively.

4.2.3 Kinetic parameters

In the simulations, the temperature is either held constant during the transformation (isothermal annealing) or increased at a constant rate (isochronal heating). This complies with many practical cases of phase-transformation analysis. Thus, time and temperature are always connected by

$$T(t) = T_0 + \Phi t, \quad (4.14)$$

where T_0 is either the isothermal annealing temperature (with $\Phi = 0$) or Φ is the heating rate and T_0 is the start temperature.

The nucleation modes considered are “site saturation” (pre-existing nuclei of number density N_V^* or N_O^*) and “continuous nucleation” with a constant nucleation rate (in the untransformed material). In the latter case, the temperature (and thus, via equation (4.14), time) dependence of the nucleation rate is given by an Arrhenius equation (implying a large driving force for the transformation⁷),

$$\dot{N}_V(T(t)) \text{ or } \dot{N}_O(T(t)) = N^0 \exp\left(-\frac{Q_N}{k_B T(t)}\right), \quad (4.15)$$

where Q_N is the activation energy for nucleation (a genuine constant), k_B the Boltzmann constant and N^0 a pre-exponential factor. N^0 has the dimension $\text{time}^{-1}\text{length}^{-3}$ for homogeneous nucleation and $\text{time}^{-1}\text{length}^{-2}$ for grain-boundary nucleation.

In all simulations, interface-controlled growth of spherical grains has been adopted. The temperature dependence of the growth rate is expressed by (again implying a large driving force)

$$v(T(t)) = v^0 \exp\left(-\frac{Q_G}{k_B T(t)}\right), \quad (4.16)$$

⁷Equations (4.15) and (4.16) imply that the absolute value of the Gibbs energy difference of the product and parent phases is large as compared to $k_B T$.

where Q_G is the activation energy for growth and v^0 is a pre-exponential factor.

4.3 Geometric Simulations

4.3.1 Simulation Principle

Geometric simulation can be used to study the evolving microstructure resulting from phase transformations, provided the nucleation rate and the growth geometry and rate are known. After its introduction [12], this type of simulation has since been used e.g. to describe recrystallisation [14, 56], crystallisation of amorphous silicon [27] and the spinel-olivine phase transformation [57].

The details of the algorithms used in this work both to generate the parent microstructure (point 2. in section 4.3.2) and to simulate the phase-transformation kinetics with nucleation on grain-boundaries have been described elsewhere [35]; to facilitate understanding of this chapter only a synopsis of the main features is given here: The program uses discretised time (time steps) and space (voxels on a three-dimensional, cubic grid). For each time step it is determined how many nuclei are formed according to the nucleation rate. A corresponding number of positions for nucleation are chosen either randomly in the whole specimen or from a list of available nucleation sites (see below). If the voxel at the chosen position is still untransformed, the nucleation is performed by transforming the voxel and recording the nucleation time and successful position. Next, the radius to which the existing grains have grown from their nucleation time until the current time is looked up ($R^{\text{ex}}(\tau, t)$, cf. equation (4.4)) for all existing nuclei/grains. Each voxel in a sphere of radius $R^{\text{ex}}(\tau, t)$ around the nucleation position of a considered product grain is then transformed, unless it has already been transformed by another grain in a previous time step (i.e. hard impingement is accounted for). Finally, the transformed fraction for the time step concerned is calculated. Next, the time is advanced one time step and the procedure described is repeated, etc., until the whole specimen has fully transformed.

In order to simulate phase-transformations with nucleation on parent-phase grain boundaries, the following two-step procedure was adopted. First, the parent microstructure is generated and a list of voxels lying on parent-phase grain boundaries is compiled. A voxel is considered to lie on a grain boundary if it has exactly two different grains in its neighbourhood (of 26 surrounding voxels). Secondly, the list is used in the simulation of

phase-transformation kinetics with grain-boundary nucleation, for the determination of possible nucleation positions.

4.3.2 Construction of the parent microstructure

Parent microstructures were generated in three different ways:

1. By randomly placing planes in the simulation cube. This corresponds to the assumptions in Cahn's kinetic model. Any contiguous volume between the placed grain-boundary planes is conceived as a grain.
2. By performing a geometric simulation with homogeneous nucleation. The temperature program (isothermal annealing or isochronal heating), the nucleation mode (pre-existing nuclei or continuous nucleation) as well as the kinetic parameters (activation energies for nucleation and growth) were varied in order to obtain a large number of different parent grain-size distributions.
3. By performing a Monte-Carlo simulation of normal grain growth. Starting from a microstructure of one-voxel sized grains, a standard Monte-Carlo algorithm [58, 59] was used to simulate grain coarsening until the grain-size distribution, normalised with respect to the mean grain size, had become stationary.

Normalised grain-size distributions of all parent microstructures applied in this work are presented in Figure 4.1. The grain size is hereby defined as the diameter of a sphere, D , with the same volume as a grain, and normalised with respect to the diameter of a sphere with mean grain volume $D_{\langle V \rangle}$. It can be seen that a wide variety of parent grain-size distributions was considered, ranging from very sharp monomodal distributions (generated by a transformation with pre-existing nuclei) to skewed, broad distributions with many small and few very large grains (generated by a transformation during heating with continuous nucleation and $Q_G/Q_N = 0.01$ and qualitatively similar to randomly placed planes) and to distributions similar to a normal distribution (generated by normal grain growth simulations).

4.4 Results and evaluation

First, the simulated kinetics are directly compared with the kinetics as predicted by the MKM+rnd model (impingement as in the classical JMAK model)

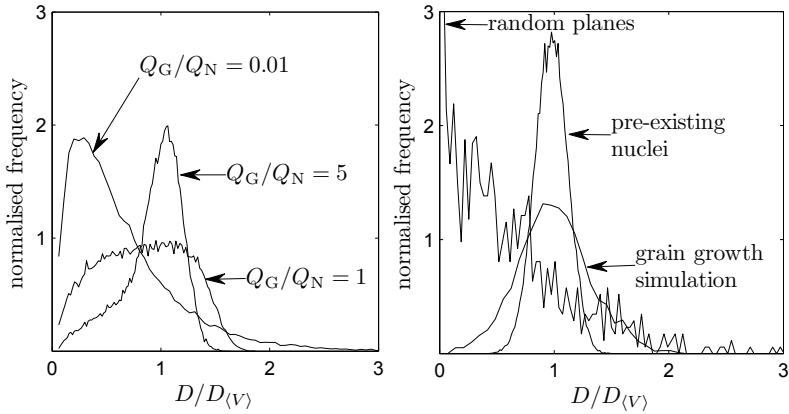


Figure 4.1: The normalized grain-size distributions of parent microstructures used in subsequent simulations of phase-transformation kinetics with nucleation on grain boundaries. Ratios Q_G/Q_N denote simulations of parent microstructure using continuous nucleation during isochronal heating with the given value for the ratio of the nucleation and growth activation energies.

and Cahn’s model using the same values for the kinetic parameters (section 4.4.1). Then, adopting the simulated kinetics as “experimental finding”, the kinetic models (cf. section 4.2) are fitted to the “experimental” data. This leads to fitted values for one or more kinetic parameters which are subsequently compared with the “true” parameters, i.e. the ones that were used as input parameters of the simulations (section 4.4.2–4.4.5).

All fits were performed using the Nelder-Mead simplex algorithm as implemented in the MATLAB language using the simulation inputs as start values for the fit. The mean squared error, MSE , which is used as an indicator of the quality of the model fit, is the average squared difference between simulated and model kinetics at each of the n time steps (typically $n \approx 100$ –150 per simulation)

$$MSE = \frac{1}{n} \sum_i^n (f_{\text{model},i} - f_{\text{sim},i})^2. \quad (4.17)$$

The difference between the value determined by fitting and the input value

of a kinetic parameter Z is reported as the relative error

$$\Delta Z / Z_{\text{input}} = \frac{Z_{\text{best fit}} - Z_{\text{input}}}{Z_{\text{input}}}. \quad (4.18)$$

4.4.1 General assessment of model appropriateness

The transformed fraction as function of time of grain-boundary nucleated (GBN) transformations, as simulated and as calculated according to the MKM+rnd model (i.e. impingement as in the classical JMAK model) and the Cahn model, is shown in Figure 4.2 a). The parent microstructure in this case was generated by a simulation on the basis of (homogeneous) continuous nucleation upon isothermal annealing. The subsequent GBN transformation proceeded on the basis of pre-existing nuclei upon isothermal annealing. The MKM+rnd model (i.e. assuming random nucleation) *overestimates* the transformed fraction: impingement for GBN transformations is more severe than for transformations with random nucleation, since the probability of finding two nuclei close together (on a grain boundary) is higher than finding two nuclei close together after random distribution. Also Cahn's model fails to correctly describe the simulated kinetics: it *underestimates* the transformed fraction. Randomly distributed planes often intersect each other at small angles, which in the simulation leads to nucleation positions which are very close to each other. In reality, such grain-boundary arrangements are unstable, since local equilibrium of interface tensions at grain-boundary edges and corners (usually) prevents very small dihedral angles [60]. Hence, impingement in Cahn's model is stronger than in (simulated) reality.

Next, the results of fitting of the MKM+rnd, MKM+ ζ and MKM+ ε models as well as the Cahn, Cahn+ ζ and Cahn+ ε models (cf. section 4.2) to the simulated kinetics are considered; examples are shown in Figure 4.2 b). For all MKM models, the nucleus density, N_V^* , and, where appropriate, the impingement parameter (cf. section 4.2.3), were used as fit parameters. Fitting the growth rate v at the same time does not lead to an improvement of the fit quality, since the two parameters cannot be varied independently for isothermal transformations [8]. For the Cahn models, the nucleus density, N_O^* , the growth rate, v , and, where appropriate, the impingement parameter, were used as fit parameters. Hence, the Cahn model incorporates one additional fit parameter. The corresponding differences between input ("real") values and the best-fit values of the kinetic parameters, as obtained for the above mentioned kinetic models, have been compiled in Table 4.1.

Clearly, the MKM+*rnd* model is unable to correctly describe the simulated kinetics. Cahn’s model does produce a reasonably good fit, but the values for the nucleus density and the growth rate obtained by fitting Cahn’s model are erroneous: they differ 72% and 42%, respectively, from the “real” values (see Table 4.1). The MKM+ ϵ model cannot correctly describe the simulated data. If ζ is used as impingement parameter for the MKM approach, a reasonably good fit is obtained. The modified Cahn models produce good fits upon incorporation of either one of both impingement parameters.

Fit results for other parent microstructures and various parent \rightarrow product kinetics (as described in section 4.2.3) are similar to the ones shown here: In all cases, the MKM model incorporating the impingement parameter ζ and the modified Cahn model are best suited to model the simulated data. In the following, these three models will be considered. Additionally, the original Cahn model is included in this comparison, recognising that this model provides a reasonable fit albeit for erroneous values of the kinetic parameters.

Table 4.1: The results of fitting various kinetic models to simulated phase-transformation kinetics. For the fit parameters v and N^* , the error relative to the input values of the simulation is given (cf. equation (4.18)). For the impingement parameters ζ and ϵ , the best-fit values are shown. Additionally, the quality of the fit is quantified by the mean squared error *MSE* (cf. equation (4.17)).

Model:	MKM+ <i>rnd</i>	Cahn	MKM + ϵ	MKM + ζ	Cahn + ϵ	Cahn + ζ
$\Delta N^* / N_{\text{input}}^*$	-61%	-72%	> 1000%	22%	117%	-20%
$\Delta v / v_{\text{input}}$	-	42%	-	-	23%	5%
ζ	-	-	-	2.11	-	0.75
ϵ	-	-	5×10^{-5}	-	2.56	-
$MSE \times 10^4$	57.6	1.3	21.1	2.8	0.19	0.05

4.4.2 Role of the ratio of the parent and product grain sizes

If all nuclei are present at the beginning of a GBN transformation, the volume density of product nuclei, N_V^* , follows from the nucleus density per unit area of parent phase grain boundaries, N_O^* , and the parent phase grain boundary area density S_V^{GB} : $N_V^* = N_O^* S_V^{\text{GB}}$ (cf. section 4.2.2). Hence, the same nucleus density per unit volume, and thus the same number of product

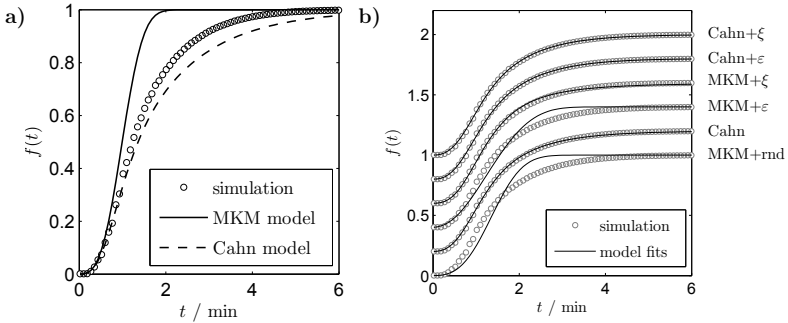


Figure 4.2: a) The simulated transformed fraction (f , symbols) for a phase transformation with nucleation on the grain boundaries of a parent microstructure generated by a simulation on the basis of continuous nucleation upon isothermal annealing. The simulated GBN phase transformation proceeded with pre-existing nuclei upon isothermal annealing. The predictions of the MKM+rnd model and the Cahn model for the same values of the kinetic parameters are shown as well (solid and dashed lines). b) Various kinetic models fitted to the same simulated degree of transformation data. Note that the curves have been shifted vertically, along the f -axis for clarity.

grains⁸, can be obtained by an infinite number of different combinations of N_O^* and S_V^{GB} , including a low nucleus density per unit grain-boundary area and a high grain boundary density and a high nucleus density per unit grain-boundary area and a low grain-boundary area density.

The results of simulations illustrating the influence of varying the ratio S_V^{GB}/N_O^* are shown in Figure 4.3. The parent microstructure was generated using continuous nucleation upon isothermal annealing; the parent \rightarrow product, GBN phase-transformation kinetics was simulated on the basis of pre-existing nuclei upon isothermal annealing. The results can be discussed as follows.

For a high ratio S_V^{GB}/N_O^* , the nuclei are spatially quasi-randomly distributed, since there are only very few product nuclei per parent grain. Therefore, the observed kinetics is well approximated by the one predicted for

⁸Note that this only holds strictly for the case of pre-existing nuclei. For continuous nucleation, employing the same nucleation rate \dot{N}_V , but varying the ratio S_V^{GB}/N_O^* does not lead to the exactly same number of product grains, because the geometry of impingement differs with varied S_V^{GB}/\dot{N}_O even though the nucleation rate per unit volume is identical.

random nucleation, i.e. the MKM+rnd model (in this case, the MKM+rnd model is equal to the classical JMAK model). For such a completed transformation, the parent-phase grain size is about as large as the product grain size or even significantly *smaller* and hence $D_{(V)}^{\text{parent}} / D_{(V)}^{\text{product}} \leq 1$. If the ratio S_V^{GB} / N_O^* is low, nucleation will be spatially highly non-random. Therefore, in this case, the observed kinetics deviates strongly from the MKM+rnd model prediction. Now, the parent-phase grain size is much *larger* than the product grain size ($D_{(V)}^{\text{parent}} / D_{(V)}^{\text{product}} > 1$). This behaviour is revealed in Figure 4.3 a), where the ratio S_V^{GB} / N_O^* is varied while keeping N_V^* (and v) constant.

Even though Cahn's model exhibits an increasing deviation from the MKM+rnd model (=classical JMAK model) with a decreasing ratio S_V^{GB} / N_O^* , it underestimates significantly the transformed fraction. Both models, the MKM+rnd model and the Cahn model only provide correct descriptions of phase-transformation kinetics for the case of a high ratio S_V^{GB} / N_O^* , i.e. for quasi-random nucleation (cf. Figure 4.3 a)).

Model fits of the MKM+ ζ model, the Cahn+ ζ model and the Cahn+ ϵ model to the simulated data are presented in Figure 4.3 c), d) and e). Each "real" simulated curve was fitted individually, using the impingement parameter (ζ or ϵ) as only fit parameter (For all other kinetic parameters, the input values of the simulations were used). The MKM+ ζ model can only correctly describe the simulated kinetics for moderate deviation from random-nucleation behaviour (i.e. for large values of S_V^{GB} / N_O^*). The best-fit value of ζ (see Figure 4.3 b)) increases about linearly with the ratio of parent to product microstructure grain size. The modified Cahn models provide good fits for the whole range of S_V^{GB} / N_O^* . The best-fit values of ζ and ϵ are nearly the same for each of the individual fits; if all curves are fitted simultaneously, the best values are $\zeta = 0.69$ and $\epsilon = 1.47$, respectively. Note that the modified Cahn model using ζ realises a better fit than the one using ϵ .

4.4.3 Role of the parent microstructure

Next, the parent microstructure was varied (pre-existing nuclei, continuous nucleation for variable Q_G / Q_N , normal grain growth; see Figure 4.1 in section 4.3.2) while adopting the same parent→product GBN kinetics: pre-existing nuclei during isothermal annealing. By appropriate adjusting of the grain size of the simulated parent microstructure, it was ensured that all simulations pertain to the same (parent) grain-boundary area density.

The resulting GBN transformation kinetics are shown in Figure 4.4 a). All

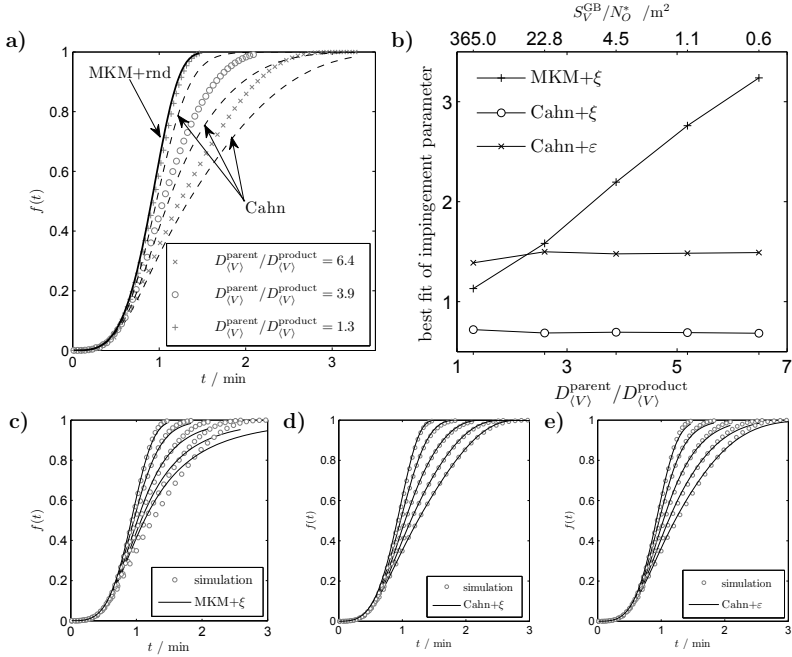


Figure 4.3: a) Results of a series of simulations of GBN phase-transformation kinetics for various values of the ratio $S_{V}^{\text{GB}}/N_{O}^*$ (symbols) together with the predictions by the MKM+rand model (solid lines) and the Cahn model (dashed lines); the resulting values for the ratio of the mean grain sizes of the parent and product microstructures have been indicated in the figure. For all simulations, $N_{V}^* = N_{O}^* S_{V}^{\text{GB}}$ was constant. b) The best-fit values of the impingement parameters ξ and ϵ when fitting the kinetic models indicated to the simulated data using the impingement parameter as only fit parameter. The corresponding model fits are shown in c) MKM+ ξ , in d) Cahn+ ξ and in e) Cahn+ ϵ .

simulated results for variable parent microstructure lie in between the prediction of the MKM+rand model and the Cahn model. Generally, the broader the parent grain-size distribution is, the more the simulated kinetics deviates from the prediction of the MKM+rand model. The simulation for a par-

ent microstructure with a broad grain-size distribution with (few) very large and many small grains comes close to the prediction by Cahn's model (i.e., the assumption of randomly distributed planes as parent microstructure).

The best-fit values for the impingement parameter and the relative error in the fit parameters (equation (4.18)) and the *MSE* for the whole fitted curve (equation (4.17)), as averages for all fits for every model, are shown in Figure 4.4 b). The used fit parameters are the density of pre-existing nuclei, N_V^* or N_O^* , and, where appropriate, the growth rate v and the impingement parameter (ζ or ϵ). Even though the relative error of the fitted parameters is small for the MKM+ ζ model, the quality of its fits is lower than those for the modified Cahn models (cf. the *MSE* values shown in Figure 4.4 b). The unmodified Cahn model, even though it shows a reasonably good quality of fit, leads to very large errors for the values of the fitted kinetic parameters. The modified Cahn model using ϵ produces very good fits, however shows a very large spread for (and thus errors in) the values of the fitted kinetic parameters. In particular, the impingement parameter ϵ varies widely if the parent microstructure is changed. The modified Cahn model using ζ shows the best quality of fit and the fitted kinetic parameters show only a moderate spread around the true values.

4.4.4 Role of the type of GBN transformation kinetics

The influence of the variation of the parent→product GBN transformation kinetics was investigated, for the same parent microstructure, by varying the nucleation mode and type of annealing. Thus, (i), the cases of pre-existing nuclei and continuous nucleation, both during isothermal annealing, were considered, and (ii) the case of continuous nucleation during isochronal heating was investigated for various ratios of the activation energies of growth and nucleation, Q_G/Q_N , namely $Q_G/Q_N = 0.01$ (most nucleation near the end of the transformation), $Q_G/Q_N = 1$ (equivalent to isothermal annealing⁹) and $Q_G/Q_N = 5$ (most nucleation at the beginning of the transformation, approaching the case of pre-existing nuclei [35]). In all simulations, the nucleation rate was adjusted such that the same final number of product grains and hence the same value for the ratio $D_{(V)}^{\text{parent}}/D_{(V)}^{\text{product}}$ resulted. The parent microstructure was generated by adopting continuous nucleation upon isothermal annealing.

⁹If the activation energies for nucleation and growth are identical, then the nucleation and growth rates increase at the same pace with rising temperature. Then, upon non-isothermal annealing, the same microstructure as for isothermal annealing results [35].

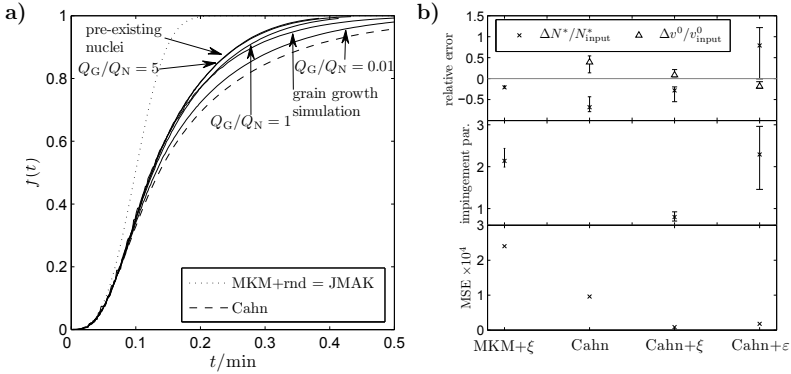


Figure 4.4: a) The transformed fraction as function of time for the same parent \rightarrow product kinetics, but variable parent microstructure as described in section 4.3.2 together with the transformed fraction as predicted by the MKM+rnd model (dotted line) and the Cahn model (dashed line). b) The mean best-fit values for the impingement parameters and the relative errors in the fit parameters (equation (4.18)) and the MSE (equation (4.17)) for the fitting of four different models. The fit parameters are the nucleation density, N^* , and, where appropriate, the pre-exponential parameter of the growth rate, v^0 , and the impingement parameter (ξ or ε). The error bars shown for the impingement parameters and the relative errors comprise the whole range of obtained best-fit values for all simulations.

The influence of grain-boundary nucleation (i.e. the deviation from random nucleation as described by the MKM+rnd model) is found to be strongest for transformation kinetics in which most (or all) nuclei are formed at the very beginning of the transformation (see Figure 4.5 a). This can be understood by considering that in transformations where a substantial amount of nucleation occurs late in the transformation, new nuclei can only form in untransformed regions and hence occur only at a certain minimum distance from the, already existing, nuclei. This leads to a *negative* correlation between nucleation positions for phase transformations simulated on the basis of continuous nucleation [61].

The simulated transformation curves were fitted using the pre-exponential factors N^0 and v^0 (cf. equations (4.15) and (4.16)) as fit parameters. For pre-

existing nuclei, $N^* \equiv N^0$. For the activation energies for nucleation and growth, Q_G and Q_N , the input values of the simulations were used. The quality of the best-fit values for the kinetic parameters can be judged considering Figure 4.5 b). The MKM+ ζ model and the unmodified and modified Cahn model are able to describe the simulated kinetics well. The fit quality is lower for the MKM+ ζ model than for the modified Cahn models, however the error in the fitted kinetic parameters is small. The unmodified Cahn model produces a large error in the fitted kinetic parameters and the modified Cahn model using ε leads to a large variation in the values for the fitted kinetic parameters. As indicated by its *MSE* value, the best fit is obtained with the modified Cahn model using ζ . It also produces small errors in, and a low spread of the values for the fitted kinetic parameters.

4.4.5 Simultaneous fitting of kinetic models to a set of non-isothermal transformation runs

In practice, models are fitted to experimental data in the absence of advance knowledge of values of kinetic parameters as activation energies, pre-exponential factors etc. Usually, a series of experiments at different isothermal holding temperatures or with different heating/cooling rates is performed and the kinetic transformation model is fitted simultaneously to all experimental results in order to determine values for the kinetic parameters, in particular for the activation energies of nucleation and growth (results of kinetic model fitting to individual transformation experiments are usually unreliable; i.e. the fitting is “insensitive” to changes in the kinetic parameters to be fitted) [8].

If the values of the activation energies of nucleation and growth differ, then the final number of product grains depends on the employed heating rate (cf. footnote 9 in section 4.4.4). If the activation energy for nucleation is smaller than for the activation energy for growth, as in the simulations performed here, nucleation can take place upon heating already at temperatures at which growth is negligibly slow (cf. equations (4.15) and (4.16)). Changing the heating rate changes the time spent in this temperature range and therefore the final number of product grains. It was shown in section 4.4.2 that it is not possible to describe a set of transformation kinetics data pertaining to different ratios of the grain sizes $D_{(V)}^{\text{parent}}/D_{(V)}^{\text{product}}$ with the MKM+ ζ model using a common value of the impingement parameter ζ (cf. Figure 4.3 b). Therefore, the desired fitting of the kinetic model to *simultaneously* all transformation runs of a set of different heating rates,

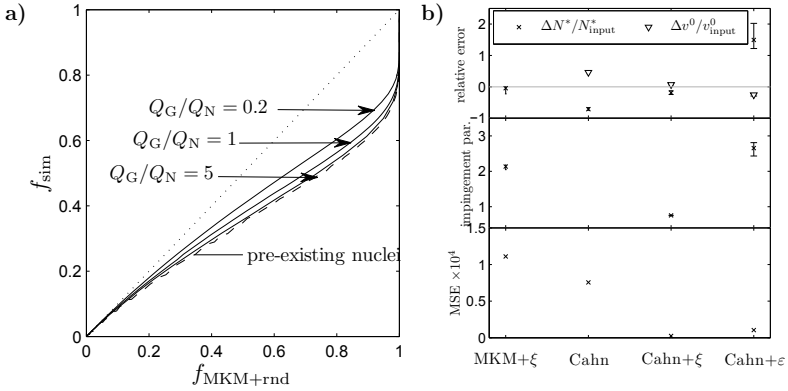


Figure 4.5: a) The simulated transformed fraction as function of the transformed fraction predicted by the MKM+rand model for simulations using the same parent microstructure but various parent→product kinetics (non-isothermal), together with the transformed fraction as predicted by the corresponding MKM+rand model (dotted line) and the Cahn model (dashed line). b) The mean best-fit values for the impingement parameters and the relative errors in the fit parameters (equation (4.18)) and the MSE (equation (4.17)) for the fitting of four different models. The fit parameters are the pre-exponential factors for nucleation, N^0 , and, where appropriate, for the growth rate, v^0 and the impingement parameter (ξ or ε). The error bars shown for the impingement parameters and the relative errors comprise the whole range of obtained best-fit values for all simulations.

in order to obtain reliable values for the activation energies for nucleation and growth, is unlikely to be successful using the MKM+ ξ model.

Results obtained by simulating GBN transformation kinetics adopting continuous nucleation (with $Q_G/Q_N = 3$), departing from a parent microstructure generated by continuous nucleation upon isothermal annealing, are shown for isochronal annealing at various heating rates in Figure 4.6, together with the fitted transformation curves according to the MKM+ ξ , Cahn and Cahn+ ξ models. The values of the fitted kinetic parameters, Q_G , Q_N and the impingement parameter, have been gathered in Table 4.2.

As expected, a simultaneous fit to all simulated GBN transformation curves

at different heating rates is not well possible for the MKM+ ζ model (see Figure 4.6 a)); the fitted values of the activation energies Q_G and Q_N differ strongly from the input values of the simulations. The quality of the fits and of the values of the fitted kinetic parameters as obtained for the modified and unmodified Cahn models is very much better, in particular in case of the modified Cahn model using ζ as impingement parameter (see Figure 4.6 b) and c) and Table 4.2).

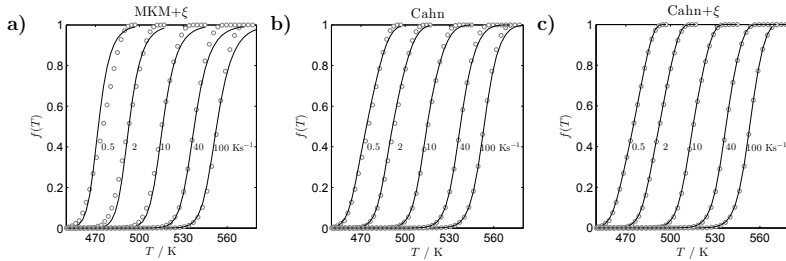


Figure 4.6: Transformed fraction as function of temperature for a series of simulations of grain-boundary nucleated transformation kinetics (symbols) with identical kinetic parameters (continuous nucleation; $Q_G/Q_N = 3$), but variable heating rate (indicated in the figure) with corresponding model fits (lines). The fit parameters are the activation energies Q_G and Q_N and, where appropriate, the impingement parameter ζ ; all curves were fitted simultaneously. The fitted models are a) MKM+ ζ , b) Cahn and c) Cahn+ ζ .

4.5 General discussion

The simulations of GBN phase transformations show that neither the MKM+ ζ model (impingement as in the classical JMAK model) nor the Cahn model correctly describes the kinetics of such phase transformations when using the same kinetic parameters as in the simulations. Both models depart from “random” nucleation behaviour which is generally incompatible with grain-boundary nucleated transformations. It has been shown that incorporating the non-random nature of the nucleation process in the kinetic model leads to a good description of the transformation kinetics, in particular by the MKM+ ζ and Cahn+ ζ models.

Table 4.2: The results of fitting various kinetic models to, simultaneously, a set of simulated phase-transformation runs at different heating rates. For the fit parameters Q_G and Q_N , the relative error, with respect to the input values of the simulation, is given (equation (4.18)). For the impingement parameters ζ and ϵ , the best-fit values are shown. The quality of the overall fit is quantified by the mean squared error MSE (equation (4.17)).

Model fit:	MKM+ ζ	Cahn	Cahn + ζ	Cahn + ϵ
$\Delta Q_G / Q_{G,\text{input}}$	23%	-1%	< 1%	< 1%
$\Delta Q_N / Q_{N,\text{input}}$	-158%	5%	< 1%	-1%
ζ	2.84	-	0.71	-
ϵ	-	-	-	1.39
$MSE \times 10^3$	50.6	7.1	0.6	1.1

Since there is no physical background for the use of both impingement parameters ζ and ϵ , neither of them can be judged to be “better” or “worse” by criteria other than their ability to correctly describe experimentally observed kinetics. The present work indicates that the MKM+ ϵ and the Cahn+ ϵ models are both not suitable to model grain-boundary nucleated phase transformations.

The MKM+ ζ model, using the ζ impingement parameter, only produces good fits if the deviation from random nucleation is not too large. The best-fit values obtained, however, are in good agreement with the “real” values, even if the transformation curves are not very well described. In this model, the value of the impingement parameter ζ depends on the ratio $D_{(V)}^{\text{parent}} / D_{(V)}^{\text{product}}$ (see Figure 4.3). Therefore, a simultaneous fit to a series of simulated grain-boundary nucleation transformation runs with varied heating rates (and continuous nucleation) leads to erroneous results for the fitted kinetic parameters.

The here proposed modified Cahn model using the impingement parameter ζ (Cahn+ ζ model) can correctly describe the simulated time-dependence of the transformed fraction for all considered parent grain-size distributions and parent \rightarrow product GBN transformation kinetics and the values of the fitted kinetic parameters show the smallest deviations from the input values of the simulations. For a given parent microstructure, the best-fit value of ζ is constant for all ratios $D_{(V)}^{\text{parent}} / D_{(V)}^{\text{product}}$ and all parent \rightarrow product kinetics. Therefore, transformation curves recorded at various heating rates

can be successfully fitted simultaneously.

From these considerations, it can be concluded that the here proposed modified Cahn model, using the impingement parameter ζ , is best suited to model the kinetics of GBN phase transformations.

Evidently, this outcome is consistent with the recognition that in the original Cahn model and in the here proposed modified Cahn model, grain-boundary nucleation is specifically modelled (i.e. accounted for), whereas the MKM+ ζ model is a general kinetic model for transformation kinetics in case of non-random nucleation, not specifically dedicated to grain-boundary nucleation as nucleation mode.

However, before favouring application of the Cahn+ ζ model to practical cases, it should be realised that the Cahn model needs one additional parameter (as compared the the MKM+ ζ model), namely the grain-boundary area density of the parent phase. In the here presented model fits, it was assumed that the value for this parameter is known. In practice, it can be obtained in the fitting procedure or experimentally by stereological methods, especially in case of transformations for which the parent phase can be examined, i.e. transformations during heating or from a (e.g. quenched-in) supersaturated state which is stable at room temperature. This is not possible for transformations occurring upon cooling from a high-temperature phase. In this latter case, data on the final number of product grains can be incorporated in the fit procedure as an additional constraint in order to improve the fit quality [36].

4.6 Conclusions

- The MKM+rnd model (impingement as in the classical JMAK model and identical to the classical JMAK model upon isothermal annealing) is unable to describe the kinetics of *grain-boundary nucleated* phase transformations: it overestimates the transformed fraction and cannot be fitted successfully to simulated transformation curves.
- The modular kinetic model incorporating the impingement parameter ζ , MKM+ ζ , can well describe the simulated kinetics, provided the deviation from random nucleation is not too strong and provided each simulated transformation curve is fitted individually.
- The Cahn model underestimates pronouncedly the transformed fraction in reality. Using kinetic parameters as fit parameters, reasonable fits are possible, however the values of the kinetic parameters

obtained by such fits deviate strongly from the “real” values.

- The here proposed modified Cahn+ ζ model can well describe grain-boundary nucleated transformation kinetics with small deviations of the fitted kinetic parameters from “real” values (i.e. simulation inputs); for the same parent grain-size distribution, the same value for the impingement parameter ζ results for a wide range of values for the ratio of the parent and product grain sizes, $D_{\langle V \rangle}^{\text{parent}} / D_{\langle V \rangle}^{\text{product}}$.
- It is therefore recommended to use the Cahn+ ζ model when attempting to infer values for kinetic parameters from experimentally determined grain-boundary nucleated phase transformation kinetics. If the deviation from random-nucleation behaviour is not too large, also the MKM+ ζ model is suitable for this task. The MKM+ ζ model, as an advantage, requires one less kinetic parameter (to be used as fit parameter or to be determined in advance).

Chapter 5

Kinetics of interface-controlled phase transformations: atomistic and mesoscopic simulations

5.1 Introduction

In many classes of materials, the microstructure and thus many properties are determined (tuned) by invoking phase transformations during the manufacturing process. Therefore it is important to gain knowledge not only about the stable or metastable phases prevailing under certain conditions (i.e. understanding the thermodynamics of the system under consideration), but also about the kinetics (i.e. the time and temperature dependencies) of the reactions which lead to them. The study of phase transformation kinetics has been undertaken for many decades [2].

Even though the general characteristics of many phase transformations are known since a long time, there are numerous open questions on issues of cardinal importance. This pertains to diffusion-controlled phase transformations, where the interplay of partitioning elements and the moving inter-phase boundary is still only partially understood [62, 63], and also holds for interface-controlled transformations, where the interface mobilities are largely determined in an empirical manner [64].

In the last years, computer simulations have become an indispensable tool to study phase transformation kinetics. On the *atomistic* length scale, they provide a detailed look at the movement of individual atoms at and across a moving interface, which is experimentally not possible. On the *mesoscopic* length scale, they lead to a predictive description of the microstructural development of materials. On the basis of such simulations, a link can be made between experimentally observed transformation kinetics and the resulting microstructure.

This chapter intends to give an overview over of recent research results of our group concerning computer simulation of interface-controlled phase transformations. After a short introduction to the essence of the modular phase transformation kinetics model (section 5.2), work on atomistic sim-

ulation of interface movement by kinetic Monte Carlo simulations will be highlighted (section 5.3). It will be shown how material properties like the activation energy for interface movement can be understood through these simulations. Subsequently, work on mesoscopic microstructure simulations will be presented (section 5.4). It will be explained how the microstructure under control of a given kinetic model can vary depending on the path followed in time-temperature space. Additionally, the ability of these mesoscopic simulations to expose the effects of non-random nucleation will be demonstrated.

5.2 The modular model for transformation kinetics

The kinetics of nucleation-and-growth phase transformations is usually described within the framework of Johnson-Mehl-Avrami-Kolmogorov (JMAK) type equations, which hold only for a very limited set of transformation conditions and nucleation and growth models. An extension of this approach incorporating arbitrary time-temperature dependencies and complex nucleation and growth mechanisms is provided by the Modular Kinetic Model (MKM) approach; see Refs. [1, 8]. For a most recent application to an interface-controlled, martensitic phase transformation, see Ref. [65].

The geometric simulations to be discussed in section 5.4 depart from an underlying kinetic model. To this end, the MKM approach can be well employed. Therefore, it will be briefly introduced in this section.

The basic concept of both the JMAK model and the MKM is to first calculate the so-called extended transformed volume, which is the volume of grains if they could each nucleate and grow in an infinitely large parent phase in the absence of other (growing) nuclei, leading to the extended transformed fraction, x_e , and then to apply an impingement correction equation to arrive at the transformed volume fraction, f . In the JMAK model, nuclei are assumed to be randomly dispersed and to grow isotropically. In this case, the impingement correction equation can be obtained by integrating

$$df = (1 - f)dx_e, \quad (5.1a)$$

which leads to¹⁰

$$f = 1 - \exp(-x_e). \quad (5.1b)$$

¹⁰In the JMAK model, the transformation is assumed to proceed isothermally and the only allowed nucleation models are “site saturation” (at $t = 0$) and “continuous nucleation”. Then, equation (5.1) becomes the well-known result $f = 1 - \exp(-kt^n)$ with constants k and n . Models which also describe nonisothermal transformations and depart from a wide range of nucleation models, but retain the assumption of randomly dispersed nuclei growing isotropically, are termed JMAK-like models. In these models, equation (5.1) becomes

Since it is often found that, especially for late stages, phase transformations cannot be well described by the impingement equation given above, modifications to equation (5.1b) have been proposed [1, 8]:

$$df = (1 - f)^{\zeta} dx_e \quad \text{with } \zeta > 0 \quad (5.2a)$$

or

$$df = (1 - f^{\varepsilon}) dx_e \quad \text{with } \varepsilon > 0 \quad (5.2b)$$

in particular in case of anisotropic growth and non-random nucleus distribution, respectively. The impingement parameters ζ and ε hereby don't have a clear physical meaning. However, it will be shown that their usage is beneficial if kinetic parameters have to be extracted from experimental data (see section 5.4.3).

In the MKM, separate models for nucleation, growth and impingement can be employed in any combination (e.g. for impingement, equation (5.1) or (5.2a) or (5.2b) or ... can be used) and arbitrary time-temperature programs can be described. The extended transformed volume fraction, x_e , which is the extended transformed volume divided by the specimen volume, is given by

$$x_e(t) = \int_0^t \left(\dot{N}_V(\tau) \left(g \int_{\tau}^t v(t') dt' \right)^{d/m} \right) d\tau \quad (5.3)$$

with \dot{N}_V as the nucleation rate per unit volume, v as the interface velocity and g as a particle-geometry factor ($g = 4/3\pi$ for growing spheres; $g = 1$ for growing cubes). If grains are assumed to grow in three dimensions, the dimensionality parameter d equals three and for linear growth (which prevails for interface-controlled phase transformations) the growth mode parameter m equals unity. For many nucleation and growth models, the integrals in equation (5.3) have to be solved numerically.

From equation (5.3), it can be seen that the two main ingredients of the kinetic model, apart from the impingement equation, are the models for the nucleation rate and the interface velocity. For nucleation, several models are available. The simplest ones are pre-existing nuclei (site saturation at $t = 0$) and continuous nucleation. For the case of continuous nucleation (implying a high driving force), the nucleation rate exhibits an Arrhenius-type temperature dependence

$$\dot{N}_V = N_0 \exp \left(- \frac{Q_N}{RT} \right). \quad (5.4)$$

$f = 1 - \exp(-k(t)t^{n(t)})$ (isothermal transformations) and $f = 1 - \exp(-\beta^n)$ (isochronal transformations), where β is the so-called path variable [1, 8].

Classically, the interface velocity is given by

$$v(T) = M_0 \exp\left(-\frac{Q_G}{RT}\right) \left[1 - \exp\left(\frac{\Delta G}{RT}\right)\right], \quad (5.5)$$

with $-\Delta G$ as the driving force of the transformation, and Q_G as the activation energy for interface movement (i.e. the activation energy of the interface mobility $M = M_0 \exp(-Q_G/RT)$). ΔG is a thermodynamical material property which is usually well-known or which can be determined experimentally. The interpretation of Q_G is complicated (see section 5.3).

After the nucleation and growth modes have been identified and substituted into equation (5.3), and after substitution of the resulting expression of x_e in the variant of equation (5.1) or (5.2) compatible with the identified impingement mode, a kinetic model has been obtained which is able to describe the evolution of the transformed fraction, f , as function of time or temperature. The choice of models for nucleation, growth and impingement thus determines the expected phase transformation kinetics. The chosen model set also determines which microstructure develops as the outcome of this phase transformation, as will be shown in section 5.4.2 using geometric simulations.

Fitting of model calculated values of f to corresponding experimental data yields values for the kinetic parameters. Usually, the activation energies are of main interest. The interpretation of values obtained for these energies is in many cases not straightforward. In the case of interface-controlled transformations, they are often compared with the activation energy for grain-boundary diffusion. The rationale behind this comparison is that a jump across a boundary between a growing grain and the matrix into which it is growing, i.e. a jump furthering transformation, should be comparable to a jump along this boundary, i.e. a jump effecting grain-boundary diffusion. However, the values obtained for Q_G can significantly differ from experimentally observed activation energies for diffusion. It is therefore interesting to conduct atomistic simulations in order to gain more insight into the atom-jump processes occurring at and near a moving parent/product interface (see the next section).

5.3 Atomistic Simulations

5.3.1 Simulation algorithm

Phase-transformation simulations at the length scale of an atom are usually performed with either Molecular Dynamics algorithms (MD) or kinetic

Monte-Carlo algorithms (kMC). While both methods rely on the availability of interaction potentials to describe the energy of individual atoms as function of their position relative to neighbouring atoms, the algorithms which advance the simulations are quite different. In MD simulations, the trajectory of each atom is tracked, whereas kMC simulations only allow jumps of atoms between predefined, fixed lattice positions. Therefore, kMC simulations are able to cover larger systems and much longer simulated times than MD simulations and are thus suitable to simulate phase transformations.

In the work presented here [66–69], kMC simulations were used to analyse the interface-controlled, allotropic γ (fcc; austenite) $\rightarrow \alpha$ (bcc; ferrite) phase transformation in pure iron. In order to describe the transformation between phases of different crystal structures, a multi-lattice approach can be taken as follows. Two interpenetrating lattices for the two phases are set up and are partially filled up such that the resulting (rectangular) bicrystal consists of several layers of bcc atoms and the remainder of fcc atoms (see Fig. 5.1). The lattices are oriented with the fcc (111) plane parallel to the bcc (110) plane and the fcc[11 $\bar{2}$] direction parallel to the bcc [00 $\bar{1}$] direction. The area densities of the closest-packed planes in both crystal structures are made identical and the volume misfit due to transformation is compensated by shifting the two lattices relative to one another (in a direction perpendicular to the original interface) after a fixed number of simulation steps. The simulation starts with one partially transformed plane as two-dimensional nucleus and subsequently the transformation proceeds in a plane-by-plane fashion.

Early simulations used a simple bond-counting model as interaction potential and a fixed activation energy for all jumps [66]. Later simulations used the embedded atom method (EAM) [67] and confirmed the earlier conclusions, thus demonstrating that even very simple interaction models can lead to and explain complex behaviour. It is too computationally demanding to calculate the activation energy for each jump using the EAM potential. Therefore, an artificial neural network can be employed. The activation energy for each of several thousands of jumps was determined by minimising the energy of neighbouring atoms, during a forced jump of one atom, using the conjugate gradient method [70]. The neural network was then trained with such data to calculate the activation energy of a jump on the basis of the positions of only 14 nearest neighbouring atoms. Details of the algorithm can be found in [66,67].

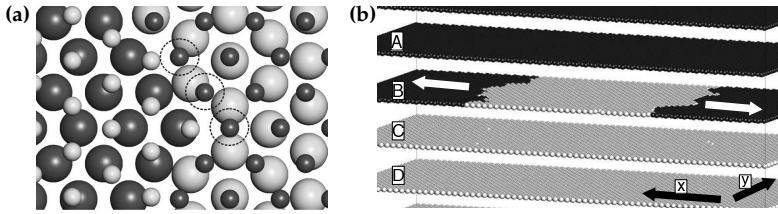


Figure 5.1: (a) A small portion of the interface between γ (fcc, light grey) and α (bcc, dark grey) on one densely-packed layer. The small spheres indicate unoccupied lattice positions and the large spheres indicate occupied lattice positions [69]. (b) A larger portion of the simulated bicrystal showing layers which are entirely filled with bcc/fcc atoms as well as one layer with a two-dimensional bcc nucleus embedded in fcc atoms. Here, the fcc atoms are shown in dark grey and the bcc atoms in light grey. The space between the layers has been made disproportionately large in order to provide a clearer view [68].

5.3.2 The activation energy for growth

From simulations as described above, values for the interface velocity as a function of time can be obtained. By fitting equation (5.5) to the simulated values, a value for the activation energy of γ/α -interface movement in iron of $Q_G = 0.99$ eV is obtained [68] (see Fig. 5.2). When comparing the thus-determined value for Q_G with a histogram of activation energies for *individual* jumps (see Fig. 5.3), it follows that only very few atomic jumps have such a high (or even higher) activation energy. One possible explanation for this observation would be to assume that the few jumps with high activation energies constitute the rate-limiting steps for interface movement. In order to test this hypothesis, simulations were performed in which all jumps with activation energies between 0.91 and 1.12 eV were prohibited. Again, the resulting activation energy for interface movement is approximately 1.00 eV, thus even lying in the interval of forbidden jumps. Therefore, it must be concluded that only a series of jumps, involving several atoms, via unfavourable, intermediate positions, can lead to the observed effective activation energy. A schematic energy path for such a series of jumps is shown in Fig. 5.4. For the fcc \rightarrow bcc transformation to proceed, several jumps must take place at or near the fcc/bcc interface, which all increase

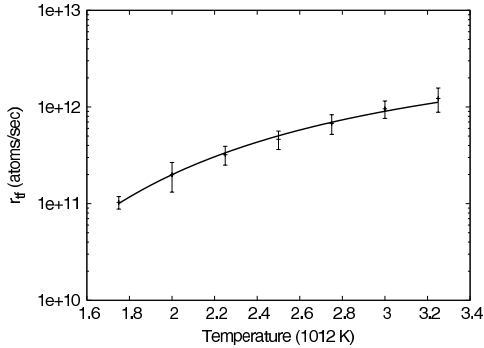


Figure 5.2: The transformation rate (which is proportional to the interface velocity, v) as a function of temperature as determined from simulations. The curve drawn through the simulated data points is a fit of equation (5.5). The resulting activation energy for interface migration equals $Q_G = 0.99$ eV [68].

the energy of the system (and which all have an *individual* activation energy < 0.99 eV) before a new bcc lattice position can be occupied by one atom and thereby the total energy of the system can be lowered.

5.3.3 Influence of the excess volume in the parent/product interface on interface migration

At a grain boundary, the density of a material is generally smaller than in the bulk of the material. The additional, unoccupied volume at the boundary is called excess volume. This excess volume is expected to have a strong influence on the interface velocity. It can be varied in simulations in two ways. Firstly, the orientation of the two parts of the bicrystal relative to one another can be varied. This can be accomplished by rotation of one crystal around an axis perpendicular to the interface between the two crystals and thereby atom arrangements at the interface are created with a varying amount of excess volume. Secondly, additional atoms can be inserted at the interface during the early stages of the simulation. This is possible since during interface migration, vacancies are formed at the interface by thermal fluctuations. By filling a predetermined number of such vacancies with additional atoms, the excess volume can be reduced.

Simulations in which the amount of excess volume at the interface was

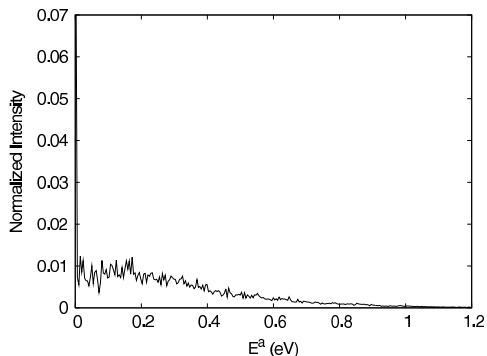


Figure 5.3: A histogram of the activation energy of the successful (single) atomic jumps during a kMC simulation using an EAM potential. Note that only few jumps have an activation energy larger than the overall activation energy for interface migration, $Q_G = 0.99$ eV (further see text) [68].

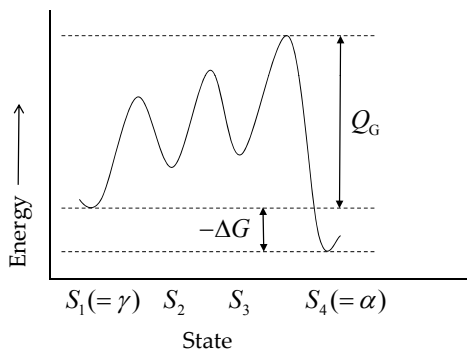


Figure 5.4: Schematic illustration of the path which the system could take from the initial state (fcc, S_1) over several unfavourable states (S_2 and S_3) to the stable state (bcc, S_4). The overall activation energy of the process is Q_G , which is larger than the activation energies of the single atomic jumps to intermediate states. The (negative of the) difference in Gibbs energy of final and initial states, ΔG , has been marked.

varied by these methods show that an increase in available excess volume leads, as expected, to a decrease of the interface-migration activation energy. However, not only the *amount* of excess volume has an influence on this activation energy, but in particular its *distribution* along the interface. If an atomic arrangement, such as the one in Fig. 5.5d, leads to regions in the parent/product interface where groups of atoms form (nearly) coherent arrangements, this will impede interface motion even if the amount of excess volume is considerable.

The activation energy for grain-boundary self diffusion can also be determined from simulations on the basis of the description above. Varying the excess volume in the parent/product interface has a strong and complex effect on the activation energy of grain-boundary self diffusion. The corresponding results can be rationalised, recognising that the activation energy consists of two parts: the activation energy for vacancy formation and the activation energy for vacancy migration. Depending on the atomic structure of the interface, especially the activation energy for vacancy formation varies strongly. It can be concluded that

- the activation energy for grain-boundary self diffusion is always larger than the activation energy for interface migration¹¹ (cf. the discussion at the end of section 5.2), and
- the exact atomic structure of the interface sensitively influences the dynamics of phase transformations. Each published study should describe exactly how the interface was set up, in order to allow comparisons of different studies.

5.4 Mesoscopic microstructure simulations

5.4.1 Simulation algorithm

Phase transformations control the eventual microstructure and thus the properties of many materials. Therefore, it is desirable to be able to predict the microstructure of a material subjected to a certain heat treatment. Even though classical kinetic models, such as the JMAK-model described in section 5.2, yield average microstructural information, like the average grain

¹¹This finding contrasts with experimental results (see references in [69]). The discrepancy is likely due to the absence of impurity atoms in the simulations, which can never be entirely avoided in experiments and which can have a strong influence on the interface-migration velocity.

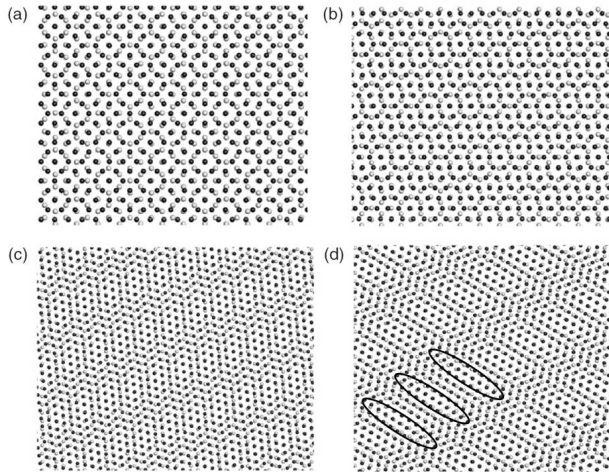


Figure 5.5: The atomic mismatch of γ/α -systems at their interface studied to identify the influence of excess volume at the interface on the transformation kinetics. Fcc atoms are shown in light grey and bcc atoms in dark grey. The arrangements were generated by rotating one lattice around an axis perpendicular to the interface. Specific patterns with nearly-coherent regions are visible. Some of such large nearly-coherent regions have been marked in panel (d) [69].

size¹², they cannot, for example, predict the grain-size distribution. Yet, the parameters of these models incorporate the data which prescribe number, shape and growth rate of growing grains and thereby allow simulations of the microstructural evolution.

There are several algorithms available for simulations of development of the microstructure. They can be grouped into algorithms which prescribe growth on the level of individual pixels/voxels in discretised space (“per-pixel/voxel-growth” or “local rules”) and algorithms prescribing the growth on the level of individual grains (“per-grain-growth” or “global growth rules”)¹³. Cellular Automata simulations and Potts Monte-Carlo

¹²The average grain size can be calculated by $\langle V \rangle = N_V^{-1} = [\int \dot{N}_V(t)(1 - f(t))dt]^{-1}$, if random nucleation prevails.

¹³Nucleation of phase transformations occurs at a length scale much smaller than the length

simulations (see, e.g. Ref. [17] for a review) belong to the first group. So-called “Geometric models” or “Avrami simulations” belong to the second group and have a number of advantages over per-pixel/voxel-growth simulations: they are less computationally intensive, there is no influence of the choice of discretised lattice, no propagating errors due to rounding-off problems and they offer a direct connection with the underlying kinetic model. It should be noted, however, that this type of algorithm cannot deal with local variations in the parent microstructure, e.g. in association with a position-dependent driving force. It is the objective of the work presented in this section to investigate the microstructure resulting from phase transformations which obey the specific class of kinetic models presented in section 5.2. Geometric algorithms are best suited for this task.

Geometric simulations have been in use for several decades (see, e.g. Refs. [12, 14, 27]). In essence, they adopt the nucleation rate and the grain radius in extended space from the kinetic model and apply them to a simulation grid. At each time step, the number of nuclei which should emerge is looked up. The location for these nuclei can be chosen either at random or be selected from a given list of allowed nucleus positions (see section 5.4.3). If the voxels at the thus-determined locations are not yet transformed, nucleation is performed by transforming these voxels. Next, for each grain, the radius in extended space is calculated from their nucleation time, the current time and the growth rate (cf. equation (5.5) in section 5.2). All voxels within a sphere of this radius around the nucleus position are transformed, if they are still untransformed (i.e. if the grain does not impinge on another, existing grain). The details of the program used in the work presented here have been described elsewhere [35].

5.4.2 Prediction of grain-size distributions

The influence of the type of nucleation and various model parameters (e.g. activation energies; see what follows) on the final microstructure after transformation, as exhibited in particular by the resulting grain-size distribution (GSD) is considered here [35]. For the present simulations, growth of randomly nucleated, isotropically growing grains (of (initially, i.e. before the onset of impingement) spherical shape) into a supersaturated matrix is assumed, implying that equation (5.1) holds for impingement. Interface-controlled growth at high supersaturation is assumed so that equation (5.5)

discretisation in a mesoscopic simulation. Therefore, in both classes of algorithms, nuclei are introduced into the simulation by “switching” a certain number of single voxels, as provided by a nucleation model, e.g. the one given in equation (5.4), to the transformed state.

can be approximated by

$$v(T) = v_0 \exp\left(-\frac{Q_G}{RT}\right). \quad (5.6)$$

As nucleation models, “pre-existing nuclei” as well as “continuous nucleation” (according to equation (5.4)) are treated.

Examples of resulting microstructures can be seen in Fig. 5.6. Corresponding grain-size distributions are shown in Fig. 5.7. All GSDs are presented as histograms of the diameter of an equivalent sphere (i.e. a sphere of volume equal to the volume of the (non-spherical) grain in the simulated microstructure), D_V , normalized by the equivalent diameter of a grain of average volume, $D_V/D_{\langle V \rangle}$.

If pre-existing nuclei are assumed, the resulting GSD is very narrow and independent of all kinetic parameters¹⁴. Specifically, the growth rate (and thus the temperature prevailing during the transformation) does not influence the GSD.

Adopting continuous nucleation, the only input parameter which changes the GSD is the ratio of the activation energies for growth and nucleation, Q_G/Q_N . Note that also the heating/cooling rate applied does not influence the observed GSDs. The GSDs obtained upon heating and cooling for various values of the ratio of the activation energies, Q_G/Q_N , are shown in Figs. 5.7 and 5.8, respectively. For comparison, also the GSD resulting from pre-existing nuclei is shown. It follows that varying the ratio of activation energies has strikingly different effects on the GSDs obtained upon heating and upon cooling.

For transformations upon heating, the simulations start at a temperature of 0 K. This means that, during the simulation, the process with the lower activation energy will start first. If this is nucleation ($Q_G/Q_N > 1$), many nuclei are formed before the onset of growth. This situation is similar to a transformation with pre-existing nuclei and thus the resulting GSD is also very narrow. If growth has the lower activation energy ($Q_G/Q_N < 1$), no transformation can occur until the first nuclei appear; once they do appear, they can grow rapidly, leading to a microstructure with very large grains taking up a large part of the microstructure and small grains distributed between these large grains (cf. Figs. 5.7 and 5.6c).

For transformations upon cooling, both nucleation and growth processes take place already at the very beginning of the transformation. The process

¹⁴This is true for the *normalised* GSDs presented here. The *average* (not normalised) grain size can be calculated by $\langle V \rangle = N_V^{-1}$ for pre-existing nuclei and is influenced by both N_V and v for other nucleation models; see footnote 12.

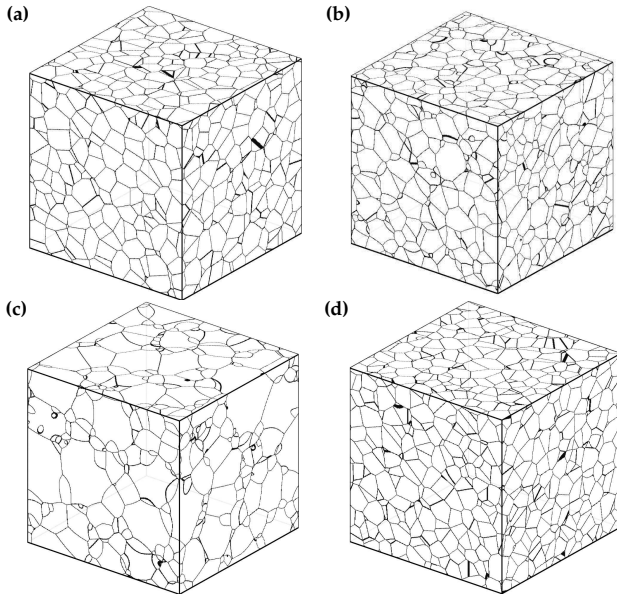


Figure 5.6: Example microstructures resulting from geometric, mesoscopic simulations, assuming pre-existing nuclei (a) (this result does not depend on the (time dependence of the) temperature), continuous nucleation and isothermal transformation (b), continuous nucleation during heating with constant heating rate and an activation energy ratio $Q_G/Q_N = 0.01$ (c) and $Q_G/Q_N = 100$ (d). See also the corresponding GSDs in Fig. 5.7 [35].

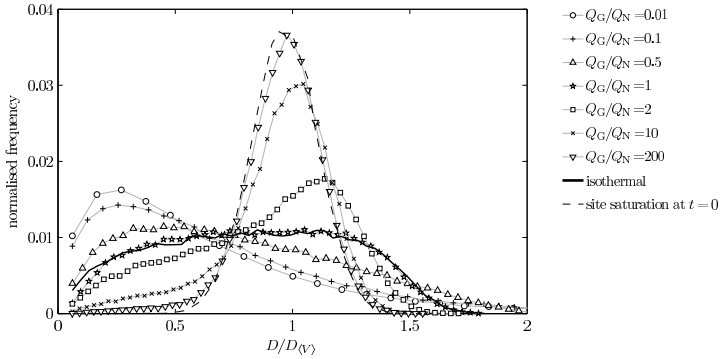


Figure 5.7: The GSDs resulting from geometric, mesoscopic simulations assuming continuous nucleation and a constant *heating* rate for various values of the ratio of the activation energies for growth and nucleation, Q_G/Q_N . For comparison, the GSDs for an isothermal transformation and continuous nucleation, as well as for a simulation assuming pre-existing nuclei (result independent of the (time dependence of the) temperature), are shown [35].

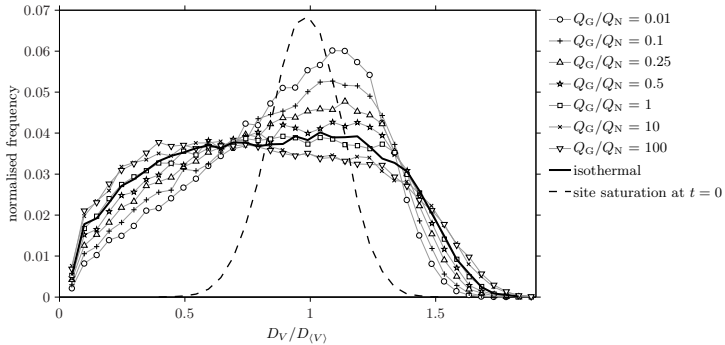


Figure 5.8: Analogous to Fig. 5.7, but for transformations at constant *cooling* rate [35].

with the larger activation energy (either nucleation or growth) ceases first. If this is growth ($Q_G/Q_N > 1$), then the transformation cannot proceed to completion. Therefore, in the simulations, the absolute values of the activation energies have been adjusted (lowered) such that the transformation can complete for each ratio of activation energies. After this adjustment, the GSDs can be compared (see Fig. 5.8). It can be seen that the range of possible grain-size distribution shapes is smaller than in the case of transformations upon heating. Further, the visible trend in shape of the GSD is just the opposite of the one observed for the case of heating (cf. Figs. 5.7 and 5.8): The larger the ratio Q_G/Q_N is for the transformation upon cooling, the more the maximum of the GSD is shifted towards small grain sizes.

It is worth noting that for both heating and cooling, the GSDs with $Q_G/Q_N = 1$ coincide with the GSD resulting from an isothermal transformation: Equal activation energies mean that the temperature dependencies of nucleation and growth are identical and thus their relative speeds stay constant, regardless of the temperature program.

It can be concluded that knowledge about the temperature dependencies of the nucleation and growth rates during a phase transformation allows to predict and understand the grain-size distribution resulting from the transformation.

5.4.3 Effects of non-random nucleation

Simulations are not only useful to gather data on the microstructure if the underlying kinetics is known, but also to simulate the phase transformation kinetics for circumstances under which JMAK(-like) models (cf. Footnote 10 in section 5.2) are not valid. This is for example the case if nucleation does not occur randomly in the bulk volume of the parent phase (homogeneous nucleation), but rather at specific sites, such as parent-phase grain boundaries (heterogeneous nucleation). Nucleation on parent-phase grain boundaries is a quite common phenomenon which is observed for example in precipitation reactions or massive transformations.

To account for non-random nucleation, a first approach involves modification of the impingement correction with an empirical impingement parameter (see equation (5.2)). This additional fit parameter often allows to fit experimental data in cases where the transformation kinetics does not comply with the impingement correction equation (5.1).

A less empirical approach was given by Cahn [11]. In his model, parent-grain boundaries are approximated as randomly distributed planes and nucleation is only allowed on these planes. One additional parameter, namely

the parent-phase grain-boundary area per unit volume, S_V^{GB} , is then needed to describe the phase transformation kinetics. Planar grain boundaries are unrealistic, because they are generally incompatible with (mechanical) equilibrium at grain grain-boundary junctions/edges. The question then arises whether approximating grain boundaries as planes will nevertheless lead to a model which is able to correctly describe experimentally obtained kinetics of grain-boundary nucleated phase transformations.

Another approach may be based on the so-called time cone formalism [42] which has been shown to be applicable to phase transformations with certain non-random nucleus arrangements [43]. However, the application of the method to grain-boundary nucleation so far has been limited to simple geometric parent-grain shapes and extending it to more realistic parent-grain morphologies appears to be non-trivial.

As compared to the above, theoretical, possibilities to treat non-random nucleation, simulations offer high flexibility to change the nucleus arrangement, almost arbitrarily, once the program has been set up. A two step process can be adopted [61,71]. First, a geometric simulation is performed with randomly distributed nuclei in order to generate a microstructure with a known GSD. In a second, subsequent simulation, nucleation is only allowed to occur on the grain boundaries of this parent microstructure. Several parameters can then be varied and the resulting kinetics compared with the one for nuclei randomly distributed in the bulk. The effects observed [61,71] can be summarised as follows:

- *The ratio of the parent-grain boundary density and the number of product nuclei/grains, S_V^{GB} / N_V .* The higher this ratio is, the closer the simulated kinetics follows the course of the transformation pertaining to random nucleation in the bulk (and the faster the transformation reaches completion, see Fig. 5.10). Conversely, the lower the ratio is, the sooner the simulated kinetics deviates from the case of random nucleation (and the longer it takes for the transformation to reach completion).
- *The nucleation mode in the parent \rightarrow product transformation.* The more nuclei are formed early in the transformation, the stronger the deviation of the kinetics from the case of random nucleation is. The strongest such deviation occurs for the case of pre-existing nuclei.
- *The parent grain-size distribution.* If this distribution has many small, but also very large grains, then the resulting kinetics will differ particularly strongly from the case of random nucleation in the bulk. For any other, less wide GSD, the deviation will be less pronounced.

All these observations can be understood when taking into account the positions of nuclei relative to one another (i.e. their position correlation). If nuclei are formed very close to one another, then impingement will set in relatively early in the transformation, i.e. earlier than in the case of randomly distributed nuclei. This position correlation occurs if a large number of nuclei are located on few parent-grain boundaries (the case of a small ratio S_V^{GB}/N_V) or if the parent microstructure features many large grains, i.e. relatively large regions in which no nucleation can take place. Also, since nuclei cannot form in already-transformed areas, an ongoing nucleation during transformation diminishes the effect of correlated nucleus positions as compared to pre-existing nucleation. This last statement does not only pertain to grain-boundary nucleated phase transformations.

The type of simulations considered here can indicate which kinetic model (i.e. which one of the above described approaches) is best able to describe the (simulated) transformation kinetics associated with grain-boundary nucleation. The results of fitting these kinetic models to simulated kinetics are shown in Fig. 5.9. It is clear that an (unmodified) JMAK model, compatible with random nucleation (cf. equation (5.1); case A in Fig. 5.9) cannot at all describe the observed kinetics. The same holds for a MKM model using impingement with the parameter ε (cf. equation (5.2b); case C). All other considered models are able to well describe the simulated transformed fraction. If, however, the values of the kinetic parameters as determined from these fits are compared with the values that were used as input values for the parameters of the simulation, it is found that Cahn's model (case B) yields incorrect fit results. Further analysis (see [71] and Fig. 5.10) reveals that only if Cahn's model is modified (extended) with an empirical impingement parameter, ζ , analogous to equation (5.2b), (case F), correct values for the kinetic parameters are obtained for all values of S_V^{GB}/N_V (see Fig. 5.10a).

As long as the deviation from random nucleation in the bulk is small (large values of S_V^{GB}/N_V), also a MKM model with the impingement parameter ζ (case D) yields good results (see Fig. 5.10b).

It can therefore be recommended to use the here proposed modified Cahn model modified with the impingement parameter ζ when describing experimentally determined kinetics of grain-boundary nucleated phase transformations. However, the gain in the quality of the fit obtained by using the Cahn model with the impingement parameter ζ as compared to the MKM model with the same impingement parameter is obtained at the cost of introducing an additional parameter: the parent grain-boundary density S_V^{GB} , the value of which can be determined (preferably) by measurements, before the transformation, or by adopting it as an additional fit parameter in the

data analysis.

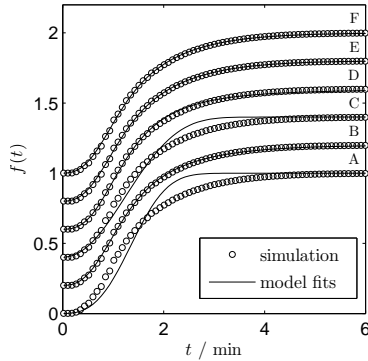


Figure 5.9: The simulated transformed fraction for a grain-boundary nucleated phase transformation (symbols) together with model fits for various kinetic models (lines). The results for the individual cases have been shifted vertically with respect to each other to improve legibility. A: JMAK model, B: Cahn's model, C: MKM model using the impingement parameter ε , D: MKM model using the impingement parameter ζ , E: modified Cahn model using the impingement parameter ε , and F: modified Cahn model using the impingement parameter ζ [71].

5.5 Conclusions

- In the analysis of phase-transformation kinetics, computer simulations can provide an atomistic interpretation of the mesoscopic kinetic parameters.
- Atomistic simulations expose the atom movements at a migrating interface which are not (yet) retrievable experimentally in a statistically assured manner. Thereby, the atomic configuration of an interface and in particular the excess volume at the interface are shown to play an important role in determining the phase-transformation kinetics.
- Mesoscopic simulations can be used to determine the (evolution of the) microstructure resulting from a specified transformation kinetics.

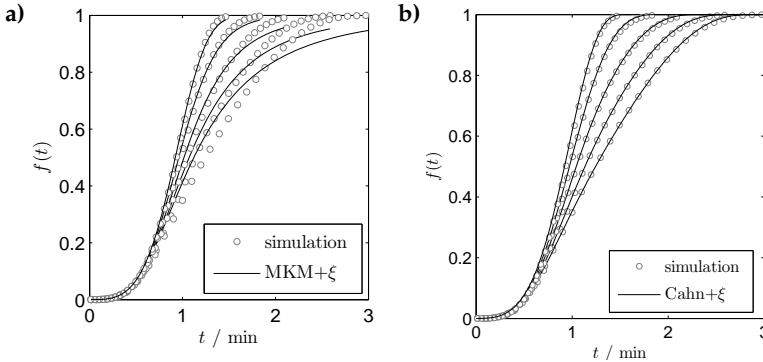


Figure 5.10: Simulation results (symbols) for a series of simulations for various parent grain-boundary densities, S_V^{GB} , together with model fits (lines) of the MKM model (a) and the modified Cahn model (b), both using the impingement parameter ζ (equation (5.2b)). The comparison shows that the modified Cahn model is suitable to describe the simulated phase transformation kinetics in all cases, while the MKM model can only be utilised for modest deviations from random nucleation [71].

Therefore, a powerful tool to validate a kinetic model is provided by comparing the predicted, simulated microstructure (e.g. as exhibited by a grain-size distribution) with the experimental observation.

- Simulations allow a full determination of phase transformation kinetics, at circumstances for which no analytic expressions for the transformation kinetics are available. With this information, empirical models can be validated and calibrated.

Chapter 6

The kinetics of and the microstructure induced by the recrystallisation of copper

6.1 Introduction

Recrystallisation of deformed materials is a process of high technological importance and has therefore been studied intensively for many decades [60,72,73]. Even though the kinetics of the recrystallisation process is easily accessible through hardness measurements, metallographic or calorimetric measurements, its interpretation is a matter of on-going debate [60].

Simple models, e.g. based on the assumption that all nuclei¹⁵ are present at the beginning of the process and that the velocity of the interfaces between deformed and recrystallised material is constant (at constant temperature), were unable to correctly describe both the observed kinetics and the microstructure after recrystallisation. Kinetic models have been proposed which are able to describe the experimentally determined recrystallisation kinetics, e.g. by assuming that there exists a distribution of growth rates during recrystallisation [37]. However the assumptions made in such models need to be validated. One way to validate kinetic models is to compare the accordingly predicted microstructure, i.e. the grain morphology and/or the grain-size distribution and/or the texture after completed recrystallisation, with the experimentally determined microstructure. The microstructure which follows the adoption of a certain kinetic model can be determined by carrying out a mesoscopic simulation.

Conversely, also models have been proposed which are able to describe experimentally observed microstructural parameters as the grain-area distribution, e.g. by assuming that the nucleation rate accelerates during recrystallisation [76]. They can be validated by comparing the recrystallisation kinetics as predicted by mesoscopic simulations on the basis of these

¹⁵It must be recognised that nucleation in recrystallisation is not the outcome of a fluctuation phenomenon as in heterogeneous phase transformations. Instead, the "nuclei" are already present in the deformed material (as subgrains [60]) and can become "activated" subject to instability criteria [60,74,75]. Nevertheless, the moment a (sub-) grain starts to grow is denoted "nucleation".

models with experiments.

Recent recrystallisation models use data on the microstructure of the material in the deformed state to calculate the nucleation rate (see, e.g. [77]) or the growth rate of recrystallising grains (see, e.g. [78–80]). To this end, informations about e.g. the subgrain-size distribution, the stored energy distribution, the texture or the misorientation-angle distribution are required as input values. Against this background, the deformed microstructure must be characterised in detail. This is done in this study by electron backscatter diffraction (EBSD) measurements of deformed, unrecrystallised specimens.

To the authors' knowledge, there are only a few studies available in the literature which present combined experimental data sets, i.e. both kinetics and microstructural change for the same recrystallising material. In this study, differential scanning calorimetry (DSC) and EBSD measurements of the static¹⁶ recrystallisation of pure copper have been conducted. The importance of taking into account informations about both the kinetics of recrystallisation and the microstructural development during recrystallisation has been illustrated in this work by mesoscopic simulations.

This paper is organised as follows. First, a concise overview of previously published work on the recrystallisation of pure copper is presented in section 6.2. Subsequently, the specimen preparation, the experimental methods and the employed simulation method are described in section 6.3. The calorimetry and microscopy results are presented in section 6.4. The kinetics and microstructure results are discussed, compared with each other and with the results of mesoscopic simulations in section 6.5.

6.2 Literature survey

6.2.1 Kinetics

Data on the kinetics of recrystallisation can be obtained with a variety of experimental methods. A summary of literature results for the recrystallisation kinetics of pure copper has been given in Table 6.1, including indication of the experimental method used for the kinetic analysis.

For isothermal measurements, the overall, effective activation energy, Q_{eff} , can be determined from a plot of $\ln(\Delta t)$ versus T_{iso}^{-1} , where $\ln(t_{f''} - t_{f'}) = \ln(\Delta t)$ is the logarithm of the time elapsed between two certain fixed fractions recrystallised, f' and f'' , and T_{iso}^{-1} is the inverse of the measurement

¹⁶I.e. recrystallisation which occurs during annealing after deformation, and not (dynamically) during deformation.

temperature. In this work, the time elapsed from the beginning of the measurements is employed (i.e. the first test fraction recrystallised is chosen to be $f' = 0$). For isochronal measurements, the overall, effective activation energy can be determined by applying a Kissinger-like analysis, i.e. a plot of $\ln(T_{f'}^2/\Phi)$ versus $T_{f'}^{-1}$, where $T_{f'}$ is the temperature at which a certain fixed value of the transformed fraction, f' , is reached and Φ is the heating rate [1, 8].

Evidently, the reported values for the effective activation energy vary widely (see table 6.1). The largest reported activation energy is approximately three times higher than the smallest one. If, on the one hand, all recrystallisation nuclei are present at $t = 0$, the activation energy determined represents an activation energy of growth. If, on the other hand, nucleation occurs (also) during the recrystallisation, then the reported activation energy is an effective one and the determination of its separate components, the activation energy for nucleation and the activation energy of growth, may be cumbersome (see section 9.6.12 in Ref. [1]). To the authors' knowledge, no such analysis has been performed for the recrystallisation of copper until now. Interpretations of the values obtained for Q_{eff} have been attempted in terms of the nucleation mechanism, a distribution of activation energies or impurity content (see references in table 6.1).

For isothermal measurements, the recrystallised fraction, f , is often presented as a "double-logarithmic plot" of $\ln(-\ln(1-f))$ vs. $\ln(t)$, also called "JMAK plot". The last designation is motivated by the occurrence of straight lines in such plots if the kinetics can be described by the classical JMAK kinetic model [1, 8], i.e. if the kinetics obey an equation of the type

$$f(t) = 1 - \exp(-kt^n), \quad (6.1)$$

where k is a rate constant and n is the growth exponent, also called Avrami-exponent, i.e. the slope of the straight line possibly observed in the double-logarithmic plot¹⁷. A deviation from straight-line behaviour in the plot discussed, which is often observed (see Table 6.1), means that the kinetics cannot be described by the classical JMAK model. Equation (6.1) only holds under specific circumstances [1, 8], such as spatially randomly distributed nuclei, specific nucleation modes (pre-existing nuclei or continuous nucleation) and isotropic growth (see also section 10.2.2 in Ref. [1] for a listing

¹⁷The growth exponent n can also be determined from isochronally (i.e. with constant heating rate) conducted experiments. To this end, an appropriately adapted variant of the JMAK equation has to be applied and then n is the negative of the slope of the straight line possibly observed in a plot of $\ln(-\ln(1-f))$ versus $\ln \Phi$ (with Φ as the heating rate). See section 9.6.15.5 in Ref. [1].

of the assumptions made in this approach). Thus, nonlinear behaviour in double-logarithmic plots can have widely varying causes (see below).

The experimentally observed slopes in the double-logarithmic plots range from below unity to more than four (see table 6.1). Within the framework of the JMAK model, the value of the slope, n , allows to draw conclusions concerning the nucleation and growth mechanisms. Assuming that the recrystallised grains grow isotropically and with a constant rate at constant temperature (i.e. "linear growth", usually compatible with interface-controlled growth, occurs), the nucleation mode can be deduced from the slope: A value of three indicates that all nuclei are present at the beginning of the transformation ("pre-existing nuclei", i.e. "site saturation at $t = 0$ ") while a value of four indicates a constant nucleation rate ("continuous nucleation") [8]; for a recent example of this type of deduction, see Ref. [81]. Exponents smaller than three are incompatible with "linear growth", i.e. a constant growth rate at constant temperature. Only a combination of pre-existing nuclei and a decreasing growth rate at constant temperature leads to such low values of n . Indeed, decreasing growth rates have been observed experimentally [82–84].

At late stages of recrystallisation, the recrystallisation rate drops, causing the slope in the double-logarithmic plot to decrease. This behaviour cannot be explained by a growth rate which is *continuously* decreasing exponentially with time [60], since this would lower the slope in double-logarithmic plots for the whole recrystallisation, and not only for late stages. It was found experimentally that not all recrystallising grains exhibit the same growth rate. There exists a distribution of growth rates in a specimen [84] and grains with a specific crystallographic orientation with respect to the specimen frame of reference were observed to grow faster than other grains [83]. A distribution of growth rates can explain the observed drop in the slope, n , of double-logarithmic plots at late stages [37]. Also other explanations for the observed decrease of n must be considered, e.g. non-random nucleation or anisotropic growth of recrystallised grains (see section 6.5).

For isothermal measurements, if the growth rate of recrystallising grains is assumed to be constant or to decrease with time, a slope in the double-logarithmic plot larger than four (see table 6.1) can only be explained with accelerating nucleation during recrystallisation. It has been observed that new grains nucleate "autocatalytically" at the interface between deformed and recrystallised material [85–87], which leads to a nucleation rate which increases with time in the initial stage of recrystallisation.

From the above discussion on the large spread in the observed recrystallisation kinetics of copper, it can be concluded that the prevailing time-

dependences of the nucleation and growth rates in the recrystallisation appear to *strongly* depend on the specimen preparation (the mode of deformation), possibly also on specimen purity and the temperature program (isothermal or isochronal).

Finally, it is remarked here that a comparison of various different experimental techniques, including calorimetric ones, to investigate recrystallisation kinetics has shown very good agreement of the results obtained for the recrystallisation kinetics by application of these methods [88]. It can therefore be excluded that a substantial amount of recovery takes place during recrystallisation, since recovery would affect the heat signal, and thus the apparent recrystallised fraction, as measured by calorimetry, but not the recrystallised fraction as measured by direct characterisation of the microstructure.

6.2.2 Microstructure

The grain-area distribution (GAD) as measured in a cross-section of fcc metals after completed recrystallisation is usually said to be of log-normal type [60]. To the authors' knowledge, no grain-area distributions of recrystallised pure copper are available in the literature. It has been remarked that the grain-area distribution is very broad: the largest observed linear intercept lengths between grain boundaries in the cross sections of specimens were approximately four times larger than the mean intercept length [83]. More information is available for aluminium alloys, where log-normal distributions were indeed commonly found [56,76]. The GADs obtained from *simulations* of recrystallisation of fcc metals are usually much narrower than these *experimentally observed* GADs (see e.g. Refs. [79,99]).

The driving force for grain-boundary migration in recrystallisation is ascribed to the difference in stored energy in front of and behind the moving boundary. However, also reduction of grain-boundary area (i.e. coarsening/normal grain growth) is a driving force for boundary migration and thus, overlap of the recrystallisation and grain-coarsening processes can in principle influence the GAD. Monte Carlo simulations in which both driving forces were taken into account lead to a kink in the double-logarithmic plots of the simulated (isothermal) recrystallisation kinetics which was attributed to coarsening during recrystallisation and which kink vanished if the grain-boundary energy, and thereby the driving force for coarsening, was decreased [100]. Since the driving force for recrystallisation in strongly-deformed metals is several orders of magnitude larger than the driving force for coarsening [60], grain growth during recrystallisation only plays a mar-

Table 6.1: Overview of literature results concerning the kinetics of static recrystallisation in pure copper. “-” indicates that this information could not be found in the paper cited. OM: optical microscopy, DSC, differential scanning calorimetry, EBSD: electron backscatter diffraction, ECAP: equal channel angular pressing. The deformation is quantified in terms of rolling reduction, ϕ , true strain, ϵ , or shear, γ .

Reference	Method	Purity	Deformation Mode	growth exponent, n	Q_{eff} / kJ
[89]	isothermal, neutron diffraction	3N	cold rolling, $\phi = 95\%$	≈ 1	125–170
[90]	isothermal, OM	4N	hot compression, $\phi = 22\%$	0.8 ^a	-
[91]	isothermal, OM	4N	wire drawing, $\epsilon = 0.4\text{--}2.8$	1.0	-
[92]	isothermal, tracer diffusion	3N	ECAP	1.14	160
[93]	isothermal, EBSD	4N	ECAP	1.3–1.5	-
[94]	isothermal, OM	4N	cold rolling, $\phi = 93\%$	1.7; 2.7 ^b	-
[95]	isothermal	-	hot rolling, $\phi = 5\text{--}33\%$	2.2	-
[88]	isothermal, various	3N	cold rolling, $\phi = 92\%$	3.1 (dropping) ^c	-
[87]	isothermal, DSC	3N	cold rolling, -	4.0 (dropping) ^c	-
[96]	isochronal DSC	5N	cold rolling, $\phi = 70\%$	-	58
[37]	isochronal DSC	3N	cold rolling, $\phi = 92\%$	3.0	85
[97]	isothermal, DSC	4N	cold rolling, $\phi = 80\%$	4.6 ^d	-
	isochronal DSC	4N	cold rolling, $\phi = 25\text{--}97\%$	-	75–130 ^e
	isochronal DSC	4N	torsion, $\gamma = 0.5\text{--}7.1$	-	95–130 ^e
this study	isothermal, DSC and EBSD	5N	cold rolling, $\phi = 95\%$	3.0 (dropping) ^c	113–109 ^f

^aobserved a higher, temperature-dependent Avrami-exponent in early stages

^bdependent on grain size; coarse grains: 1.7, fine grains: 2.7

^c“dropping” means that the observed kinetics deviate from a straight-line behaviour in the double-logarithmic plot towards the end of the recrystallisation

^ddetermined by Starink et al. [98], only the first 10% of the recrystallisation was analysed

^edecreases with increasing deformation

^fdepends on the transformed fraction; see section 6.4.1

ginal role, if at all, in the recrystallisation of such materials (see also section 6.4.2).

6.3 Experimental details and simulation method

6.3.1 Specimen preparation

High-purity copper was supplied by Alfa Aesar (Karlsruhe, Germany) as a rod with a purity of 99.999 at.-% (metals basis). From this rod, cylinders of 10 mm height were cut and rolled in a laboratory rolling mill with the rolling direction perpendicular to the cylinder axis to a sheet of thickness 0.5 mm with a reduction in thickness of 0.5 mm per pass (leading to a rolling reduction of 95%). The “cylinder” was rotated around the cylinder axis (i.e. around an axis perpendicular to the resulting sheet surface) between successive passes to yield a homogeneous deformation and approximately equiaxed grains. Between passes, the material was cooled in ice water to prevent dynamic recrystallisation. Disc-shaped specimens with a diameter of 4.5 mm were punched out of the rolled sheet and the resulting specimens were lightly ground in order to produce a flat surface. The deformed specimens were stored at 193 K (-80°C) to avoid room-temperature recovery and recrystallisation.

Before each measurement, the specimens were annealed (in a DSC apparatus; cf. section 6.3.2) at 383 K (110°C) for 10 min. Both DSC and EBSD measurements showed that no recrystallisation takes place during this pre-treatment. Since recovery is a process with an exponentially declining rate at constant temperature [60], the pre-treatment ensures that the main portion of the stored energy of the specimen which can be released by recovery has already been released before any further, recrystallisation experiments are conducted. Moreover, it has been shown that prior annealing treatments have no strong influence on the kinetics of the subsequent recrystallisation kinetics (see discussion and references in [100]).

For EBSD measurements (cf. section 6.3.3), employed to characterise states of partial and complete recrystallisation, specimens were annealed in an oil bath at 413 K (140°C) for various times between 6 and 22 min and subsequently quenched in ice water. The partially recrystallised specimens were stored at 193 K (-80°C) until further examination.

6.3.2 Calorimetry

Enthalpy changes upon recrystallisation were recorded using a PerkinElmer Pyris 1 power-compensated DSC. The temperature measurement was calibrated using literature values for the melting temperature of pure zinc, lead and indium and the heat-flux signal was calibrated using the melting enthalpies of lead and indium. The specimens were encapsulated in aluminium pans prior to the measurements. All experiments were performed isothermally, where the specimens were heated to the desired temperature with the highest possible heating rate of the device (approximately 200 K/min). After completion of the observed heat effect, the specimens were cooled down to room temperature.

Since there is only very little heat released during recrystallisation and the device therefore operates close to its limit of resolution, special care was given to the determination of the base line. Usually, the base line for the measurement of an irreversible process is provided by a repetition of the measurement (second run), during which no heat flux from the specimen is observed. However, the first and second run of typical measurements (see figure 6.1 a) do not coincide at the beginning of the measurement, i.e. before the onset of the recrystallisation, as they should. Also the first and second runs of already-recrystallised, inert specimens (cf. figure 6.1 a) do not coincide, i.e. the second run is "flatter" and the recorded heat flux approaches zero sooner after reaching the measurement temperature than in the first run. Therefore, the difference between the first and the second runs must stem from e.g. a variable contact between the pan and the surface of the heating chamber in the DSC.

For a large number of measurements with inert specimens at various temperatures (see figure 6.1 a), it was found that the apparent heat effect as measured in the first run (= the base line for the DSC scan recorded for the deformed, recrystallising specimen) can be well described by

$$\frac{d\Delta H}{dt} = C_1 \exp\left(\frac{t}{C_2}\right) + C_3 t + C_4, \quad (6.2)$$

where $d\Delta H/dt$ represents the negative of the observed heat flux, t denotes the time elapsed since the measurement temperature has been reached, and the four C_i are constants. Fitting of the constants C_i simultaneously to all measurements of the first run of inert specimens, even for the same measurement temperature, was not well possible for a single set of C_i values. Therefore, base lines for the recrystallisation runs were constructed for each measurement individually by fitting equation (6.2) to the parts of the DSC

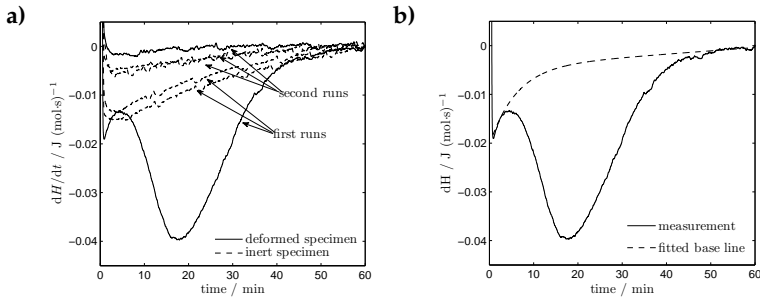


Figure 6.1: a) The heat flux signal of a DSC device for the first and second runs of a deformed and an inert copper specimen at 408 K (135°C). b) The heat flux of the first run of the same deformed specimen as in panel a) together with the fitted base line according to equation 6.2. All curves in panels a) and b) were shifted vertically to zero heat flux at the end of the measurements.

signal before and after recrystallisation (figure 6.1 b). Adopting this procedure, well-reproducible results for the recrystallised fraction as function of time, $f(t)$, were obtained.

Since recovery is a process with an exponentially-declining heat release, in principle it cannot be excluded that the adoption of an exponentially-declining function for the base line masks some heat release possibly due to concurrent recovery [101]. However, a comparison of the first measurement runs of a deformed and an inert specimen (cf. figure 6.1) shows that the amount of heat release by recovery, if there is any at all, must be small (see also the discussion at the end of section 6.2.1 and see section 6.3.1).

6.3.3 EBSD

Specimens for EBSD characterisation were prepared by removing the surface layer of the specimens by grinding and subsequent polishing. All EBSD scans were performed in the surface plane. The measurements were performed with a Zeiss Leo 438VP scanning electron microscope with an EDAX TSL EBSD measurement system. After each measurement, a “cleanup procedure” of the measured data file was employed in which grains smaller than four pixels are removed and the adjacent grains are enlarged accordingly until they impinge on each other.

Many twin boundaries, coherent and incoherent, were observed in the microstructure. It is not clear whether the observed twinned parts of copper crystals are induced as growth faults of growing recrystallised grains [102, 103] or whether they nucleate autocatalytically, at the migrating boundary between deformed and recrystallised material [85, 87, 93]. In each of both cases, they do not originate by separate nucleation events, but develop from an already-existing recrystallised grain. It is therefore reasonable to group all adjacent crystal parts in twin orientation into one grain, as was done in the present study.

The spread of grain-area size observed in fully recrystallised specimens is very large. Therefore it was impossible to correctly determine both the number of very large and very small grains simultaneously from a single EBSD measurement: If the step size of the EBSD scan is large, small grains consist of only very few pixels and then are deleted by the cleanup procedure. If the step size is small, the number of pixels necessary to capture a statistically significant number of large grains becomes prohibitively large. The cumulative grain-area distributions of the same specimen, as determined for various step sizes, are shown in figure 6.2. The grain areas observed in these measurements range from $10^0 \mu\text{m}^2$ to $10^5 \mu\text{m}^2$. It follows from figure 6.2 that the smallest employed step size is still not small enough to resolve the smallest grains in the microstructure. For measurements of entirely recrystallised specimens, a step size of $\Delta x = 1 \mu\text{m}$ was chosen. With this step size, the smallest grains cannot be resolved, however the overall shape of the grain-area distribution is correctly captured.

On the basis of the EBSD measurements, it is possible to distinguish the recrystallised parts from the unrecrystallised parts of a specimen which was quenched to room temperature after partial recrystallisation. To this end, the average so-called image-quality index¹⁸ of all pixels belonging to a grain can be used¹⁹ [104]. Partially recrystallised specimens exhibit a bimodal distribution of the average grain-image quality: see figure 6.3, which shows the corresponding histogram for a specimen which has recrystallised to 67%. Hence, a threshold value can be chosen in order to distinguish recrystallised grains (high grain-image quality) and unrecrystallised grains (low grain-image quality). There is some overlap between the two constituents (peaks) of the distribution (cf. figure 6.3) and therefore some grains will be classified

¹⁸The image quality is a measure of the quality of the backscatter electron diffraction pattern of the material corresponding to one pixel.

¹⁹It is also possible to use the average orientation spread in a grain to distinguish between recrystallised and unrecrystallised parts of the specimen. In the present study, both methods have been shown to lead to the same results.

incorrectly as recrystallised even though they are unrecrystallised grains, and vice versa. However, the overlap is not large, the vice-versa nature causes compensation and therefore the error thus made in the classification is small. The majority of the grains for which classification is ambiguous are small grains. Therefore, the GADs determined from EBSD scans are least reliable for small grain areas. Small differences in specimen preparation bring about different average values of the grain-image quality for different specimens, so that the threshold must be and was chosen separately for each specimen.

EBSD scans of partially recrystallised specimens provide quantitative values for various parameters characterising the (partially) recrystallised microstructure. Firstly, the grain-area distribution can be determined. For small fractions recrystallised, only few grains are recorded and therefore the corresponding grain-area distributions are not very reliable. Further, the area fraction recrystallised (which equals the volume fraction recrystallised, f) as well as the number of grains per unit area, N_A , can be determined. It should be noted that N_A , the number of grains per unit area in a two-dimensional cross section of a specimen, is not equal to the number of grains per unit volume of the specimen, N_V , which latter value can generally only be determined from three-dimensional measurements. N_V can only be determined straightforwardly from N_A if it is assumed that all grains are spherical [86,105], an assumption which does not hold for recrystallising copper (cf. the figures in section 6.4.2) and generally not in case of anisotropic recrystallisation-front velocities. Finally, the area of the interface between recrystallised and unrecrystallised material per unit volume, S_V , can be determined. It is calculated from $S_V = 2N_L$, where N_L is the number of times a straight line randomly drawn on the cross section traverses from an unrecrystallised to a recrystallised grain (and vice versa), divided by the length of the line [105]. Due to the discrete nature of the EBSD measurements, this method is sensitive to measurement artefacts (e.g. apparent one-pixel grains if the probe line “touches” a grain with a rough grain boundary at an acute angle).

6.3.4 Simulations

Kinetic models make assumptions about the nucleation and growth (and impingement) mechanisms. On the basis of such a (mesoscopic) kinetic model, simulation methods can be devised to determine the resulting microstructure. To this end, so-called geometric simulations are particularly efficacious [35]. In these simulations, grains are assumed to grow as spheres

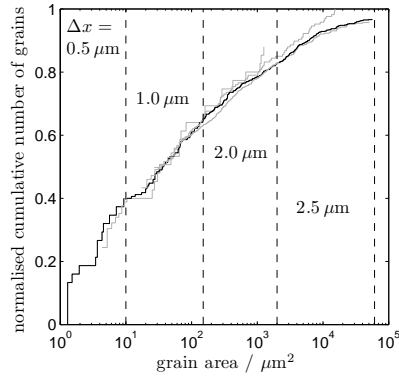


Figure 6.2: The cumulative logarithmic grain-area distribution (GAD) of a fully recrystallised (at 413 K (140°C)) specimen measured by EBSD scans with variable scan step size Δx (in μm , indicated in the figure). The individual measurements, each with a different step size, are shown in grey lines, for only those grain-area ranges that could practically be covered (see text). From these measurements, the combined GAD (black) is assembled as the composite of the GADs as determined for each Δx in the grain-area intervals as indicated by the vertical dashed lines.

with nucleation and growth rates prescribed by an underlying kinetic model. Nucleation, growth and impingement of spheres is carried out in discretised space and time. The simulated microstructure after completed recrystallisation can be analysed in the same way as done for the experimental results.

In this article, geometric simulations are employed to assess whether the microstructure as predicted by a specific kinetic model matches with the experimentally determined microstructure. In particular, grain-area distributions as determined experimentally and as generated by simulations are compared. The algorithm used for these simulations is described in detail in Ref. [35].

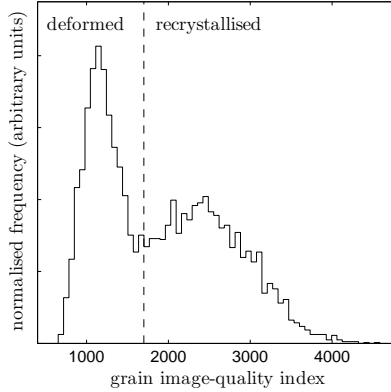


Figure 6.3: A histogram of the average grain-image quality index of a partially recrystallised (at $T_{\text{iso}} = 413 \text{ K}$ (140°C); $f = 0.67$) specimen as determined by an EBSD measurement. All grains with image qualities below the dashed line are considered as unrecrystallised (deformed) while all grains with a higher image quality are considered as recrystallised.

6.4 Results and evaluation

6.4.1 Calorimetry

The difference between the recorded heat flux signal and the constructed base line was determined (as described in section 6.3.2 [cf. equation (6.2)]). Thus the released heat due to only the recrystallisation ($-\Delta H_{\text{ReX}}$ with H_{ReX} as enthalpy) has been obtained. The determination of the recrystallised fraction, f , as function of t then is straightforward. If $\Delta H_{\text{ReX,tot}}$ represents the total enthalpy change of recrystallisation (the area under the $d\Delta H/dt$ vs. t curve), it follows:

$$\frac{d(\Delta H)}{dt} = \Delta H_{\text{ReX,tot}} \left(\frac{df}{dt} \right) \quad (6.3)$$

and f as a function of t follows by stepwise application of equation (6.3). The resulting course of the recrystallised fraction as a function of time is shown for various isothermal annealing temperatures in figure 6.4.

If the recrystallisation kinetics can be described by the classical JMAK model, a straight line arises by representation of the experimental results

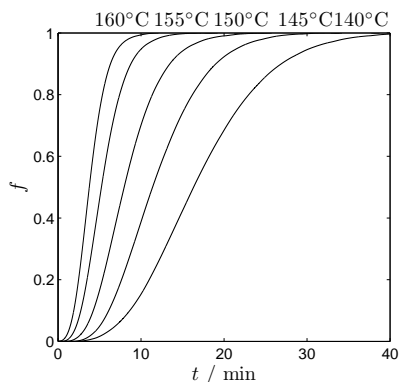


Figure 6.4: The recrystallised fraction, f , determined by isothermal DSC, as function of time at various temperatures.

in the double-logarithmic plot: $\ln(-\ln(1-f))$ vs. $\ln(t)$ (cf. equation (6.1) in section 6.2.1). As follows from figure 6.5 a), straight lines of slope three (i.e. $n = 3$) can be well fitted to the first half of the data points (i.e. to about $f \approx 0.6$) of each run. For $f > 0.6$, the slope decreases until the end of the recrystallisation. These results are more or less in line with literature results: slopes (=values of the growth exponent, n) between 0.8 and 4.6 were observed and a decrease of the slope in the late stage of recrystallisation was often found (see section 6.2.1). Evidently, the classical JMAK model provides an imperfect description of the recrystallisation kinetics.

Independent of the adoption of a specific kinetic model, a value for the effective activation energy, Q_{eff} , can be determined from a set isothermal annealing runs [1,29]. In a plot of the logarithm of the time elapsed between two fixed fractions transformed, $\ln(\Delta t)$, versus the inverse of the isothermal annealing temperature, T_{iso}^{-1} , the effective activation energy, Q_{eff} , can be determined as the slope of the resulting straight line (cf. section 6.2.1). Here, the time elapsed from the beginning of the measurements ($f' = 0$) until various fixed fractions recrystallised, f'' , was employed. The value thus determined for Q_{eff} decreases from 112 to 110 kJ mol^{-1} for f'' changing from 0.2 to 0.8 (see figure 6.5 b). This result for Q_{eff} is within the large range of the values found in the literature. (see Table 6.1).

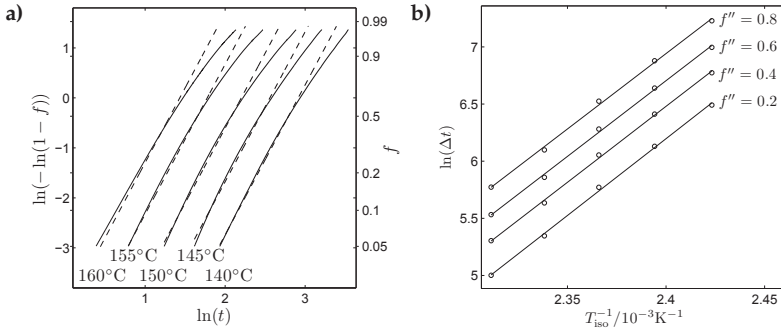


Figure 6.5: a) The double-logarithmic plots of the recrystallised fraction, f , as determined from isothermal DSC runs at various temperatures (cf. figure 6.4). The dashed lines of slope three were fitted to the first half of the recrystallisation curves. b) A plot of $\ln(\Delta t)$ vs. T_{iso}^{-1} used to determine the effective activation energy of the recrystallisation, for various values of the recrystallised fraction, f'' . For all curves, $f' = 0$ was chosen (see section 6.2.1 and Ref. [1]).

6.4.2 EBSD

The recrystallised fraction as determined from the EBSD scans (according to the method described in section 6.3.3) is shown in figure 6.6 (data points) for the recrystallisation at $T_{\text{iso}} = 413\text{ K}$ (140°C). The error bars included in figure 6.6 for the EBSD data points result from different choice of threshold values for the image-quality index to separate the fractions of recrystallised material and unrecrystallised material in a partially recrystallised specimen. The full line drawn in the figure represents the recrystallised fraction as determined by DSC for an identically conducted experiment. The DSC curve was shifted by one minute to shorter times in order to obtain the best match with the EBSD data. This small correction is a consequence of recrystallisation already beginning during the heating up to the measurement temperature in the isothermal DSC experiments, whereas specimens used for EBSD analysis practically immediately reached the annealing temperature in the oil-bath annealings performed. It follows that the degrees of transformation as determined by DSC and EBSD agree very well. Thereby, the base-line construction applied in the DSC measurement (cf. section 6.3.2) is

validated. The result also indicates that there is no substantial amount of recovery occurring during the recrystallisation, because if this were the case, a deviation of the DSC measurements (which capture the heat release due to recovery) from the EBSD measurements (which are insensitive to recovery) would be observed (see also the discussion at the end of section 6.2.1 and see sections 6.3.1 and 6.3.2).

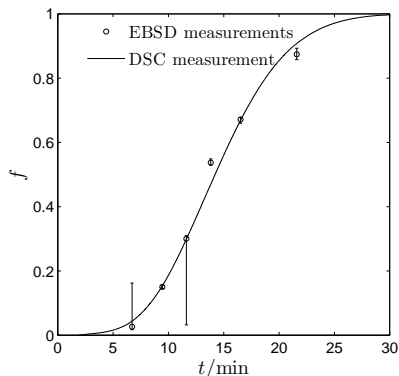


Figure 6.6: The transformed fraction as determined from EBSD measurements for recrystallisation at $T_{\text{iso}} = 413 \text{ K}$ (140°C) (data points), as function of time. The error bars indicated for the data points result from choosing different image-quality thresholds in the analysis of the EBSD measurements (cf. section 6.3.3). The full line represents the recrystallised fraction as determined by DSC for an identically conducted experiment. The DSC curve is shifted by one minute to shorter times to obtain the best match with the EBSD results.

A grain-orientation map of a deformed (and recovered) specimen is shown in figure 6.7 a). The different colours denote the surface normal in the crystal frame of reference. Orientation gradients (different shades of the same colour) are visible within grains (and subgrains). The grain boundaries determined from the measurement are shown in figure 6.7 b). Low-angle grain boundaries (misorientation angles of adjacent pixels $5^\circ < \omega < 15^\circ$ ²⁰) are shown in grey and high-angle grain boundaries ($\omega > 15^\circ$) are shown in

²⁰If the misorientation between two pixels is smaller than five degrees, the pixels are considered to belong to the same grain.

black. The mean subgrain diameter is approximately $3\ \mu\text{m}$. The corresponding image-quality map of the EBSD scan is shown in figure 6.7 c). The subgrain structure within grains is revealed by the relatively low image quality of pixels (appearing relatively dark) on the subgrain boundaries.

A similar analysis for a partially recrystallised specimen is shown in figure 6.8 a). Here, the grain-orientation map is shown with the image-quality map superimposed in the same figure. Bright grains (i.e. grains with a high average image quality) are recrystallising grains growing into the surrounding deformed matrix. All growing grains comprise parts in orientations due to (multiple) twinning. This can be seen by comparing figure 6.8 a) with figure 6.8 b) where all parts of a recrystallised grain in twin orientation relationships with adjacent parts in the same recrystallised grain have been given the same colour. The boundary between recrystallised and unrecrystallised material is irregular and not flat as it would be expected for an isotropic growth rate: protrusions and retrusions can be observed.

The EBSD scan for a fully recrystallised microstructure is depicted in figure 6.9. The grain-orientation map is shown with the image-quality map superimposed in figure 6.9 a). For the same area as in figure 6.9 a), only the grain boundaries are shown in figure 6.9 b): high-angle grain boundaries are shown as black lines; twin boundaries (coherent and incoherent) are shown in grey. There are almost no small-angle grain boundaries (misorientation angle $5^\circ < \omega < 15^\circ$; shown in red). Most of the grains are irregularly-shaped. Very large as well as very small grains occur in the microstructure.

The evolution of the grain-area distribution of recrystallised grains with ongoing recrystallisation is presented in figure 6.10, where histograms of the logarithm of recrystallised grain areas are shown for various partially and one fully recrystallised specimen. For the first histograms, the number of recrystallised grains and hence the accuracy are not very good, but it is clear that already at low transformed fractions there are large recrystallised grains in the microstructure. The shape of the grain-area distribution remains more or less unchanged from $f = 0.67$ onwards. For a process with pre-existing nuclei (as often assumed in the modelling of recrystallisation, see e.g. Refs. [79,80]), it would be expected that the grain-area distribution is more narrow at the beginning and broadens only later as a consequence of impingement.

The observed microstructure could also be affected by processes other than recrystallisation, namely by grain growth after recrystallisation. This can be excluded by the comparison of the microstructures of a specimen which was quenched to room temperature immediately after the end of the observed heat effect in the DSC scan and of a specimen which was held at

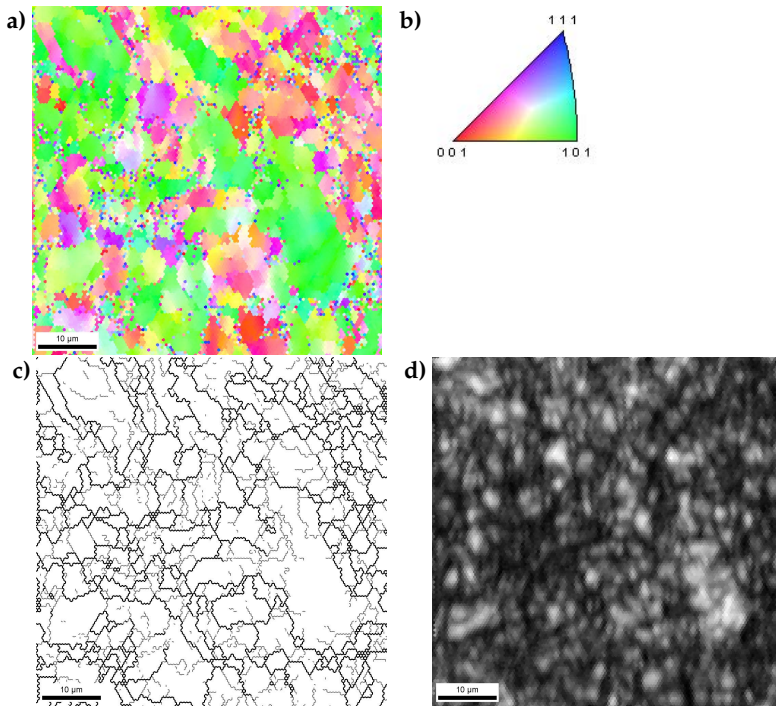


Figure 6.7: a) The grain-orientation map of a deformed specimen. The colours indicate the surface normal in the crystal frame of reference (see colour legend in the standard stereological “triangle” on the right). b) The grain boundaries determined from the measurement. Low-angle grain boundaries ($5^\circ < \omega < 15^\circ$) are shown in grey and high-angle grain boundaries ($\omega > 15^\circ$) are shown in black. c) The image-quality map of the same specimen (bright: high image quality, dark: low image quality).

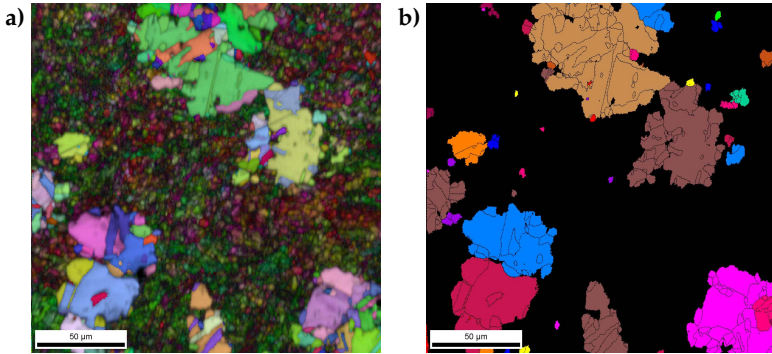


Figure 6.8: An EBSD scan of a specimen partially recrystallised at $T_{\text{iso}} = 413 \text{ K}$ (140°C). a) The grain-orientation map (colours, see the legend in figure 6.7) with the image-quality map superimposed in the same image: regions of low image quality (unrecrystallised areas) are dark, while regions of high image quality (recrystallised grains) are bright. b) The same EBSD scan, with all grains below the image quality threshold marked in black. All parts of recrystallised grains in twin orientation relationships with adjacent parts in the same recrystallised grain have been given the same colour. Evidently, many twin grain boundaries occur inside the recrystallised grains.

the recrystallisation temperature of 413 K (140°C) for one additional hour after the end of the observed heat effect. The GADs of the two specimens were identical within the experimental accuracy; in particular, a large number of very small grains (which should vanish rapidly during coarsening) was still present after the annealing treatment.

The number of observable recrystallised grains in the EBSD scans per unit area, N_A , has been plotted versus the recrystallised fraction in figure 6.11 a) The corresponding results of mesoscopic simulations (see section 6.3.4), assuming either pre-existing nuclei or continuous nucleation, i.e. with a constant nucleation rate at constant temperature per (unrecrystallised) unit volume, have been presented in the same figure. In both simulations, a constant, isotropic growth rate was employed. The number of recrystallised grains per unit area was normalised by the number of recrystallised grains per unit area observed in the fully recrystallised specimen. The experimental data show that the number of observable grains increases

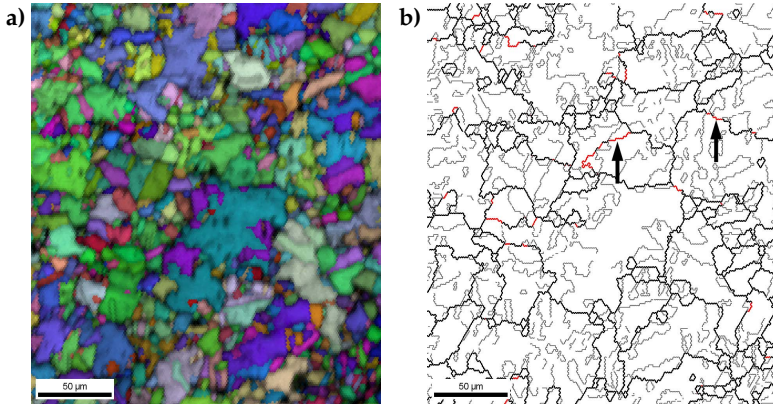


Figure 6.9: An EBSD scan of a specimen fully recrystallised at $T_{\text{iso}} = 413$ K (140°C). a) The grain-orientation map (colours, see the legend in figure 6.7) with the image-quality map superimposed in the same image: regions of low image quality (unrecrystallised areas) are dark, while regions of high image quality (recrystallised grains) are bright. b) The grain-boundary types observed: low-angle grain boundaries ($\omega < 15^\circ$, marked in red; see arrows), twin boundaries (coherent and incoherent, grey) and general high-angle grain boundaries ($\omega > 15^\circ$, black).

relatively slowly in the beginning, and increases rapidly towards the end of the recrystallisation. This is in contrast with the results from both simulations, which show a rapidly increasing number of grains in the beginning, followed by a slower increase towards the end of the recrystallisation.

The recrystallised/unrecrystallised interface area per unit volume (see procedure described at the end of section 6.3.3) as function of the recrystallised fraction is shown in figure 6.11 b)²¹. The maximum of the experimental data in this plot occurs at a slightly higher transformed fraction than as predicted by the simulations assuming pre-existing nuclei or continuous nucleation. This means that a relatively large unimpinged surface area unrecrystallised/recrystallised is present relatively late in the experimentally observed recrystallisation. Such a situation could, for example, be due to a high nucleation rate at late stages of the recrystallisation (since small grains

²¹This plot and its analysis is referred to by some authors as the microstructural path method [82,106].

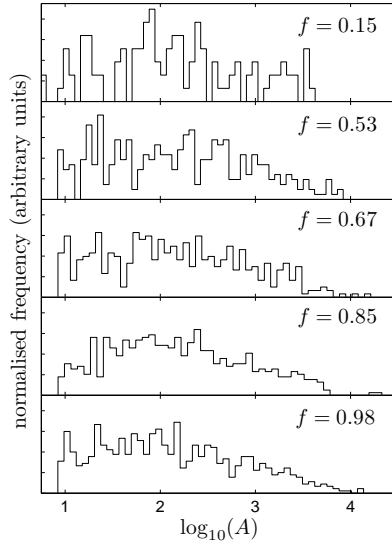


Figure 6.10: The logarithmic grain-area distributions of recrystallised grains as determined by EBSD measurements for partially and fully recrystallised specimens at $T_{\text{iso}} = 413 \text{ K}$ (140°C).

have a higher surface-to-volume ratio than large grains), or due to the irregular shape of the grains (leading to a higher surface-to-volume ratio than for regularly shaped grains).

The surface-normal inverse pole figures of a deformed specimen and an of an entirely recrystallised specimen, as obtained from the EBSD measurements, are presented in figure 6.12. The surface-normal inverse pole figure of the deformed specimen is typical for fcc metals deformed under uniaxial compression, and not for rolled fcc metals [107]. This is a consequence of the rotation of the copper specimen around the sheet normal after each pass during rolling (cf. section 6.3.1). The texture of the recrystallised specimen does not match the texture expected for cold-rolled and recrystallised fcc materials, i.e. it does not exhibit a strong cube texture with many $\{100\}$ -planes parallel to the specimen surface [60, 107]. Instead, many grains with $\{111\}$ -planes parallel to the specimen surface are found.

A single (inverse) pole figure only contains incomplete information about the texture of a specimen. The orientation-distribution function, which con-

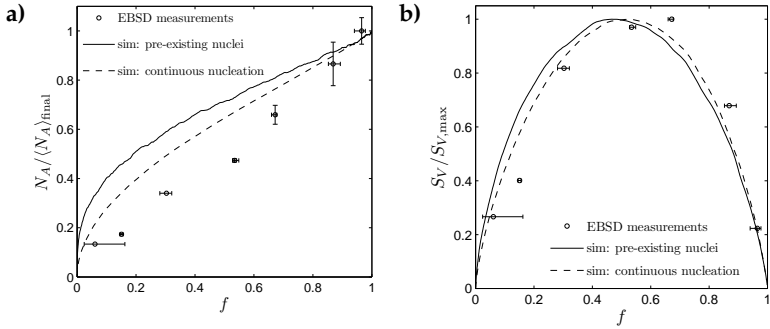


Figure 6.11: a) The normalised number of recrystallised grains per unit area as a function of time and b) the (unimpinged) recrystallisation front area per unit volume as function of the recrystallised fraction (at $T_{\text{iso}} = 413 \text{ K}$ (140°C)). Experimental results from EBSD measurements are shown (data points). The error bars result from choosing different image-quality thresholds in the analysis of the EBSD measurements. The corresponding results from mesoscopic simulations, assuming either pre-existing nuclei (solid line) or a constant nucleation rate (dashed line) and, for both cases of nucleation, a constant, isotropic growth rate, are shown as well.

tains the full information about the texture of a specimen, is also available from EBSD measurements and can thus be used as input data in mesoscopic simulations (see what follows).

The mobility of the moving interface recrystallised/unrecrystallised is strongly dependent on the misorientation angle of the growing grain with respect to the surrounding deformed matrix. Hence, to set up simulations with realistic misorientation-angle distributions, knowledge of (even; see above) the ODF of the deformed and recrystallised material is insufficient [108], since no information about the position of the grains in the specimen is contained in such data. However, from the EBSD measurements, misorientation-angle distributions can be obtained. Such results for both deformed specimens and fully recrystallised specimens are shown in figure 6.13. In the deformed state, many low-angle grain boundaries are present. This results from the formation of subgrains (with low-angle subgrain boundaries consisting of arrays of dislocations) during recovery. The misorientation-

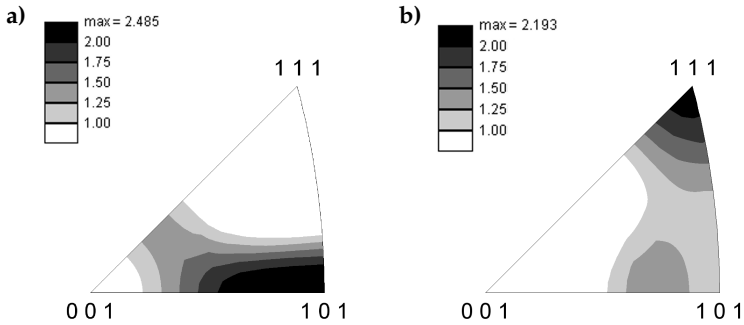


Figure 6.12: The surface-normal inverse pole Figure for the specimen surface (rolling plane) as obtained by EBSD of a) a deformed specimen (cf. section 6.3.1) and b) a specimen fully recrystallised at $T_{\text{iso}} = 413 \text{ K}$ (140°C). The values given for the levels of the iso-frequency contours shown have been indicated in the top left of the panels as $i \times \text{random}$, where “random” pertains to the frequency level in the absence of preferred orientation and with i as the number indicated.

angle distribution of the recrystallised specimen follows closely the Mackenzie distribution [109] which represents the case of randomly oriented grains of cubic material. Hence, even though the texture of the fully-recrystallised specimen (see figure 6.12) is not random, the spatial distribution of the grains in the specimen is random and therefore no clustering of misorientation angles can be observed.

6.5 General Discussion

Adopting a JMAK-model description for isothermal recrystallisation, the slope of a double-logarithmic plot equals the growth exponent, n , which depends on the nucleation and growth modes. The likely mode of growth is “interface controlled” and the dimensionality of the growth is three (grains grow in all three dimensions, i.e. in an equiaxed fashion). For this growth mode and pre-existing nuclei (site saturation), the growth exponent equals three; for this growth mode and continuous nucleation (constant nucleation rate at constant temperature), the growth exponent equals four [8]. The

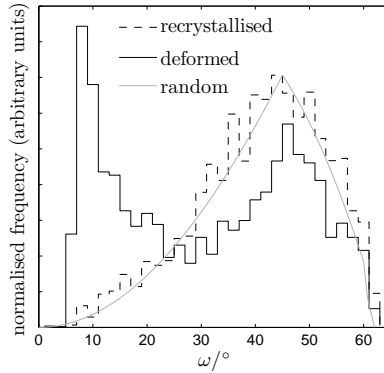


Figure 6.13: The misorientation-angle distribution functions for neighbouring grains of a deformed specimen (dashed line) and of a fully recrystallised specimen (solid line, without twin boundaries) obtained by EBSD. The Mackenzie distribution, i.e. the case of randomly oriented grains of cubic material, is also shown.

experimental results indicate $n = 3$ for $f < 0.6$ (figure 6.5). Hence, this discussion would lead to the conclusion that all nuclei are present at the beginning of the recrystallisation and that the observed value for the effective activation energy represents the activation energy of growth, i.e. in this case the activation energy of the mobility of the recrystallisation front. However, the microstructural results presented in this paper show that such an interpretation, as based only on calorimetric data, is unjustified (see what follows).

The grain-area distribution expected for the case of pre-existing nuclei and, as assumed in JMAK kinetics, isotropic growth is much narrower than the one observed experimentally. This follows from figure 6.14, where the GAD of figure 6.10 has been replotted together with corresponding results of simulations, including simulations according to JMAK kinetics with pre-existing nuclei.

A wide grain-area distribution skewed towards large grains, as observed experimentally, can be generated if nucleation continues during recrystallisation, e.g. if, for isothermal recrystallisation, continuous nucleation, or even an *accelerating* nucleation rate during recrystallisation is assumed [35, 76]. Also the experimental result for $N_A(f)$, which shows a steep increase

in the number of nuclei per unit area in a cross section towards the end of recrystallisation (figure 6.11 a), could be explained with an accelerating nucleation rate. Adoption of any model with ongoing nucleation would, however, lead to a growth exponent larger than three, which is not observed (figure 6.5 a). Moreover, such models are still JMAK-like models which would lead to straight lines in double-logarithmic plots (cf. Ref. [8]) and thus cannot describe the experimentally observed departure from JMAK-like behaviour in the late stages of recrystallisation (figure 6.5 a).

The above consideration indicates that additional effects must be taken into account to reconcile kinetics and microstructural observations.

Decreasing growth rate. An accelerating nucleation rate together with a decreasing growth rate could likely explain the broad grain-size distribution (cf. Ref. [76]) and the observed slope of three in the double-logarithmic plot. However, even an exponentially decreasing growth rate leads to a straight line in the double-logarithmic plot (see section 6.2.1 and the discussion in Ref. [60]). Therefore, the observed kinetics cannot be described with such a model.

Non-random nucleation. Nuclei which are spatially inhomogeneously distributed, e.g. along grain boundaries in the parent microstructure, cannot be described with JMAK-like models and show a decreasing slope in double-logarithmic plots [11]. Nucleation in recrystallisation is known to occur preferentially in regions of high misorientation gradients, i.e. at grain boundaries in the deformed microstructure [60,75]. However, there is no evidence that the observed kinetics are due to non-random nucleation in the present experiments: Grain-boundary nucleation, as compared to random nucleation, only affects transformation kinetics and the final microstructure noticeably if there are many more product nuclei than parent grains, i.e. if the nuclei saturate the parent-grain boundaries [11,61,71]. In that case, a string-of-pearl pattern of grains along parent-grain boundaries would be visible in partially recrystallised specimens. Since this is not the case (see figure 6.8), it is unlikely that non-random nucleation is responsible for the observed kinetics.

Inhomogeneous growth rate. Another possible reason for the observed departure from JMAK kinetics is an inhomogeneous growth rate [100]. Assuming that all stored energy is released during recrystallisation, the interface velocity of a migrating recrystallisation front depends on the local

driving force, i.e. the energy stored in the deformed matrix before the front, and the mobility of the interface, which strongly depends on the misorientation between deformed matrix and recrystallised grain [110]. Therefore, it is clear that the front velocity may change from location to location (and also the (average) front velocity may change as function of time).

In order to incorporate inhomogeneous growth rates in a simple model for the recrystallisation kinetics, it was assumed that there is a distribution of growth rates (i.e. each grain has its own, constant growth rate) instead of a common growth rate for all grains. Assuming a normal distribution of growth rates and pre-existing nuclei, it was found possible to fit the experimentally observed kinetics reasonably well (a simultaneous fit to all isothermal runs; see figure 6.15). However, the GADs resulting from corresponding simulations do not match the experimentally observed ones (see figure 6.14). So, although the recrystallisation kinetics can be described by this model (which is an improvement as compared to the JMAK model), the microstructure resulting from the recrystallisation is described imperfectly. It follows that any future testing of kinetic models for recrystallisation requires satisfactory descriptions of both the kinetics and the microstructure.

The occurrence of a significant variation in growth rate of recrystallising grains was ascribed above to a relatively large variation in driving force and microstructure in the deformed specimen. Such effects are much more pronounced for recrystallisation than for heterogeneous phase transformations: The driving force for recrystallisation is much smaller than for phase transformations [1, 110]. Even though fluctuations e.g. in the driving force may occur from location to location in the specimen for massive or precipitation transformations, the relative changes are small and the driving force can be approximately taken as constant. In recrystallisation, on the other hand, fluctuations in the small driving force may even lead to some regions not taking part in the recrystallisation at all.

The above discussed results indicate the necessity to develop models which explicitly take into account the inhomogeneous nature of the deformed microstructure before recrystallisation and which incorporate realistic, “physical” models for the nucleation rate and the recrystallisation-front velocity, which models should be tested against experimental data for both the kinetics and the microstructural development.

Mesoscopic simulations are best suited to investigate such models. They can take experimental information about the deformed microstructure as input and allow the comparison of simulated kinetics *and* microstructure with

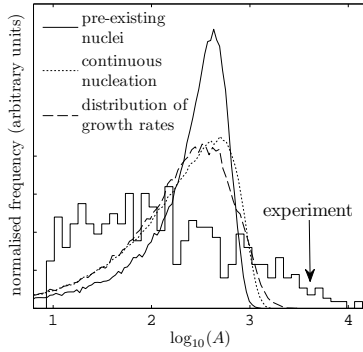


Figure 6.14: The GAD of a fully recrystallised specimen as determined by EBSD together with predictions by various simulations. Solid line: assuming pre-existing nuclei and a uniform growth rate; dotted line: assuming a constant nucleation rate and a uniform growth rate; dashed line: assuming pre-existing nuclei and a distribution of growth rates.

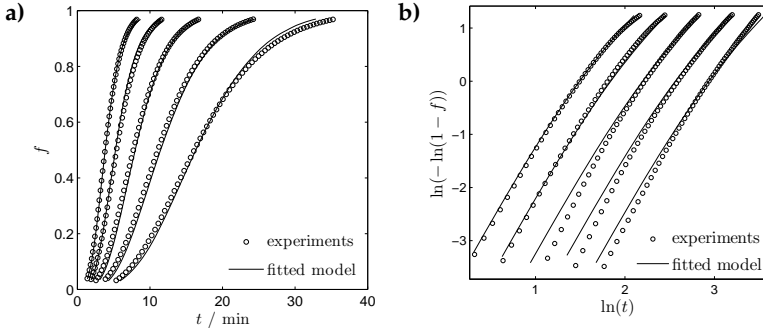


Figure 6.15: a) The transformed fraction as a function of time determined by DSC measurements (data points), see figure 6.4 b) together with the result of fitting a kinetic model simultaneously to all isothermal runs, assuming pre-existing nuclei and a normal distribution of growth rates. b) A double-logarithmic plot of the same data.

experimental data such as those presented in this work. Therefore, Cellular Automata simulations will be employed in a forthcoming article [111] to simulate recrystallisation departing from an inhomogeneous deformed state.

6.6 Conclusions

6.6.1 Recrystallisation of copper

- The kinetics determined for the static recrystallisation of strongly deformed copper by DSC and EBSD agree very well.
- The growth exponent equals three up to a fraction recrystallised of 0.6 and subsequently decreases. The recrystallisation kinetics cannot be described by a JMAK-like kinetic model.
- The grain-area distribution of recrystallised grains is very wide and includes very large grains already in early stages of the recrystallisation. After complete recrystallisation, it spans at least five orders of magnitude of grain area ($10^0 - 10^5 \mu\text{m}$).
- The number of recrystallised grains per unit area observable in specimen cross sections increases slowly in early stages and quickly in late stages. This observation suggests that new recrystallised grains are formed not only at the beginning, but continuously during the recrystallisation.
- The grains in the fully recrystallised microstructure each consist of several parts sharing a twin orientation relationship. The grain boundaries are strongly curved and have an irregular shape. Although the recrystallised microstructure reveals a distinct texture, the misorientation-angle distribution for neighbouring grains is identical to the one expected for randomly oriented grains.
- The experimental data on the kinetics and the microstructure cannot be reconciled by neither a nucleation continuing (or even accelerating) during recrystallisation, nor a growth rate decreasing during recrystallisation, nor a spatially non-random nucleation and also not by a combination of these. A spatially varying growth rate, as a consequence of intrinsic microstructural inhomogeneity, is identified as the key to understand both the kinetics and the resulting microstructure of recrystallisation.

6.6.2 Recrystallisation in general

- A viable model for the recrystallisation kinetics should be able to describe both the dependency of the recrystallised fraction on time and/or temperature and the microstructural development; e.g. as exhibited by the grain-area distribution. An acceptable fit of a JMAK(-like) or other model to only the fraction recrystallised as function of time or temperature is possible in many cases without that the generated microstructure can be predicted reliably. This invalidates a considerable body of conclusions presented in previous works.
- On the one hand, models pertaining to a decreasing growth rate and/or accelerating nucleation rate predict microstructures with broad grain-area distributions, potentially as broad as the observed ones, but are not able to describe the observed recrystallisation kinetics.
- On the other hand, a model pertaining to pre-existing nuclei and a distribution of (constant) growth rates can explain the observed recrystallisation kinetics, but the predicted microstructure (grain-area distribution) does not comply with experimental results.
- Models which incorporate the inhomogeneous nature of the deformed microstructure, and thus the variation from location to location of the driving force and the recrystallisation-front mobility, may correctly describe both the observed recrystallisation kinetics *and* the extraordinarily wide grain-area distribution. Such models can be implemented in mesoscopic simulations.

Chapter 7

Interplay of kinetics and microstructure in the recrystallisation of pure copper: comparing mesoscopic simulations and experiments

7.1 Introduction

Already some of the earliest works on mesoscopic microstructure simulation have treated the process of recrystallisation in metals [12, 76, 112]. This can be understood as a consequence of the great technological importance of recrystallisation and the recognition that the usually applied simple recrystallisation models fail to correctly describe both the experimentally observed kinetics and the resulting microstructure.

In particular, two experimental results could not be conclusively explained yet and thus give rise to enduring interest in recrystallisation: *Firstly*, the kinetics of (isothermal) recrystallisation show a time dependence which cannot be explained with simple Johnson-Mehl-Avrami-Kolmogorov (JMAK)-models [5–7] based on a constant growth rate of recrystallised grains [83]: In so-called double-logarithmic plots of $\ln(-\ln(1-f))$ versus $\ln(t)$, with f being the fraction recrystallised and t being the time elapsed since the start of the recrystallisation, a straight line results if the recrystallisation can be described by the classical JMAK model (for a discussion of JMAK(-like) models, see Ref. [1]). The frequently observed deviation from a straight line towards the end of the recrystallisation has been interpreted as a result of a decreasing growth rate of recrystallised grains [60, 87]. *Secondly*, the grain-size distributions of the microstructures generated by physically conceivable models considered in computer simulations are (so far) consistently and distinctly narrower than the ones observed experimentally [79, 99].

Even though broad grain-size distributions can of course always be generated by devising arbitrary nucleation and growth models in computer simulations [56, 76], the question arises what the physical background of such nucleation and growth models could be, if there is any. In more recent recrystallisation models, the nucleation and growth rates are defined dependent on the deformed microstructure at the onset of recrystallisation

(see, e.g., Refs. [60,75,77,79]). The reason for the decreasing growth rate (see above) is then believed to originate from the inhomogeneity of the deformed microstructure, in which, during the annealing, new nuclei are forming and into which the recrystallising grains are growing.

In recrystallisation simulations departing from an inhomogeneous, deformed microstructure, it is very important to describe this microstructure, i.e. the start configuration of the simulation, as accurately as possible. Most published works on the simulation of recrystallisation which do investigate the influence of the deformed microstructure on recrystallisation depart from a lightly deformed microstructure (true strain $\epsilon < 1$), which is incompatible with practical recrystallisation processes. Such a microstructure usually consists of subgrains/dislocation cells²², delineated by low-angle grain boundaries, within the deformed, original grains, delineated by high-angle grain boundaries, which are still visible. In corresponding simulations, deformed grains are either assumed to have a homogeneous stored energy and no subgrain structure [78,79], or a stored energy gradient is artificially generated inside the grains [113], or the grains contain a subgrain structure [114], or information about the deformed microstructure and stored energy are taken from crystal-plasticity FEM simulations [115–117]. In all these cases, high-angle boundaries (which provide the migrating recrystallisation fronts) are only present at the original grain boundaries, so that nuclei emerge along these original grain boundaries and not randomly throughout the microstructure.

Simulations of strongly deformed metals have been scarcely performed. In strongly deformed metals (true strain $\epsilon > 1$), the original grain morphology is not well detectable any more and the assumption that the microstructure consists of well-defined subgrains (sharing low-angle grain boundaries) within large grains (delineated by high-angle grain boundaries) is untenable [60]. In EBSD experiments, low-angle and high-angle boundaries were found between microstructural features which were only a few micrometers wide [118] (Features of this size are typically subgrains and, in case of lightly deformed microstructures, are expected to be separated by only low-angle grain boundaries).

It is desirable to directly use such an experimentally observed, strongly deformed microstructure as start configuration of simulations. However,

²²The small features in deformed microstructures with dislocations forming more or less well-defined walls and relatively dislocation-free interiors are referred to as subgrains or dislocation cells in the literature. To avoid confusion between the “cells” in a deformed microstructure and the “cells” in a cellular automaton simulation, the term “subgrains” will be used for the former throughout this paper.

the simulations in which EBSD measurements of such microstructures were used for this purpose [80] have been restricted to two dimensions until now. In the current project, three-dimensional simulations of recrystallisation in such strongly deformed metals have been performed.

The kinetics and the microstructure of the recrystallisation of metals were simulated in the past using geometrical simulations, [12, 56, 119], phase-field simulations [114, 117], vertex dynamics simulations [120], Potts Monte-Carlo simulations [78, 80, 100] and cellular automata [16, 17, 121, 122]. Especially the latter two methods offer a high flexibility in the possible models which can be employed to describe nucleation and boundary migration (i.e. growth) during recrystallisation and are less computationally expensive than phase-field simulations.

In this paper, the kinetics and the resulting microstructure of copper which has been strongly deformed by cold-rolling ($\epsilon = 3$) have been investigated by comparison of the results of cellular automata simulations with experimental data. Informations about the microstructure of the deformed material were taken from a comprehensive data set on the the recrystallisation of pure copper presented elsewhere [118].

It is attempted to reconcile the experimentally observed kinetics and the (resulting) microstructure by applying three different approaches. Firstly, it is investigated whether anisotropic growth, due to an interface velocity which depends on the misorientation between the recrystallising grains and the deformed matrix, can lead to the observed decreasing growth rate, and to (non-spherical grains corresponding with) a broad grain-size distribution. Secondly, it is investigated if ongoing nucleation during recrystallisation can broaden the grain-size distribution enough to explain the experimental findings. Thirdly, the effect of subgrain-energy distributions, i.e. an inhomogeneously distributed stored energy, leading to a distribution of growth rates, is considered.

7.2 Experimental results

This section provides a brief summary of our recent experimental results on the recrystallisation of copper [118], which are essential for the understanding of the present paper. The kinetics of the recrystallisation of pure copper which has been strongly deformed by cold rolling ($\epsilon = 3$) was investigated upon isothermal annealing using differential scanning calorimetry (DSC). The microstructure, as reflected in grain-size parameter distributions and the image-quality index, was characterised in the deformed, partially

recrystallised and fully recrystallised states by orientation imaging microscopy using electron backscatter diffraction (EBSD) [118].

Deformed microstructure. The original grain morphology before rolling is not clearly visible any more in the deformed (and recovered) specimens. A distinction between small original grains and deformation-induced subgrains within original grains cannot be made. The majority of grain boundaries are high-angle grain boundaries (misorientation angle²³ $\omega > 15^\circ$), but the misorientation-angle distribution shows a higher number of low-angle grain boundaries (LAGB) than expected for randomly oriented (sub-)grains (cf. also Figure 7.6 in section 7.5.1, where the misorientation-angle distribution of a deformed specimen is shown). The average area of the (sub-)grains in the microstructure is approximately $3 \mu\text{m}^2$.

Kinetics. In a double-logarithmic plot of the fraction recrystallised as function of time, a straight line with slope three results for all annealing temperatures, up to a recrystallised fraction, f , of approximately 0.6. For $f > 0.6$, the slope of the plot, the so-called JMAK-exponent, drops slightly (cf. Figure 7.5 in section 7.5.1). There is no recovery taking place during recrystallisation as follows from the coincidence of the DSC and EBSD data for the fraction recrystallised.

Observed number of grains per unit area. The number of grains which can be observed in a cross section rises only slowly at the beginning of the recrystallisation, but increases faster towards the end of the recrystallisation (cf. Figure 7.9 in section 7.5.2).

Recrystallised microstructure. The recrystallised microstructure includes many twins, however all grains sharing twin orientation relationships were counted as one grain since they develop from an already-existing recrystallised grain. The grain boundaries between recrystallised grains are not smooth, but strongly curved/ irregular.

Final grain-area distribution. The grain-area distribution after completed recrystallisation is extremely broad: it spans at least five orders of magnitude (the smallest grains could not be resolved with the employed res-

²³The difference in crystallographic orientation of two (adjacent) otherwise identical crystals can always be described as a rotation around a specific axis.

olution) and has its maximum at small grain areas (cf. Figure 7.4 in section 7.5.1).

7.3 Employed nucleation and growth models

7.3.1 “Nucleation”

“Nucleation” in recrystallisation is not a fluctuation phenomenon like in (solid-solid) phase transformations. Instead, the “nuclei” are already present in the deformed material in the form of subgrains which can become “activated” or “supercritical”, i.e. become “nuclei”, if certain instability criteria are (all) fulfilled [1,60,74,75]:

1. The boundary curvature must be (become) below a critical value (i.e. the subgrain radius must be larger than the critical radius, r^*),
2. there must be (develop) a mobile (i.e. high-angle) grain boundary as part of the subgrain boundary and
3. there must be (arise) a driving force for movement of the recrystallisation front (i.e. a difference between the stored energies at both sides of the migrating recrystallisation front).

Subgrains may fulfill these conditions already after deformation. Then one speaks of “pre-existing nuclei” or “site saturation (at $t = 0$)” [8].

The above listed conditions determining which subgrains are supercritical, may be a function of heat treatment time/temperature: (normal) subgrain coarsening can occur upon increasing time in isothermal experiments and upon increasing temperature in isochronal experiments and thereby subgrains adjacent to a high-angle grain-boundary can reach a size larger than the critical radius for “nucleation” in the course of ongoing recrystallisation (therefore, recrystallisation can be considered as “discontinuous subgrain coarsening”)²⁴.

Recently, a quantitative model for “nucleation” in recrystallisation has been developed based on the mechanism of subgrains becoming supercritical

²⁴A different model for “discontinuous subgrain coarsening” assumes that the subgrain-size criterion is fulfilled for most subgrains but that they only have immobile, low-angle grain boundaries with their neighbours. Normal subgrain growth then leads to a situation in which individual subgrains can obtain mobile, high-angle grain boundaries with their neighbours, e.g. by continuous merging of low-angle grain boundaries [1,60] and then start to grow, i.e. coarsen discontinuously [123].

upon (normal) coarsening [77]. The critical subgrain radius for nucleation is given by [60]

$$r^* = \frac{2\gamma_{\text{HAGB}}}{-\Delta G}, \quad (7.1)$$

where γ_{HAGB} is the boundary energy of the high-angle grain boundary created/ extended during “nucleation” and $-\Delta G$ is the driving force for recrystallisation, i.e. the stored energy in the deformed microstructure. Under the assumption that the stored energy of the deformed, parent microstructure is mainly located in the subgrain boundaries, equation (7.1) can be rewritten as [1,60]

$$r^* = \frac{4}{3} \langle r_{\text{subgrain}} \rangle \frac{\gamma_{\text{HAGB}}}{\gamma_{\text{subgrain}}}, \quad (7.2)$$

where $\langle r_{\text{subgrain}} \rangle$ is the average subgrain radius in the grain into which the new “nucleus” is growing and γ_{subgrain} is the boundary energy of a subgrain boundary. During subgrain coarsening, obviously $\langle r_{\text{subgrain}} \rangle$ increases, but since γ_{subgrain} increases at the same time (the misorientation angle at the subgrain boundary increases during subgrain coarsening), the critical radius can be considered to stay about constant during subgrain coarsening. This implies that only very little of the deformation energy is released during subgrain coarsening (i.e. no significant recovery takes place), which is in agreement with experimental findings for materials with low- to medium-stacking fault energies such as copper [60,88,118].

Subgrain coarsening follows a power-law behaviour [60], so that the average subgrain radius, $\langle r \rangle$, can be expressed as

$$\langle r \rangle^\beta - \langle r \rangle_0^\beta = kt, \quad (7.3)$$

using the initial average subgrain radius $\langle r \rangle_0$, the subgrain-growth exponent β (set to $\beta = 3$ in this work²⁵) and the subgrain-growth constant k . This equation can also be expressed as time dependence of the average subgrain radius normalised with respect to the critical subgrain radius, $\chi(t)$,

$$\chi(t) = \langle r \rangle(t) / r^* = \left(\langle r \rangle_0^\beta + kt \right)^{1/\beta} / r^*. \quad (7.4)$$

Thus, subgrains become supercritical if their normalised subgrain radius, $\chi(t)$, is larger than unity.

²⁵A range of values from $\beta = 2$ to 5 has been observed experimentally [60]. A sensitivity study concerning this parameter has been performed in this work and it was found that a variation of the value of β in this range does not qualitatively change the simulation results and thereby the conclusions drawn.

The spatial distribution of nuclei (random or non-random) can influence the kinetics and final microstructure of recrystallisation. When nuclei are arranged spatially non-randomly, e.g. along high-angle grain boundaries of the deformed material or as a consequence of the presence of non-randomly distributed, nucleation-stimulating second-phase particles, then the slope of a double-logarithmic plot of the recrystallised fraction as function of time (the JMAK exponent) decreases to a value of one towards the end of the transformation and the maximum of the resulting grain-size distribution is shifted towards smaller grain sizes [11, 41, 61, 84, 118]. However, the influence of non-random nucleation on the recrystallisation kinetics and the final microstructure will only be significant (if detectable at all) if the departure from a random nucleus arrangement is pronounced [71]. A strongly non-random arrangement of nuclei would be visible in partially recrystallised specimens [82]. Since no such distinctive departure from random nucleation could be observed during the recrystallisation of strongly deformed copper [118] (cf. also the discussion in Ref. [100]), non-random nucleation is not considered in the present recrystallisation model.

7.3.2 Growth

In early recrystallisation models, the interface velocity of a recrystallisation front, i.e. the growth rate of the recrystallising grains, was assumed to be constant. This assumption cannot be upheld in the light of experimental results. The slope of double-logarithmic plots (the JMAK exponent) was often found to be smaller than three, the lowest possible value compatible with a constant growth rate and any nucleation model. Particularly, the slope was often found to be decreasing towards the end of the recrystallisation. Microscopy studies also suggest a growth rate decreasing with progressing recrystallisation [83, 84, 87]. Against this background, a time dependence of the form $v = \text{const.} \times t^{-d}$ has often been assumed for the growth rate, v , with the exponent d ranging from 0.4 to 1 [60].

This model for the growth rate v is unsatisfactory, because it cannot explain the observed decrease in the JMAK exponent towards the end of the recrystallisation, apart from the empirical character of a relation for v as discussed. The decrease of the growth rate can be discussed as follows:

Classically, the velocity of a recrystallisation front is described by the product of the driving force for recrystallisation, $-\Delta G$, and the mobility of the migrating boundary, M

$$v = M(-\Delta G). \quad (7.5)$$

A decrease of the interface velocity can thus originate from a decrease of the grain-boundary/ recrystallisation-front mobility or from a decrease of the driving force.

The driving force for recrystallisation is the deformation energy stored in the initial microstructure. The driving force can be reduced by recovery. Such recovery can be excluded during the recrystallisation of pure copper (see the last section). If the stored energy is not distributed homogeneously in the deformed microstructure, it is possible that the *average* driving force, and hence the average interface velocity, decreases with time, since the regions with a high driving force recrystallise first²⁶.

The possible inhomogeneity in driving force on the length scale of the specimen cannot be very pronounced, because experimental techniques measuring the released enthalpy of the entire specimen (calorimetry) and techniques measuring the recrystallised area fraction of a small part of the specimen (such as EBSD) yield approximately the same results for the recrystallised fraction [88, 118]. However, on the length scale of subgrains, inhomogeneities in driving force may exist. Such small-scale inhomogeneities of the growth rate do not strongly influence the recrystallisation kinetics, but can change the shape of the recrystallising (growing) grains and hence have an influence on the grain-area distribution (GAD) after recrystallisation [83].

A decreasing growth rate may also be caused by a decreasing (average) interface mobility. The mobility is known to depend on the misorientation angle describing the misfit of the growing, recrystallising grain and the deformed, adjacent matrix into which the growth of recrystallised material occurs. Low-angle grain boundaries (LAGB) are virtually immobile. All high-angle grain boundaries (HAGB) have approximately the same mobility, with the exception of certain high-mobility high-angle grain boundaries (HMGB), e.g. the $\Sigma 7$ ($40^\circ \langle 111 \rangle$) grain boundaries in copper [60]²⁷.

When a recrystallising grain encounters a subgrain in the deformed matrix with respect to which it has a low misorientation, then a LAGB is generated. Since this newly formed boundary segment has a very low mobility,

²⁶Note that this explanation for a decreasing (average) interface velocity during recrystallisation only applies if the regions with high and low deformation energy are spatially distributed randomly in the specimen and if the length scale of the stored-energy inhomogeneity is of the same order of magnitude as the size of the recrystallising grains. If it is (much) smaller, each recrystallising grain sweeps through (very) many regions of different stored energy and thus the average interface velocity is constant throughout the recrystallisation (see also the discussion in Ref. [99])

²⁷It has also been argued that the crystal-lattice orientation with respect to the specimen frame of reference, and not the misorientation between recrystallising grain and deformed matrix, is responsible for the high growth rate of certain grains [83], i.e. grains belonging to certain texture components have an inherently higher growth rate.

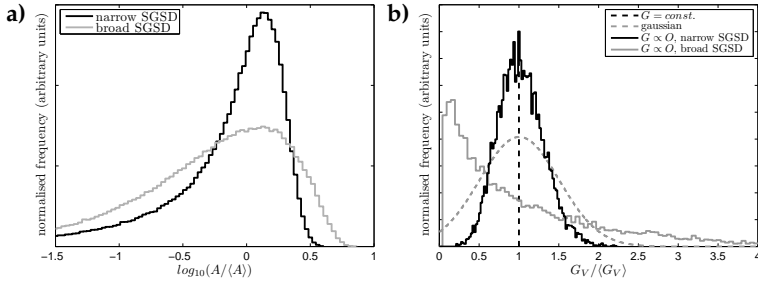


Figure 7.1: a) The two subgrain-size distributions used in the simulations, presented as logarithmic distributions of the normalised subgrain areas visible in a two-dimensional cross section. The subgrain structures were generated by geometric simulations with varied input parameters [35]. The narrow SGSD corresponds with a Voronoi-tessellation as subgrain microstructure. b) The subgrain-energy distributions (i.e. the number of subgrains with a certain deformation energy per unit volume) employed in the simulations, normalised by the average subgrain energy per unit volume. The distributions resulting for subgrain energies proportional to the subgrain surface areas correspond with the assumption that all of the deformation energy in the deformed structure is stored in the subgrain boundaries.

the growth of the concerned recrystallising grain is slowed down. If a grain shares LAGBs with *all* neighbouring (deformed) subgrains, it is almost completely prevented from further growth. This situation is termed “orientation pinning” [83]. If it occurs for a significant fraction of recrystallising grains, orientation pinning may be responsible for the observed decrease of the average growth rate of recrystallised grains in an advanced stage of the process.

7.4 Simulation method

7.4.1 Setup of the deformed microstructure

In lightly deformed metals, the original grain structure is still clearly visible after deformation. Inside these grains, a subgrain structure has developed which can be revealed by, e.g. EBSD measurements. In the present study

(pertaining to practical cases of recrystallisation), the deformation was so severe that the original grain structure could not be discerned well any more; it could not be established if a crystallite was a subgrain/cell (in a grain; see footnote 22 in section 7.1) or a small grain (as separate entity). Therefore, the deformed microstructure in the simulations was described on the basis of subgrains only.

The subgrain microstructure was generated by a geometrical simulation²⁸ (see Ref. [35] for a description of the algorithm). By changing the parameters of this simulation, it was possible to generate the desired average subgrain size and subgrain-size distribution (SGSD). In this paper, two different subgrain microstructures were considered: (i) a Voronoi tessellation [35,124], corresponding with a narrow, rather symmetric (with respect to the median) SGSD and (ii) a microstructure consisting of few large and many small grains, corresponding with a very broad and skewed SGSD (see Figure 7.1 a). These two microstructures will be referred to, by the shape of their SGSD, as “narrow” and “broad”, respectively.

In order to investigate the misorientation dependence of the interface mobility during recrystallisation with a close relation to reality, it is important that the experimentally obtained texture and the misorientation distribution (MOD) are adopted in the setup of the deformed microstructure. To do so, a Monte Carlo algorithm can be used [108], as follows.

Using the rejection sampling technique [70], this algorithm first assigns orientations to all subgrains such that the orientation distribution function (ODF) of the subgrains corresponds with the experimentally determined one. The location of the subgrains is not taken into account in this step. Next, two subgrains are chosen at random and it is checked whether exchanging the orientations of these two subgrains would bring the MOD of the entire subgrain ensemble “closer” to the desired, experimentally determined MOD (hereby, the “distance” of the two (binned) distributions is given by the sum of the squared differences of the numbers in each class of the histograms). Only if this is the case, the exchange is performed. Then, the next pair of subgrains is picked, etc. until a satisfactory match of the simulated MOD and the experimental MOD is obtained. Since grain orientations are exchanged in the algorithm and no new orientations are introduced, the ODF remains constant during this process. Hence, the thus resulting ODF and MOD of the simulated deformed microstructure are virtually indistinguishable from the experimentally determined ones (see Figure 7.6 in section 7.5.1).

²⁸Note that the geometrical simulation is used here merely to create a space-filling structure and

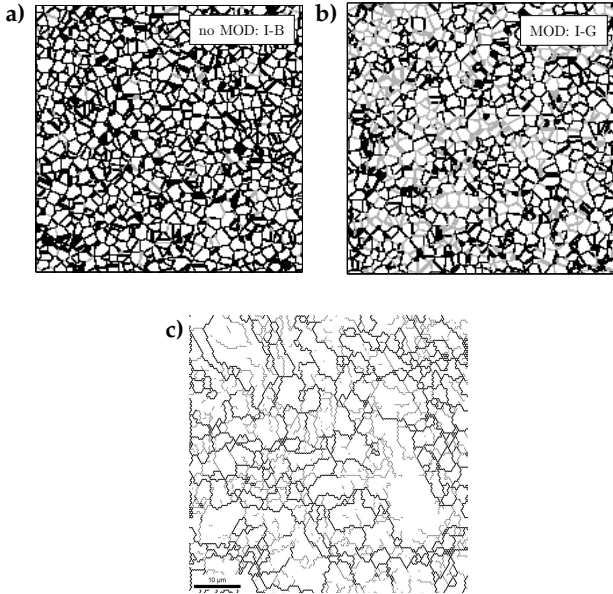


Figure 7.2: The subgrain structure used as start configuration for the simulations investigating misorientation-dependent mobilities. High-angle grain boundaries ($\omega > 15^\circ$) are shown in grey and low-angle grain boundaries ($\omega \leq 15^\circ$) are shown in black. a) If the subgrains orientations are chosen randomly and b) if the subgrain orientations are chosen according to the experimentally obtained ODF and arranged according to the experimentally obtained MOD. c) The grain boundaries in a cold-rolled copper specimen as determined by an EBSD measurement [118]. HAGBs are shown in black and LAGBs are shown in grey.

The effect of this procedure is exhibited in Figure 7.2, where the subgrain microstructure is shown before application of this algorithm (Figure 7.2 a: random distributions of subgrain orientations; i.e. random ODF and random MOD) and after application of this algorithm (Figure 7.2 b: ODF and MOD equal to the experimentally determined ones). The subgrain-boundary character is indicated by the colour of the boundaries: LAGBs are shown in

not to physically model the development of subgrains.

grey and HAGBs are shown in black.

In the simulations, the subgrain microstructure has been set up (i) with a random ODF and a random MOD, or (ii) with a random ODF but with a MOD corresponding with the experimental one (i.e. only the second part of the above described algorithm is applied), or (iii) with an ODF corresponding to the experimentally determined one and with a random MOD (i.e. only the first part of the above described algorithm is applied), or (iv) with both the experimental ODF and the experimental MOD taken into account (i.e. the entire algorithm described above is applied).

The ODF and the MOD together do not define a microstructure unambiguously. Even though the ODF and the MOD of the microstructure generated by the Monte Carlo algorithm are identical to the experimentally obtained distributions (cf. Figure 7.6 a), the appearance of the thus simulated microstructure is different from reality as represented by EBSD measurements (cf. Figures 7.2 b) and c)): both the subgrain-size distribution and the spatial arrangement of LAGBs and HAGBs differs.

The driving force for recrystallisation is the stored energy in the deformed microstructure. This stored energy can either be uniformly distributed in the deformed microstructure or the stored energy per unit volume can vary from subgrain to subgrain. For the latter case, the deformation energy per unit volume of the subgrains can either be obtained from a certain, adopted, deformation-energy distribution, e.g. from the gaussian distribution, or the deformation energy per unit volume of a subgrain can be connected to the subgrain size. If it is assumed that the stored energy is contained mainly in the dislocations forming the subgrain boundaries [114,123], then the energy of a subgrain, G , should be proportional to its surface area, O , (i.e. $G \propto O \propto V^{2/3}$, with V as the subgrain volume). The stored energy per unit volume within a certain subgrain, $G_V = G/V$, is then proportional to $V^{-1/3}$.

Subgrain-energy distributions (SGEDs, pertaining to the number of grains with a certain stored energy per unit volume) corresponding with these cases (uniform subgrain energy, gaussian SGED and subgrain-energy proportional to the subgrain surface area) are shown in Figure 7.1 b). In the simulations, the normalised stored energy per unit volume, i.e. $G_V / \langle G_V \rangle$, is used so that in all cases the same *average* stored energy per unit volume is employed. The broadest SGED corresponds with the case of subgrain energy proportional to the subgrain surface area and a broad SGSD.

7.4.2 Cellular automaton algorithm

For the present simulations of recrystallisation, a cellular automaton similar to the one used by Bos et al. [122] was employed. It is a fully deterministic automaton in which the cells²⁹ are arranged on a cubic lattice with periodic boundary conditions. Each subgrain/grain comprises a number of such cells. Unrecrystallised cells which lie at the boundary between already recrystallised and unrecrystallised regions are called “active cells”, because, different from recrystallised cells and unrecrystallised cells at a distance from the recrystallisation front, they are in principle able to recrystallise in the current time step. A list of active cells is compiled and kept updated throughout the simulation. This ensures that only a small fraction of all cells needs to be considered in each time step.

For each time step, it is first checked if there are subgrains (additionally to the already growing subgrains) which (now) fulfill the nucleation criteria. If this is the case, the nucleation for this subgrain is carried out (see section 7.4.3). Next, the list of active cells is updated. In the subsequent growth step, it is checked for each active cell whether the recrystallisation front should be advanced to include the cell under consideration (see section 7.4.4). If this is the case, the recrystallisation front is advanced accordingly. Finally, at the end of the time step, the following quantities are updated: the fraction of the total stored energy of the microstructure which has been released so far, f_H ³⁰, the volume fraction of the microstructure which has been recrystallised, f_V , the number of recrystallising grains (= the number of recrystallisation nuclei) per unit volume, N_V , and the number of recrystallising grains per unit area visible in a two-dimensional cross section of the microstructure, N_A .

After 99% of the initially stored energy has been released (i.e. $f_H > 0.99$), the automaton is stopped. The small amount of still unrecrystallised regions are assumed to be subject to insufficient driving force for recrystallisation. This corresponds to the experimental procedure in Ref. [118], in which specimens were cooled to room temperature after no further heat release could be detected in the calorimetric measurements.

²⁹Not to be confused with the subgrains/cells of the simulated and real microstructures; see footnote 22 in section 7.1.

³⁰The stored energy, which is the driving force ($-\Delta G$) of the recrystallisation can be taken as approximately equal to the enthalpy released ($-\Delta H$) during recrystallisation [2].

7.4.3 Nucleation

Nucleation of recrystallisation occurs when subgrains become “supercritical”. This can either occur by artificially defining a fixed number of subgrains as supercritical before the beginning of the simulation (as holds for the simulations described in section 7.5.1), or according to a certain nucleation condition, to be applied at each time step of the the simulation (as holds for the simulations described in section 7.5.2; see what follows).

A subgrain becomes supercritical if it is larger than the critical radius, r^* (see section 7.3.1). The critical radius depends on the driving force for recrystallisation (see equation (7.1)). Since in the simulations, a recrystallising nucleus/grain is assumed to have zero (deformation) energy, the driving force is equal to the (deformation) energy stored in the neighbouring unre-crystallised subgrain(s). Even though this deformation-energy difference is not uniform throughout the specimen in some of the simulations, an average, constant, value for the critical radius is assumed in each simulation (see also the discussion below equation (7.2)).

During subgrain coarsening, the criterion to decide if a particular subgrain i becomes a recrystallisation nucleus can be expressed as

$$r_i(t) > r^* \text{ or } \chi(t) = \frac{r_i(t)}{r^*} > 1, \quad (7.6)$$

where χ is the dimensionless, normalised critical subgrain size and $r_i(t)$ is the radius of the considered subgrain.

In order to avoid dealing with the computationally costly explicit simulation of subgrain coarsening during ongoing recrystallisation in the simulation, the subgrains retain their initial size, but, instead, the critical subgrain size, r^* , is (artificially, i.e. for the purpose of computational efficiency in the simulation only) decreased with time and the criterion for nucleation thus becomes

$$\chi(t) = \frac{r_i}{r^*(t)} > 1. \quad (7.7)$$

Therefore, the same time dependence of $\chi(t)$ is realised even though the microstructure (and hence, the radius r_i of each subgrain) remains unchanged. The microstructure developing upon recrystallisation, as described by the *normalised* grain-size distribution, then is independent of $\chi(t)$ being given by equation (7.6) or equation (7.7).

When a subgrain becomes supercritical, all cells inside the subgrain are instantaneously regarded as recrystallised by setting their deformation energy to zero and by adding this energy to the heat released by the recrystallisation. This means that the nuclei in such simulations are not of negligible

size, as is assumed in JMAK(-like) kinetic models [1]. Hence, if the kinetics of the recrystallisation is to be analysed using the double-logarithmic plots (JMAK plots; cf. section 7.1), this nonzero nucleus size must be accounted for. If all nuclei have the same size and grow at the same rate, this can be done by calculating the time which it (hypothetically) would have taken the nuclei to grow from negligible size until the size which they have when nucleation occurs, and then shifting the simulation start time (the zero point of the time scale) to an earlier time by this amount [125]. If this correction is not applied, erroneous JMAK plots and erroneous results for the JMAK-exponent result. This is exhibited by simulations pertaining to a homogeneous deformation energy in the deformed microstructure: without correction, they do not lead to straight lines in double-logarithmic plots (as would be expected). After applying the correction, the straight-line behaviour and the correct value of the JMAK-exponent is obtained.

In the present simulations, the focus is on recrystallisation in the presence of a distribution of subgrain size and therefore recrystallisation-nucleus size and also of a distribution of growth rates. Therefore, in view of the correction discussed above, the (hypothetical) start time can only be given as average value of all recrystallisation nuclei³¹. This leads to deviations from straight-line behaviour in the double-logarithmic plots in the early stages of the recrystallisation. The slope of the double-logarithmic plots in these early stages is therefore considered to be slightly unreliable.

The number of nuclei at the beginning of the simulation is chosen (by adjusting the value of the critical radius, r^*) such, that the size ratio between subgrains in the deformed state and grains in the recrystallised state corresponds roughly to the ratio found in experiments. For the considered case of recrystallisation of copper, this means that there are approximately 325 times more subgrains in the deformed state than grains in the recrystallised state (ca. 100 000 vs. ca. 300 for the simulations). Note that for simulations involving ongoing nucleation, the number of recrystallised grains also is approximately equal to 300 in the first time step, but increases during the simulation.

7.4.4 Growth

Growth is executed via the active cells, i.e. the cells with at least one adjacent (via face, edge or corner of the cell) recrystallised cell in their neighbourhood of 26 cells (cubic grid). Consider the moment at which a particular cell i in

³¹Note that the average size of the recrystallisation nuclei is larger than the average subgrain size, since (only) the large ($r_i > r^*$) subgrains act as recrystallisation nuclei.

the simulation cube is reached by the recrystallisation front coming from a nearby nucleus, i.e. the time at which it becomes recrystallised. At this time, its “growth length”, l_i , i.e. the distance the recrystallisation front has travelled from the newly recrystallised cell i towards the adjacent unrecrystallised (active) cells, is zero. At each subsequent time step, the growth length of this cell, $l_i(t)$, is calculated by

$$l_i(t) = l_i(t - \Delta t) + v_i \Delta t, \quad (7.8)$$

where $l_i(t - \Delta t)$ is the growth length of this cell i at the previous time step, v_i is the local recrystallisation-front velocity at the position of cell i and Δt is the time step length of the simulation. Next, it is determined for each active cell next to cell i whether the growth length of cell i is equal to or larger than the distance between cell i and the active cell considered, i.e. whether the recrystallisation front coming from the recrystallised cell i has reached any (unrecrystallised) active cells yet. If this is the case, the corresponding active cell, j , becomes a recrystallised cell. Then, at this moment in time, the growth length of cell j , l_j is zero and the local recrystallisation-front velocity at the position of cell j , v_j , is calculated, etc.

The *local* interface velocity, v , depends on (i) the mobility of the migrating recrystallisation front, which depends on the misorientation angle, ω , between the considered growing, recrystallised grain and the unrecrystallised subgrain into which it is growing, and (ii) on the driving force for interface migration, which is provided by the deformation-energy difference between the deformed and the recrystallised grain.

In the simulations, the stored energy of recrystallised grains is set to zero. Thus, the local driving force for recrystallisation is given by the stored energy of the (deformed) unrecrystallised subgrain considered.

In the simulations, the (misorientation-dependent) interface mobility, $M(\omega)$, is assumed to be different for low-angle grain boundaries (LAGBs; grain boundaries with misorientation angle $\omega \leq 15^\circ$), general high-angle grain boundaries (HAGBs; grain boundaries with misorientation angle $\omega > 15^\circ$) and (for copper) high-mobility high-angle grain boundaries (HMGBs; grain boundaries with misorientation angle $\omega = 40^\circ$ with $\langle 111 \rangle$ rotation axis; see footnote 23 in section 7.2). LAGBs are assumed to have a mobility which is 100 times smaller than the mobility of a general HAGB, M_{HAGB} , and the HMGBs are assumed to have a mobility 10 times larger than a general

HAGB [60,79]:

$$M(\omega) = \begin{cases} 0.01M_{\text{HAGB}} & \text{if } \omega \leq 15^\circ \text{ (LAGB),} \\ M_{\text{HAGB}} & \text{if } \omega > 15^\circ \text{ (HAGB),} \\ 10M_{\text{HAGB}} & \text{for } 40^\circ \langle 111 \rangle \text{ boundaries (HMGB).} \end{cases} \quad (7.9)$$

This simple model for grain boundary mobility is capable of capturing the main effects of variable grain-boundary mobility on the recrystallisation kinetics and the resulting microstructure (see section 7.6).

In the simulations, the mobility can (i) be set as identical for all grain boundaries (denoted " $M \neq M(\omega)$ " in Table 7.1), or (ii) can be different for LAGBs and HAGBs (first two lines of equation (7.9); denoted " $M(\omega)$ " in Table 7.1; in this case HMGBs are assumed to have the same mobility as HAGBs), or (iii) can be different for LAGBs, HAGBs and HMGBs (denoted " $M(\omega) + \text{HMGBs}$ " in Table 7.1).

7.5 Results

7.5.1 Growth kinetics: anisotropic growth due to misorientation-dependent grain-boundary mobility

In order to investigate the influence that a misorientation-dependent grain-boundary mobility has on the recrystallisation kinetics and the final microstructure, a series of simulations (denoted I-A to I-G) was performed. The employed simulation parameters have been summarised in Table 7.1. In these simulations, the nuclei were present already at the beginning of the recrystallisation (pre-existing nuclei; site saturation at $t = 0$), the parent microstructure had a narrow SGSD (cf. Figure 7.1 a) and all subgrains had the same stored (deformation) energy per unit volume.

As a reference, a simulation with constant, i.e. misorientation-*independent* grain-boundary mobility was performed first (I-A). As expected, the resulting microstructure (Figure 7.3 a) is very similar to a Voronoi tessellation (cf. the nearly straight grain-boundary segments between triple lines (triple points in the depicted cross section)) and the corresponding GAD (shown in black in Figure 7.4) is narrow and includes only few very small grain areas. After correcting for the non-negligible nucleus size (cf. section 7.4.4), the slope of the double-logarithmic plot (the JMAK-exponent; cf. section 7.1) for the recrystallised fraction equals three (see Figure 7.5 a), as expected [2,8].

Next, the mobility was made to depend on the misorientation between the growing recrystallised grains and the adjacent part of the parent mi-

Table 7.1: Simulation parameters employed in the set of simulations investigating misorientation-dependent grain-boundary mobilities, all pertaining to pre-existing nuclei. $M \neq M(\omega)$ means a simulation with misorientation-*independent* grain-boundary mobilities, $M(\omega)$ means simulations in which LAGBs have a lower mobility than HAGBs and $M(\omega)$ +HMGB means a simulation in which LAGBs have a lower mobility than HAGBs and additionally $40^\circ \langle 111 \rangle$ grain boundaries, HMGBs, have a very high mobility. In the last three columns, it is specified whether the experimentally determined distributions were used as input for the misorientation-distribution of the deformed microstructure (“def. MOD”), the orientation-distribution function of the deformed microstructure (“def. ODF”) and the orientation-distribution function of the recrystallisation nuclei (“nucl. ODF”), respectively, or whether the (mis)orientations were chosen randomly.

Simulation	Mobility	def. MOD	def. ODF	nucl. ODF
I-A	$M \neq M(\omega)$	random	random	random
I-B	$M(\omega)$	random	random	random
I-C	$M(\omega)$	exp.	random	random
I-D	$M(\omega)$	exp.	exp.	random
I-E	$M(\omega)$	exp.	exp.	exp.
I-F	$M(\omega)$	random	exp.	exp.
I-G	$M(\omega)$ +HMGBs	exp.	exp.	exp.

crostructure as described in section 7.4.4. For the simulations I-B to I-F, only LAGB (low mobility) and HAGB (100 times higher mobility) were considered. In the simulation I-G, additionally HMGB ($40^\circ \langle 111 \rangle$; highest mobility) were considered (see Table 7.1). The subgrain orientations were set up randomly in simulation I-B. In simulation I-C, they were set up in compliance with the experimentally determined MOD of the deformed copper specimen; in simulation I-F they were set up in compliance with the experimentally determined ODF of the deformed copper specimen; and in simulation I-D, -E and -G, they were set up in compliance with both the experimentally determined MOD and the experimentally determined ODF of the deformed copper specimen. For the present case of pre-existing nuclei, the orientations of the recrystallisation nuclei were chosen either randomly (I-B, -C and -D) or according to the experimentally determined ODF of the fully recrystallised copper specimen (I-E, -F and -G).

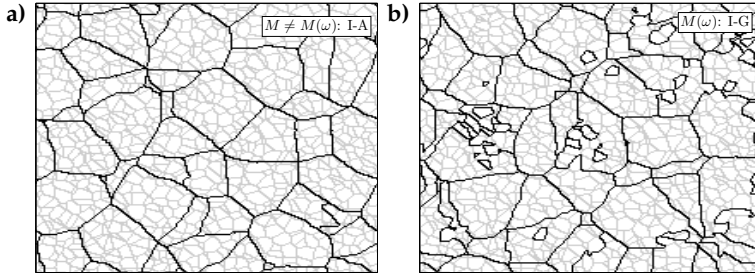


Figure 7.3: The fully recrystallised microstructures, shown as two-dimensional cross sections through the three-dimensional simulation cube, after two simulations from the set of simulations investigating the role of misorientation-dependent grain-boundary mobilities. The grain-boundaries after recrystallisation are shown in black and the original subgrain boundaries (of the deformed microstructure) are shown in grey. a) For a simulation with constant, misorientation-independent grain-boundary mobilities and b) for a simulation with misorientation-dependent grain-boundary mobilities incorporating the experimentally obtained ODF and the experimentally obtained MOD of the deformed state and using the experimentally obtained ODF of the recrystallisation nuclei.

The MOD of the subgrains in the deformed state is shown in Figure 7.6. For the simulations I-C and I-G (Figures 7.6 a) and c), respectively), the MOD was made equal to the experimentally determined MOD (cf. section 7.4.1). For simulation I-F, where compatibility with only the experimentally determined ODF of the deformed microstructure was assumed, the resulting MOD of the subgrain microstructure shows a very small deviation from the Mackenzie distribution, which is the MOD expected for randomly oriented material with cubic crystal symmetry [109]. For the simulations I-A and I-B (not shown in Figure 7.6), in which compatibility with neither the experimentally observed ODF nor the experimentally observed MOD was imposed, the MOD of the subgrain microstructure is equal to the Mackenzie distribution, as expected.

The simulations demonstrate that the kinetics of the recrystallisation are not influenced significantly by the misorientation-dependent mobility (see Figure 7.5 a): All simulations lead to a straight line with slope three in the

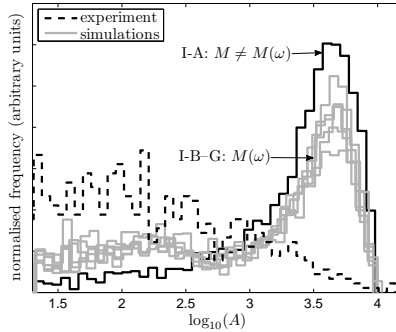


Figure 7.4: The resulting (logarithmic) grain-area distributions for the set of simulations investigating misorientation-dependent mobilities (simulations I-B to I-G). The result of the reference simulation (i.e. with constant, misorientation-*independent* grain-boundary mobilities; I-A) is shown in black and the experimentally obtained GAD of cold rolled and recrystallised copper [118] is shown with a dashed line.

double-logarithmic plot. Therefore, the deviation from straight-line behaviour observed experimentally cannot be ascribed to the misorientation dependence of the grain-boundary mobility and thus not to anisotropic growth.

For the case of a misorientation-dependent grain-boundary mobility, the number of recrystallised grains per unit area as function of the recrystallised fraction (Figure 7.5 b) shows a slightly different course than for the case of a misorientation-*independent* grain-boundary mobility (involving isotropic growth; cf. the reference simulation I-A): the rate at which recrystallising grains become visible in a cross section increases towards the end of the recrystallisation for the cases of misorientation-dependent grain-boundary mobilities. This phenomenon generally agrees with the experimental observation; however, the simulated and experimental curves do not agree well in the beginning stage of the recrystallisation.

Although the GAD after completed recrystallisation shows an increased relative amount of small grains in case of a misorientation-dependent grain-boundary mobility, as holds much stronger for the experimental result, the main part of the GAD is similar to the GAD for the case of a misorientation-independent grain-boundary mobility, in striking disagreement with the ex-

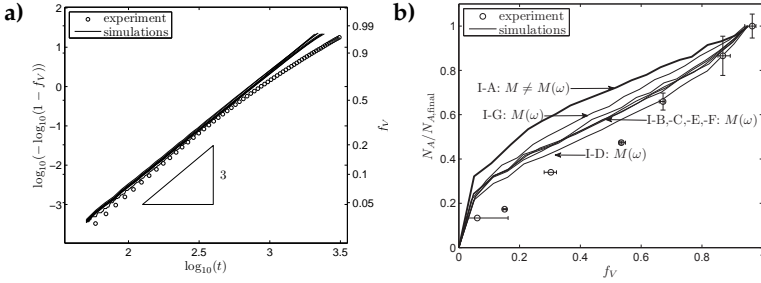


Figure 7.5: Kinetic results for the set of simulations investigating misorientation-dependent grain-boundary mobilities. a) The simulated kinetics (lines) shown as double-logarithmic plots (JMAK-plots) together with experimental results (symbols) and b) the normalised number of recrystallised grains per unit area observable in a two-dimensional cross-section through the three dimensional simulation cube as function of the recrystallised volume fraction (lines) together with experimental results (symbols). The result of the reference simulation (i.e. pertaining to a constant, misorientation-*in*dependent grain-boundary mobility; I-A) is shown in black.

perimental result (see Figure 7.4). Comparing the microstructure obtained from the reference simulation (I-A, Figure 7.3a) with a simulation with misorientation-dependent mobility (I-G, Figure 7.3b), it is clear that in the latter case there are numerous small grains or protrusions on the grain boundaries of larger grains, mostly only as large as one subgrain in the deformed state. These former subgrains have/had a small misorientation angle with the surrounding grains and were therefore not swept by the recrystallisation front, but left unrecrystallised. They were either recrystallised later by another grain (leading to protrusions along grain boundaries) or remained unrecrystallised even at the end of the simulation (leading to small, independent grains). This explains the increased relative amount of small grains in the GADs obtained for misorientation-dependent grain-boundary mobilities as compared to the case of a misorientation-independent grain-boundary mobility. The extent of such frequency increase at small grain areas in the GAD depends on the orientations of the subgrains and the recrystallised grains (i.e. their ODFs) as well as on their spatial arrangement.

From the results and their above discussion it can be concluded that as-

signing, in the simulation, orientations to the subgrains in the deformed state and the recrystallising grains according to the experimentally observed ODF and MOD for the deformed state and the ODF for the recrystallised state does not suffice to generate by simulation a deformed microstructure which, upon recrystallisation with a misorientation-dependent mobility, leads to a recrystallised microstructure compatible with the experimental observation.

The misorientation distributions of the microstructures in the deformed state (i.e. pertaining to the misorientation angle between adjacent subgrains *before* the recrystallisation simulation) and in the fully recrystallised state (i.e. pertaining to the misorientation angle between adjacent recrystallised grains *after* the recrystallisation simulation) are shown in Figure 7.6 for three example simulations. Additionally, the distribution of the misorientation angle between recrystallised grains and adjacent deformed subgrains during recrystallisation is shown. This MOD was calculated for all pairs of deformed subgrains and adjacent recrystallised grains which occurred *during* the simulation, i.e. at all stages during recrystallisation. This latter MOD reflects the distribution of local interface mobilities occurring during the simulated recrystallisation. For none of the performed simulations, this MOD (representing an average for the entire recrystallisation process) deviates strongly from a random (Mackenzie) distribution: neither a relatively large number of low-mobility grain boundaries (LAGBs) nor a relatively large number of high-mobility grain boundaries (HMGBs) is formed during recrystallisation (but see next paragraph). As a consequence, the recrystallisation kinetics does not differ from the reference simulation (isotropic growth).

Interestingly, the MOD of the fully recrystallised microstructure is not fully identical to the Mackenzie distribution if the experimentally observed ODF for the recrystallisation nuclei/grains is adopted in the simulations (see Figures 7.6 b) and c); simulations I-F and I-G), but rather shows a relatively high number of LAGBs and also a relatively high number of grain boundaries with misorientation angle $\omega > 50^\circ$ (see, especially, Figure 7.6 b)). This is different from the experimental results, where the MOD for the fully recrystallised specimens is almost perfectly identical to the Mackenzie distribution [118].

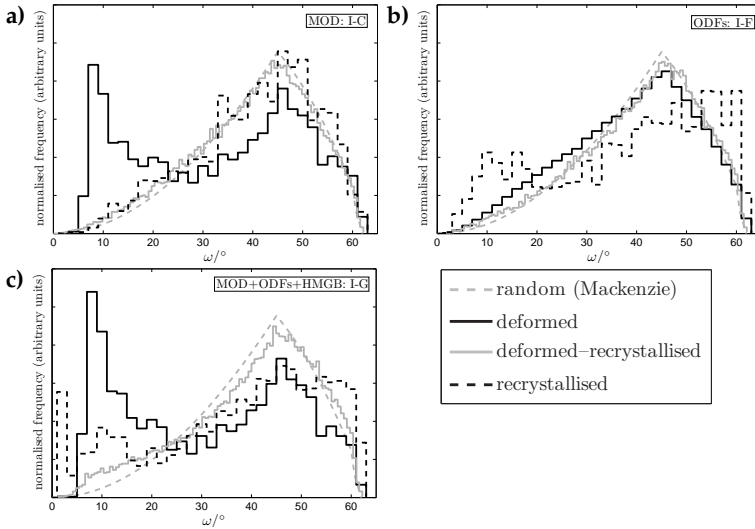


Figure 7.6: The misorientation distributions of the simulated microstructures in the deformed state (i.e. pertaining to the misorientation angle between adjacent subgrains *before* the recrystallisation simulation: black, solid lines), in the fully recrystallised state (i.e. pertaining to the misorientation angle between adjacent recrystallised grains *after* the recrystallisation simulation: black, dashed line) and between adjacent recrystallised grains and the deformed subgrains during recrystallisation (i.e. pertaining to the misorientation angle between adjacent unrecrystallised subgrains and recrystallised grains *during* the recrystallisation simulation (see text): grey, solid line). For comparison, the Mackenzie distribution for randomly oriented cubes is shown as well (grey, dashed line). a) For a simulation incorporating (only) the experimentally obtained MOD of deformed subgrains, b) incorporating the experimentally obtained ODFs for the deformed subgrains and the recrystallised grains and c) incorporating the MOD of deformed subgrains and both ODFs in a simulation including high-mobility grain boundaries.

7.5.2 Influence of the subgrain-size distribution, the subgrain-energy distribution and the nucleation model

In order to investigate the effect of ongoing nucleation on the GAD as observed after recrystallisation, a set of simulations with two different nucleation modes was carried out: Firstly, simulations were performed with pre-existing nuclei (subgrain-growth constant $k = 0$; cf. sec. 7.3.1)) and, secondly, with ongoing nucleation (subgrain-growth constant $k > 0$). In the case of ongoing nucleation, the subgrain-growth constant, k , was chosen high enough to induce a clear difference with the results of simulations without ongoing nucleation, but small enough to assure that the recrystallisation proceeded predominantly by growth of recrystallised grains and not by nucleation of new grains.

The rate at which subgrains become recrystallisation nuclei not only depends on the kinetics of subgrain coarsening, but also on the subgrain-size distribution (SGSD). Therefore, two different SGSDs were employed; a narrow one and a broad one (see Figure 7.1 a).

Ongoing nucleation is expected to lead to a JMAK-exponent larger than (the experimentally observed value of) three (see [2, 8] and section 7.2). Then, to realise a decreasing growth rate for individual recrystallising grains as recrystallisation proceeds, as observed experimentally (see section 7.3.2), a mechanism is needed to slow down the growth rate as the recrystallisation proceeds. For this purpose, a distribution of subgrain (deformation) energies per unit volume was introduced (see section 7.4.1). For comparison, also simulations with a homogeneous (deformation) energy in all subgrains were performed.

The employed parameters for all simulations, coded II-A to II-L, have been gathered in Table 7.2. In all simulations, the grain-boundary mobilities were taken as misorientation-independent. The simulations II-A and II-G (both pertaining to cases of pre-existing nuclei and a uniform SGED, but different SGSDs) serve as reference simulations. Identical results for the recrystallisation kinetics and the resulting microstructure are obtained for both cases, since for the case of pre-existing nuclei and a uniform SGED, the SGSD does not influence the outcome of the simulation.

The double-logarithmic plots for simulations pertaining to a narrow and a broad SGSD are presented in Figures 7.7 a) and b), respectively. Except for the two reference simulations, II-A and -G, all simulations led to curves with a slope *larger* than three. The slope is larger for simulations with ongoing nucleation (II-B, -D, -F and II-H, -J, -L) than for simulations with pre-existing nuclei (II-C, -E and II-I, K), as expected (see section 7.2). However,

Table 7.2: Simulation parameters employed in the set of simulations investigating the effects of subgrain-energy distributions and ongoing nucleation. "SGSD" denotes the employed subgrain-size distribution (see Figure 7.1 a), "SGED" denotes the employed subgrain-energy distribution (none, gaussian distribution or subgrain energy proportional to the subgrain surface area, see Figure 7.1 b) and "SG coarsening" denotes the nucleation model ($k = 0$: pre-existing nuclei, $k > 0$: ongoing nucleation).

Simulation	SGSD	SGED	SG coarsening
II-A	narrow	$G = \text{const.}$	$k = 0$
II-B	narrow	$G = \text{const.}$	$k > 0$
II-C	narrow	gaussian	$k = 0$
II-D	narrow	gaussian	$k > 0$
II-E	narrow	$G \propto O$	$k = 0$
II-F	narrow	$G \propto O$	$k > 0$
II-G	broad	$G = \text{const.}$	$k = 0$
II-H	broad	$G = \text{const.}$	$k > 0$
II-I	broad	gaussian	$k = 0$
II-J	broad	gaussian	$k > 0$
II-K	broad	$G \propto O$	$k = 0$
II-L	broad	$G \propto O$	$k > 0$

a decrease of the slope upon continued recrystallisation, as observed experimentally, is not revealed by any of the simulations.

Note that for these plots, the fraction of released energy was used to determine a value for f , denoted by f_H , instead of the recrystallised volume fraction, which leads to a value for f denoted by f_V . The two quantities are not identical for simulations involving a distribution of subgrain (deformation) energies. For the determination of the degree of transformation (fraction recrystallised), the fraction of released enthalpy was used since this quantity is measured in the calorimetric experiments used for comparison. In the experiments (see section 7.2), the results for f_V and f_H are identical within experimental accuracy. This imposes a limit on the width of the SGED which can be employed in the simulations: If the SGED becomes very broad, f_V and f_H differ strongly and the simulations cannot be reconciled with the experimental results.

The number of recrystallised grains is plotted in Figure 7.8 as function of the recrystallised fraction. All simulations start with (approximately)

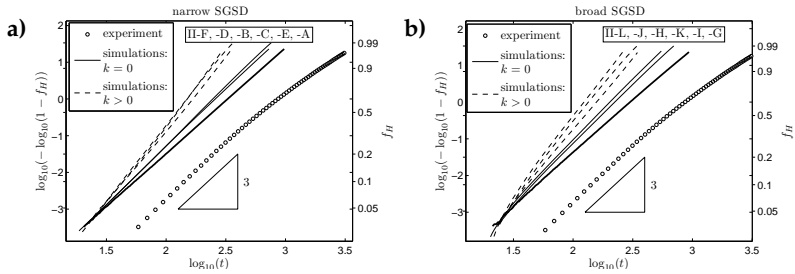


Figure 7.7: The results of the set of simulations investigating the effects of SGEDs and ongoing nucleation. The simulated kinetics (lines) are shown as double-logarithmic plots together with experimental results (symbols). The fraction of the released heat was used to produce the plots and the curves were shifted horizontally to facilitate comparison. a) The results of simulations employing a narrow SGSD and b) the results of simulations employing a broad, skewed SGSD.

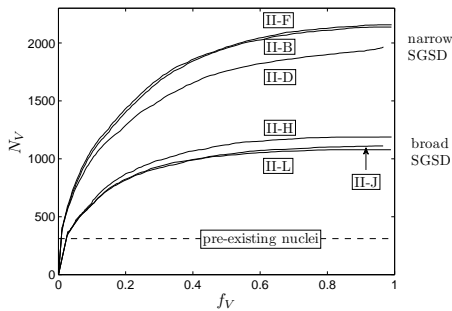


Figure 7.8: The number of recrystallisation nuclei in simulations with ongoing nucleation as a function of the recrystallised volume fraction. For comparison, the number of nuclei in simulations pertaining to pre-existing nuclei is shown as dashed line.

the same number of pre-existing nuclei. For simulations pertaining to pre-existing nuclei, the number of nuclei remains constant during the recrystallisation, whereas it increases for simulations pertaining to ongoing nucleation. Despite identical subgrain coarsening kinetics, the nucleation rate is different for simulations using a narrow and a broad SGSD. This is expected, since subgrain coarsening, leading to more and more subgrains becoming larger than the critical subgrain radius/size, leads to different numbers of new (i.e. additional) nuclei for different SGSDs (cf. Figure 7.1 a). (Note that in the simulations, ongoing nucleation is realised by a reduction of the critical subgrain size; cf. section 7.4.3).

The influence of the SGED on the number of recrystallising grains is much less pronounced than the influence of the SGSD (cf. Figure 7.8 and Table 7.2). In the present simulations, the SGED does not influence the subgrain coarsening kinetics and hence it could be expected that the nucleation rate should be entirely independent of the SGED. However, since the SGED does influence the driving force of the recrystallisation and hence the growth rate of recrystallising grains, it exerts a modest influence on the number of recrystallising grains: if recrystallisation is slow, subgrain coarsening remains significant and therefore more nuclei can emerge before recrystallisation is completed than if recrystallisation is fast.

The difference between the simulations is not very pronounced if the normalised number of recrystallised grains observable in a cross section, $N_A/N_{A,final}$, is considered (see Figure 7.9). The simulations pertaining to ongoing nucleation (Figure 7.9 b) are slightly more similar to the experimental observations than the simulations pertaining to pre-existing nuclei (Figure 7.9 a). However, for both nucleation modes, the simulated results in case of inhomogeneously distributed deformation energy (especially simulation II-C, -I, -K, -D, -J and -L) deviate more from the experimental values than the results of the simulations with the same deformation energy for all subgrains (II-A, -G, -B and -H). The simulations in which the subgrain energy is proportional to the subgrain surface area (II-K and -L) show the strongest difference with the reference simulations and the experimental results.

For these latter cases, where the subgrain energy is proportional to the subgrain surface area (II-K and -L), the number of grains visible in a cross section even decreases slightly towards the very end of the recrystallisation, a behaviour which is opposite to the experimentally observed marked *increase* towards the end of the recrystallisation. This decrease of the number of visible grains at the completion of recrystallisation in simulations II-K and II-l can be understood as follows. In a partially recrystallised micro-

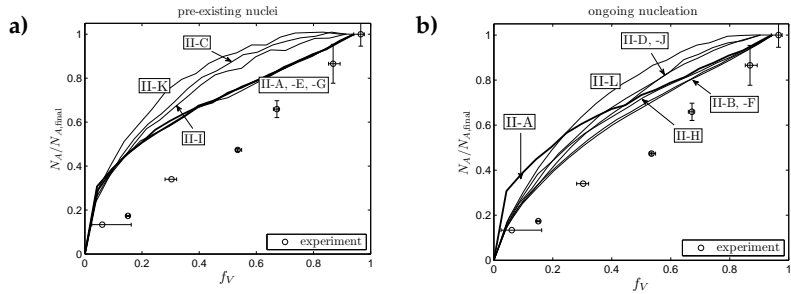


Figure 7.9: The normalised number of recrystallised grains per unit area observable in a two-dimensional cross-section through the three dimensional simulation cube as function of the recrystallised volume fraction (lines) for the set of simulations investigating SGEDs and the nucleation mode. For comparison, experimental results (symbols) are shown as well. The results of the reference simulations (cf. Table 7.2) are shown in black. a) Simulations pertaining to pre-existing nuclei and b) simulations pertaining to ongoing nucleation.

structure, the irregular shape of some grains leads to the observation of several grains in a two dimensional cross section, which are only seemingly separate grains, i.e. which are in reality connected underneath/above the cross-sectional plane. During the final stage of the recrystallisation, the grain shapes become less irregular and thus the phenomenon described causes the observed number of grains in a cross section to decrease. The corresponding microstructure after completed recrystallisation (II-J; see Figure 7.11 d) shows many curved grain boundaries, but not many grains which are only seemingly separate grains, which would be presented as relatively small grains in the GAD of the fully recrystallised simulated microstructure.

The GADs after completed recrystallisation are shown in Figure 7.10. All simulations pertaining to pre-existing nuclei lead to very similar GADs, showing a bimodal shape as observed also for the simulations described in the previous section (Figure 7.4). The SGSD and the SGED do not have a strong influence on the shape of the GADs. Simulations pertaining to ongoing nucleation obviously lead to a larger number of recrystallised grains and hence to a lower average grain area. The main peak of the GAD is not

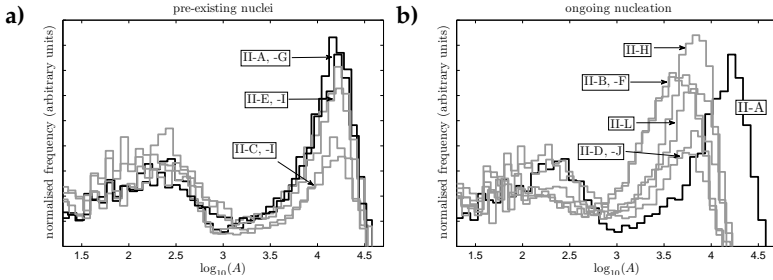


Figure 7.10: The (logarithmic) grain-area distributions after completed recrystallisation for the set of simulations investigating SGEDs and the nucleation mode. The results of the reference simulations (see Figure 7.9) are shown in black. a) Simulations pertaining to pre-existing nuclei and b) simulations pertaining to ongoing nucleation.

significantly broadened.

Yet, despite the similarity of the GADs, the corresponding microstructures are quite different in appearance. Five example microstructures are shown in Figure 7.11 together with the experimentally determined one. The difference in the resulting microstructures for the cases of pre-existing grains and ongoing nucleation can be observed by comparing Figure 7.11 c) and Figure 7.11 d). The grains produced by the simulation pertaining to ongoing nucleation are overall much smaller than the grains produced by the simulation pertaining to pre-existing nuclei.

The simulations with non-uniform subgrain energy (Figures 7.11 b) to e)) lead to microstructures with small grains inside recrystallised grains, whereas for the reference simulation with a uniform subgrain energy (Figure 7.11 a), small grains can only be seen in between recrystallised grains (in space which was still unrecrystallised at the end of the simulation; marked by arrows in the figure). These small grains inside larger, recrystallised grains are (parts of) unrecrystallised subgrains which have only a very low (deformation) energy and hence offer almost no driving force for recrystallisation.

The SGSD does not have a strong influence on the appearance of the microstructures (cf. Figures 7.11 b) and c)).

In particular the grain boundaries produced by the simulations with non-uniform subgrain energy are somewhat curved (Figures 7.11 b) to e)), whereas

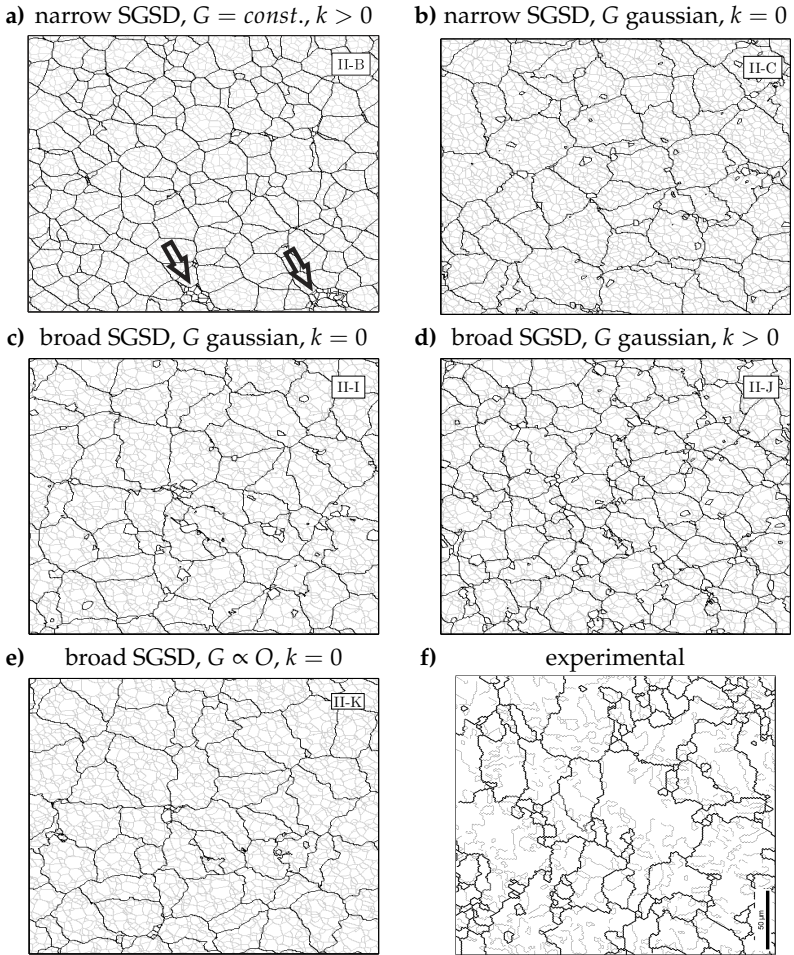


Figure 7.11: a)–e) The fully recrystallised microstructures for some simulations from the set of simulations investigating SGEDs and ongoing nucleation. The grain-boundaries after recrystallisation are shown in black and the original subgrain boundaries (of the deformed microstructure) are shown in grey. The simulation parameters have been indicated above the panels and the simulation number (see Table 7.2) have been indicated in the panels. f) Experimental result for recrystallised pure copper [118]. General HAGB are shown in black and twin grain boundaries are shown in grey.

the grain boundaries resulting from simulations with uniform subgrain energy are more or less flat (Figure 7.11 a). However, compared with the experimentally determined microstructure (Figure 7.11 f), the shape of the grains in the simulated microstructures pertaining to non-uniform subgrain energies is more regular.

7.6 Concluding Discussion

None of the simulations performed in this study produced a microstructure compatible with experimental results for severely deformed copper. Some simulations led to microstructures composed of grains with curved grain boundaries similar in appearance to experimentally observed grains, but the simulations did not produce the monomodal, broad GAD as observed experimentally. Instead, bimodal GADs resulted (see Figures 7.4 and 7.10).

Since the subgrains in the initial, deformed microstructure are much smaller than most grains in the final, recrystallised microstructure, one recrystallising grain sweeps through many subgrains in the course of the recrystallisation. Therefore, a migrating grain boundary (recrystallisation front) will be subjected to many, successive misorientations. If, for example, a subgrain with small misorientation with respect to the growing grain is encountered, the interface mobility is reduced at only the corresponding, small portion of the moving recrystallisation front. The grain will grow around the unfavourably oriented subgrain and a small, as yet unrecrystallised grain is left behind in the wake of the recrystallisation front. This leads to the observed bimodal nature of the GAD and not to a monomodal, broad GAD.

Also the experimentally determined kinetics could not be reproduced. Instead of a JMAK-exponent decreasing with progressing recrystallisation, the simulations showed either a constant or an increasing JMAK-exponent (cf. Figures 7.5 and 7.7). Neither (i) a misorientation-dependent interface mobility, nor (ii) a SGED did lead to a slowing down of the average growth rate towards the end of the recrystallisation, as is experimentally observed [118]:

Ad (i) The misorientation dependency of the grain-boundary mobilities has an only small impact on both recrystallisation kinetics and microstructure, because there are only few LAGBs and HMGBs, as compared to the dominating HAGBs, present between growing recrystallising grains and the deformed matrix during the simulated recrystallisation (only approximately 6% of all boundaries are LAGBs, cf. Figure 7.6). Even if a recrystal-

lised, growing grain encounters a subgrain of the deformed microstructure with which it has such a special orientation relationship (leading either to a very low (LAGB) or a very high (HMGB) grain-boundary mobility), this orientation relationship, and thus its effect on the recrystallisation kinetics, is lost once the recrystallising grain has grown around (low mobility LAGB) or has swept through (high mobility HMGB) the subgrain concerned.

Ad (ii) The influence of a distribution of subgrain (deformation) energy on the recrystallisation kinetics is not very strong. It was expected that the subgrains with the highest energy would recrystallise first, thereby reducing the average (deformation) energy of the not yet recrystallised subgrains, which would cause a decrease of the recrystallisation rate towards the end of the recrystallisation. It may be suggested that this phenomenon could not manifest itself due to the spatially random distribution of the subgrain-deformation energies. Making the SGED broader would increase its effect on the recrystallisation kinetics. However, in this case, a marked discrepancy between the two measures for the recrystallised fraction, f_V and f_H should occur (cf. the discussion in section 7.5.2), which was not observed experimentally.

As the grain-boundary migration rate is proportional to both the mobility and the driving force (cf. section 7.3.2), a similar discussion as given above for the effect of a misorientation distribution on the GAD can be given for the effect of a SGED on the GAD: the sizes of subgrains and recrystallised grains are very different and thus, if a low-energy subgrain is encountered by a growing recrystallised grain, the as yet unre-crystallised subgrain is left behind in the wake of the recrystallisation front. Thus the presence of a SGED yields a bimodal GAD as well.

The experimentally observed, broad GAD after completed recrystallisation could possibly be better reproduced by simulations departing from a subgrain structure with a very broad size distribution, including grains in the deformed state which are larger than the smallest grains in the recrystallised state (cf. the experimental results shown in Figure 7.2 c and the discussion above). Such simulations are the subject of future work.

Alternatively, ongoing nucleation could in principle produce such broad GADs. Indeed, the simulations with ongoing nucleation did show a broader GAD than the ones pertaining to pre-existing nuclei. A broad GAD with few large and many small grains (as experimentally observed) is obtained if a large number of nuclei is generated at the end of the process (i.e. if

the nucleation rate *accelerates* during the recrystallisation). With the current nucleation model, this situation could not be attained, since the subgrain-coarsening rate, which governs the nucleation rate, *decreases* with time. Moreover, the JMAK-exponent of the simulations pertaining to ongoing nucleation is higher than the experimentally observed ones: Models with a nucleation rate increasing during the recrystallisation will likely produce an even higher JMAK-exponent which may even increase with progressing recrystallisation, contrary to experimental observation.

The inadequacy of the models used in the simulations to reproduce *both* the experimentally observed kinetics and the experimentally observed microstructure implies that more detailed knowledge of the initial deformed microstructure is required. In the present article, the parent microstructure was taken into account by making the simulated subgrain structure in the initial, deformed state compatible with the experimentally obtained ODF and MOD and by assigning a certain SGSD and SGED. For future work it is therefore suggested to measure, spatially resolved, the crystal orientations and stored energies of an entire deformed specimen with a technique such as three-dimensional EBSD and to use this information as start configuration for recrystallisation simulations; thereby taking into account not only the size and orientation distributions of subgrains, *but also their spatial arrangement*.

7.7 Conclusions

Departing from an initial, deformed microstructure generated by geometric simulation, the kinetics and the resulting microstructure of the recrystallisation of pure copper have been simulated using a cellular automaton. The simulation results have been compared with previously published experimental data for strongly deformed, cold-rolled copper. The simulation procedure used in this work conceives the initial microstructure as an agglomerate of subgrains/cells, whose orientation and (partial information on their) spatial arrangement were determined according to the experimentally determined orientation-distribution function and/or the experimentally determined misorientation-angle distribution.

- When the grain-boundary mobilities in the simulation are made to depend on the misorientation, a higher number of small grains in the fully recrystallised microstructure results as compared to simulations with misorientation-independent grain-boundary mobilities. However, the occurrence of misorientation-dependent grain-boundary mo-

bilities does not influence the recrystallisation kinetics significantly. The grain-area distribution becomes bimodal with many small grain areas corresponding to (the size of) former subgrains left behind because of a low angle of misorientation with the local recrystallisation front, and many larger grain areas corresponding to the size of recrystallised grains as obtained in simulations with misorientation-independent grain-boundary mobilities.

- The introduction of an inhomogeneously distributed deformation energy, by varying the subgrain-size distribution and the subgrain-energy distribution as employed in the setup of the initial microstructure, also (see above) leads to a higher, as compared to simulations with a homogeneous deformation energy, number of small grains left behind because of their (locally) low deformation energy, thereby inducing a bimodal grain-area distribution, and to curved grain boundaries in the fully recrystallised microstructure. The recrystallisation kinetics is not significantly influenced.
- Ongoing nucleation increases the JMAK-exponent determined from the recrystallisation kinetics to a value larger than three, but did not significantly influence the fully recrystallised microstructure.
- The simulations could not reproduce the experimentally observed kinetics, i.e. a JMAK-exponent of initial value three which decreases towards the end of the recrystallisation. The simulated JMAK-exponent is either equal to three for the entire process (for simulations pertaining to misorientation-dependent mobilities) or becomes even larger than three (for simulations pertaining to ongoing nucleation).
- To realise matching of the simulated and measured microstructures, employing, in particular, a broad, preferably experimentally determined subgrain-size distribution appears imperative for the setup of the initial, deformed microstructure. Additionally, informations about the ODF, MOD and the stored-energy distribution in the deformed microstructure should be taken into account.

Chapter 8

Kinetics of the allotropic hcp-fcc phase transformation in cobalt

8.1 Introduction

Pure cobalt exhibits an allotropic phase transformation at the equilibrium temperature T_0 (at constant pressure) with the hcp modification as low temperature phase and the fcc modification as high temperature phase. This allotropic transformation shows characteristics of a martensitic transformation [126, 127]: the transformation needs no diffusion and composition change, has a distinct athermal nucleation nature leading to spontaneous initiation of the reaction upon reaching the “martensite” start temperature M_S upon cooling or the “austenite” start temperature A_S upon heating.

Many studies on the mechanism and microstructural evolution associated with the allotropic phase transformation in Co have been performed (e.g. see Refs. [126, 128]), providing controversial or inconclusive results on a number of aspects: The equilibrium temperature and its uncertainty as given in Ref. 4, $T_0 = 690 \pm 7$ K (at 1 atm), covers the range of most of the available literature data [127, 129–131], based on calculations or determined experimentally, taken as average of the “austenite” and “martensite” start temperatures, measured by X ray diffractometry, magnetometry, dilatometry or calorimetry. Values for the martensite start temperature M_S range from 692 K to 661 K and for the austenite start temperature A_S range from 694 K to 720 K [127, 132, 133]. The difference between the start temperatures for the fcc→hcp transformation (M_S temperature) and the hcp→fcc transformation (A_S temperature) is called (here) “temperature hysteresis”. Values for the enthalpy of transformation, $\Delta H_{hcp \rightleftharpoons fcc}$, range from 377 to 464 J mol⁻¹ [126, 127, 129–131] and some studies indicate differences upon heating and cooling [133, 134]. The diversity of these results appears to depend on the specimen shape (thin layer [128, 135, 136], powder [137–139], sheet [133, 134, 140, 141] and rod [126, 132, 137, 138]), the specimen size [133, 134], the state of stress [132, 139] and the (type of) thermal treatment [126, 132–135, 137–140, 142].

It appears that depending on the initial microstructure and experimental

conditions (as heating/cooling rate) a significant number of hcp \leftrightarrow fcc transformation cycles must be passed through in order to establish reproducible characteristics of the hcp \rightleftharpoons fcc transformation (see Refs. [126, 127, 133, 134, 138, 143] and, in particular, results of this study presented in section 8.4). This may contribute to the discrepancies apparent from the literature cited above.

A full, quantitative, description of the kinetics of the allotropic transformation in Co was not presented until now. The present work for the first time provides such a model description of the allotropic, martensitic transformation kinetics of Co, departing from a general modular model of phase transformation kinetics composed of separate modes of nucleation, growth and impingement [8, 144], thereby incorporating an athermal nucleation mode as proposed in Ref. [143], interface controlled growth and anisotropic impingement. This approach was recently applied successfully by our group to the polymorphic transformation of Laves phases [145].

The present chapter focuses on the hcp \rightarrow fcc phase transformation using “stabilized” specimens (i.e. after a number of preceding transformation cycles). Isochronal annealing experiments in a fixed temperature range using Differential Scanning Calorimetry, DSC, were performed. The resulting enthalpy changes as function of time and heating rate were interpreted quantitatively using the modular phase transformation model.

8.2 Theoretical Background of Transformation Kinetics

Solid state phase transformations can take place as soon as the hitherto existing phase is not stable anymore; i.e. a thermodynamic driving force can be indicated. Such a phase transformation can be realized in different ways. In general a phase transformation can be subdivided into three (overlapping) steps: nucleation, growth and impingement. This type of modular approach has been described in [144, 146] (see, especially, the review in Ref. [8]) and has been applied successfully to a variety of phase transformations: crystallization of amorphous metal alloys [31, 147–151], the austenite-ferrite transformation in Fe-based alloys [152–154] and the polytypic transformations of Laves phases [145].

Assuming, hypothetically, that each individual product particle, emanating from a successful nucleation process, grows into an infinitely large parent phase, in the absence of other product particles, the so-called extended volume, V_e , given by the sum of the volumes of all these (hypothetical) particles, can be calculated. In a second step the extended transformed frac-

tion, $x_e (= V_e/V_S$; with V_S as the volume of the specimen), has to be corrected for (hard) impingement to obtain the real transformed fraction, f , by adopting a certain impingement mode. In the following, after discussing the $\text{hcp} \rightleftharpoons \text{fcc}$ transformation mechanism, nucleation, growth and impingement modes relevant for the $\text{hcp} \leftrightarrow \text{fcc}$ transformation are indicated briefly.

8.2.1 The $\text{hcp} \rightleftharpoons \text{fcc}$ Transformation Mechanism

The dislocation (line) energy of a so called perfect dislocation can be reduced by dissociation into two Shockley partial dislocations inducing a stacking fault (SF) in between both partials, with the stacking fault energy (SFE) σ . The width of the dissociated partial dislocations is given by the balance of the elastic repulsion force, forcing the dissociation, and the stacking fault energy, σ , opposing the dissociation: dissociated (perfect) dislocations are a basic component of the microstructure [155].

The transformation of an fcc (ABCABC... stacking sequence) into an hcp (ABABAB... stacking sequence) crystal structure, and vice versa, can be realized by the motion of Shockley partial (SP) dislocations, with Burgers vectors, of type $1/6\langle 11\bar{2} \rangle$, on every second closest packed plane [135,143].

This process can be called “ordered glide” as an ordered array of Shockley partials is required for the phase transformation. So this ordered array of x partials transforms a region of thickness $2x$ closest packed layers. The transformation $\text{fcc} \rightarrow \text{hcp}$ occurs by dissociation of the perfect dislocations and the transformation $\text{hcp} \rightarrow \text{fcc}$ by association of the SPs (see Figure 8.1). Studies of the microstructural evolution upon thermal (transformation) cycling showed that such ordered dislocation arrangements evolve indeed [135], establishing, by the “back and forth” movement of the same partial dislocations, the reversible $\text{hcp} \rightleftharpoons \text{fcc}$ transformation with preservation of the orientation, in the specimen frame of reference, of the hcp and fcc crystals, as validated for Co [126].

Each SP can be associated with one of six Burgers vectors of type $1/6\langle 11\bar{2} \rangle$ on a closest packed plane leading, upon glide of the SP, to a microscopic shear of the lattice (see top part in Figure 8.2). This shear can be nullified (no add up of microscopic to macroscopic shear) by the summation of a set of three successive dislocations in the ordered array of SPs, with Burgers vectors such that $\vec{b}_1 + \vec{b}_2 + \vec{b}_3 = 0$ (see bottom left part in Figure 8.2). If $\vec{b}_1 + \vec{b}_2 + \vec{b}_3 \neq 0$, macroscopic shear evolves³² (see bottom right part in

³²Note that for polymorphic Laves phase transformations such macroscopic shear is impossible because of the glide of synchro Shockley partial dislocation dipoles [145].

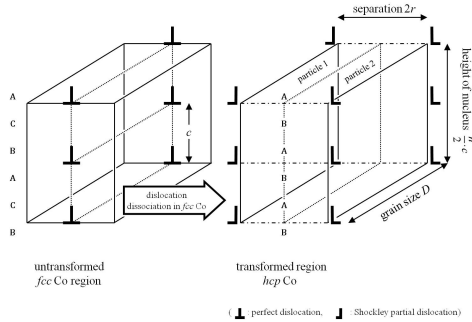


Figure 8.1: Schematic view of an hcp nucleus (ABABAB... stacking sequence) developing in an fcc matrix (ABCABC... stacking sequence) by dissociation of three perfect dislocations in fcc. Left: Array of three perfect dislocations in the fcc Co phase (before dissociation); right: two arrays each consisting of three Shockley partial dislocations; the two arrays build up two particles consisting of the hcp phase, each particle having a volume determined by the grain size D , the height of the defect structure (depending on the number of Shockley partial dislocations within the array) and half of the separation distance, $2r$, realised by glide of the Shockley partial dislocations.

8.2 Theoretical Background of Transformation Kinetics

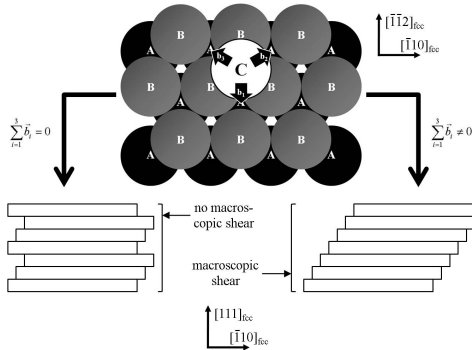


Figure 8.2: Stacking sequence of an fcc crystal lattice (top). The black arrows indicate possible Burgers vectors available for the glide process of Shockley partial dislocations upon the fcc→hcp transformation. Bottom left: Burgers vectors of Shockley partial dislocations in every second closest packed plane oriented such that for three successive Shockley partials (i.e. comprising a stack of six closest packed planes) . No macroscopic shear occurs. Bottom right: Shockley partial dislocations, gliding on every second closest packed plane with the same Burgers vector. This leads to macroscopic shear.

Figure 8.2 where the extreme case, all SPs have same \vec{b} , is shown). However, it is usually assumed [141, 156] that microscopic shear cancels out over short distances and therefore the contribution of macroscopic shear to the phase transformation (kinetics) is considered to be negligible here.

Irrespective of the micro-/macroscopic shear discussed above, the allotropic transformation in cobalt is associated with a macroscopic distortion due to the change of the atomic distances. This macroscopic distortion for the fcc→hcp transformation is +0.021% parallel to and 0.242% perpendicular to the closest packed plane [141].

The hcp crystal lattice has only one closest packed set of $\{0001\}$ planes; the fcc crystal lattice has four equivalent sets of closest packed $\{111\}$ planes. Upon thermal cycling the dislocation structure is (re)arranged, from any initial state, such, that only one single set of $\{111\}_{fcc}$ planes is active and parallel to $\{0001\}_{hcp}$ (further see section 8.6.1).

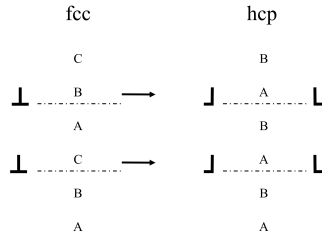


Figure 8.3: Ordered arrays of Shockley partial dislocations gliding through an fcc Co crystal leaving behind the hcp Co structure (see also Figure 8.1).

8.2.2 Nucleation

The thermodynamic model for nucleation must be compatible with the mechanism for the $\text{hcp} \rightleftharpoons \text{fcc}$ transformation by glide of an ordered array of Shockley partial dislocations (cf. section 8.2.1). The model presented here is derived from an earlier description of nucleation of the martensitic $\text{fcc} \rightarrow \text{hcp}$ transformation in metals by dissociation of perfect dislocations [143].

Consider the periodically arranged array of perfect dislocations in an fcc crystal as shown in Figure 8.1 and Figure 8.3. The $\text{fcc} \rightleftharpoons \text{hcp}$ phase transformation is performed by glide of the periodically arranged Shockley partial dislocations through the crystal lattice (see section 8.2.1)

Initiation of an $\text{fcc} \rightarrow \text{hcp}$ transformation requires dissociation of the array of perfect dislocations into two arrays of Shockley partial dislocations. The region in between these two arrays can be described as a stacking faulted region (with reference to the parent structure) or as transformed region (exhibiting the product, hcp crystal structure). As long as fcc is the stable phase, the dissociation is limited by the relatively high energy (with reference to the parent phase) of the faulted structure lying between the two arrays of Shockley partial dislocations. This is no longer the case if the hcp phase becomes the stable phase, i.e. by passing the hcp-fcc phase equilibrium temperature T_0 upon (isochronal) cooling from the fcc phase field.

The region between the two separated arrays of Shockley partial dislocations can be considered as two second-phase (hcp) particles each having the volume V and the interfacial area S . The total Gibbs energy change ΔG associated with the formation of this second phase particle can be given as:

$$\Delta G = V(\Delta G_V^{ch} + E_V^{str}) + S\sigma \quad (8.1)$$

8.2 Theoretical Background of Transformation Kinetics

where ΔG_V^{ch} ($= \Delta G_m^{ch}/V_m$; ΔG_m^{ch} is the chemical Gibbs energy difference per mole of atoms between product phase and parent phase and V_m is the molar volume) is the chemical Gibbs energy difference between product phase and parent phase per unit volume, E_V^{str} ($= E_m^{str}/V_m$); $= E_m^{str}$ is the elastic strain energy per mole of atoms) is the elastic strain energy per unit volume and σ is the particle/matrix interface energy per unit area. For small overheating/undercooling, i.e. in the vicinity of the equilibrium phase-transformation temperature T_0 , the chemical Gibbs-energy change per mole of atoms $= \Delta G_m^{ch}$ can be approximately given as:

$$\Delta G_m^{ch} \approx \frac{\Delta H_{hcp \rightleftharpoons fcc}}{T_0} (T - T_0) = \frac{\Delta H_{hcp \leftrightarrow fcc}}{T_0} \Delta T \quad (8.2)$$

with $\Delta H_{hcp \rightleftharpoons fcc}$ as the molar enthalpy of transformation (fcc \rightarrow hcp: $\Delta H < 0$, hcp \rightarrow fcc: $\Delta H > 0$) and ΔT as the undercooling/overheating. The molar chemical Gibbs energy change ΔG_m^{ch} corresponds to the chemical driving force for the transformation and, as evident from equation (8.2), it changes its sign at T_0 . The elastic strain energy per unit volume, E_V^{str} , cannot be neglected since the product and the parent phases have unequal molar volumes (see section 8.5).

The volume of a product phase particle is given by

$$V = \frac{n}{2} c \cdot n \cdot D \quad (8.3)$$

with $nc/2$ as the height/size of the nucleus; $n/2$ is the number of dislocations within the array of dislocations oriented perpendicular to the stacking direction (cf. Figure 8.1 and Figure 8.3; n is the number of closed packed layers in the stack considered and c is the distance between adjacent dislocations in the array parallel to the c -axis ($c_{hcp} = 0.40686$ nm, $c_{fcc} = (2/3)\sqrt{3} a_{fcc} = 0.40931$ nm [157]), $2r$ is the separation distance of the partial dislocations (r is the distance passed by one array of Shockley partial dislocations) and D is the grain size of the parent crystal (cf. Figure 8.1).

The newly created interfacial area S of one particle is given by the top and the bottom side and the front and the rear side of the product-phase particle (as shown in Figure 8.1). Because $D \geq nc/2$, the interfacial area S is approximately given by the top and bottom sides and thus:

$$S \approx 2rD \quad (8.4)$$

It follows from equations (8.1), (8.3) and (8.4):

$$\Delta G_A \equiv \frac{\Delta G}{rD} = n \frac{c}{2V_m} (\Delta G_m^{ch} + E_m^{str}) + 2\sigma \quad (8.5)$$

The term $\Delta G/rD$ corresponds to the energy difference between the product phase/ particle and parent phase per unit area top/bottom interface, ΔG_A . Note that both the volume chemical energy term as well as the interface energy term scale with r .

Evidently, a critical size (a critical value of r) does not occur (cf. equation (8.5)): The transformation can take place “spontaneously”, i.e. without overcoming an energy barrier by thermal activation, provided that the energy difference between the product phase (lying in between the dissociated dislocation arrays) and parent phase per unit area, ΔG_A , becomes negative, e.g. by a change of temperature (cf. equations (8.2) and (8.5)). Hence, the product phase particles develop by athermal nucleation.

The interfacial term 2σ in equation (8.5) is independent of the height $nc/2$ of the possibly operating dislocation array, whereas the chemical Gibbs energy change for operation of the same dislocation array $nc\Delta G_m^{ch}/2V_m$ increases with n . For a fixed value of n the energy difference per unit area top/bottom interface, ΔG_A , equals zero at a finite value of undercooling, $\Delta T = T_0 - T$, for the fcc \rightarrow hcp transformation (or rather overheating, $\Delta T = T_0 - T$, for the hcp \rightarrow fcc transformation). A distribution of heights of the arrays of dislocations (corresponding with a varying number of closed packed layers, n , in the stack considered) is supposed to exist in the fcc crystal. It follows from equation (8.5) that the larger the height of the dislocation array, i.e. the larger n , the lower the required undercooling in order that this dislocation array starts to produce by glide a product phase (hcp) particle. In other words, the nucleation event can be described as a kind of site saturation at each temperature, where dislocation arrays of specific height start to operate.

At a given undercooling, $\Delta T(t) = T_0 - T(t)$, the critical (minimal) value of n , i.e. n^* , indicating the minimal height of the dislocation array for realising by glide the fcc \rightarrow hcp transformation, satisfies (see equations (8.2) and (8.5)):

$$n^*(\Delta T(t)) = - \frac{2\sigma}{\frac{c}{2V_m} \left(\frac{\Delta H_{hcp \rightleftharpoons fcc}}{T_0} (T - T_0) + E_m^{str} \right)} \quad (8.6)$$

Depending on the values of the parameters at the right hand side of equation (8.6), as σ , ΔH and E_m^{str} , a minimum number of stacked dislocations can be designated from n^* in order to obtain a stable nucleus that can grow. For example, considering the hcp \rightarrow fcc transformation above $T_0 = 690$ K, if $\Delta H_{hcp \rightleftharpoons fcc} = 501$ J mol $^{-1}$, $\sigma = 10$ mJ m $^{-2}$ [140], $E_m^{str} = 0.838$ J m 2 , it follows $n^* = 32$ at $T = 720$ K and $n^* = 24$ at $T = 730$ K. Upon decreasing temperature more and more dislocation arrays of decreasing height can be

come active. From experimental data for the martensitic transformation in Fe 30.2 wt% Ni, it was proposed that the cumulative number of operating dislocation arrays, $N(n^*(\Delta T(t)))$, obeys the empirical function [158]:

$$N(n^*(\Delta T(t))) = N_{tot} \exp(-n^*(\Delta T(t))) \quad (8.7)$$

with N_{tot} as the total number of pre-existing Shockley partial dislocation arrays of variable height per unit volume. The total number of preexisting SP arrays of variable height can be (over)estimated by approximating the grain volume by D^3 and recognizing that D/c represents the number of dislocations covering a height D . Hence, $N_{tot} = 2 \cdot (D/c)/D^3 = 2/cD^2$ taking into account that every perfect dislocation by dissociation contributes to the development of two nuclei (see Figure 8.1). This estimation is rough as at the begin of the transformation the number of SPs in a nucleus is larger than one. However, the values of the fit parameters of the transformation model do not depend strongly on the value of N_{tot} (see section 8.5). The above treatment focussed on the fcc→hcp transformation occurring upon cooling. A parallel treatment holds for the hcp→fcc transformation occurring upon heating.

8.2.3 Interface-controlled growth

When an ordered array of Shockley partial dislocations glides through the crystal (as shown in Figure 8.1 and Figure 8.3) the product phase particle grows. The dimensionality of the growth is one, i.e. the product phase particle grows in one of the three possible $\langle 11\bar{2} \rangle$ directions oriented perpendicular to the c -axis (cf. Figure 8.2). There is no composition change from parent to product phase in an allotropic phase transformation and thus the growth is controlled by atomic (jump) processes in the direct vicinity of the interface: interface-controlled growth. The height of a product phase particle which starts to grow at time τ is given by $n^*(\Delta T(\tau)) \cdot c/2$ (cf. Figure 8.1). Hence, at time t the volume $Y(\tau, t)$ of a product phase particle, which starts to grow at time τ , is given by (see Figure 8.1, equations (8.3) and (8.6))

$$Y_i(\tau, t) = D \frac{n^*(\Delta T(\tau))}{2} c r(T(t)) = D \frac{n^*(\Delta T(\tau))}{c} \int_{\tau}^t v dt' \quad (8.8)$$

with v as the interface/Shockley partial dislocation-glide velocity. For small undercooling or overheating the growth velocity v is given by

$$v(T(t)) = M(-\Delta G_m(T(t))) = M_0 \exp\left(-\frac{Q}{RT(t)}\right) (-\Delta G_m(T(t))) \quad (8.9)$$

where M is the temperature dependent interface mobility, M_0 is the pre exponential factor for growth and Q denotes the activation energy for growth. The net driving force $\Delta G_m(T(t))$ which is given as a molar quantity [8] amounts to (cf. equations (8.1) and (8.5)):

$$\Delta G_m(T(t)) = \frac{\Delta G}{rDn^*(\Delta T(t))\frac{c}{2V_m}} = \Delta G_m^{ch}(T(t)) + E_m^{str}(T(t)) + \frac{2\sigma}{n^*(\Delta T(t))\frac{c}{2V_m}} \quad (8.10)$$

8.2.4 Extended Fraction, Transformed Fraction and Impingement

Adopting an appropriate impingement mode, the *real* transformed fraction $f_{model}(T(t))$ can be calculated from the extended transformed fraction x_e (cf. beginning of section 8.2). In the case of anisotropic growth, which pertains to the allotropic phase transformation considered here (one dimensional growth; cf. section 8.2.3), the (hard) impingement process can be phenomenologically described by the following equation [8]:

$$\frac{df}{dx_e} = (1 - f)^\zeta \quad (8.11)$$

where ζ is a measure for the degree of anisotropic impingement. Integration of equation (8.11) for the case $\zeta > 1$ yields:

$$f = 1 - [1 + (\zeta - 1)x_e]^{-\frac{1}{\zeta-1}} \quad (8.12)$$

8.3 Experimental

8.3.1 Alloy Production

The cobalt rod with a diameter of 5 mm used in this study was obtained in the hammered, not annealed state from Alfa Aesar (Karlsruhe, Germany) and has a purity of 99.995 at.%. Disc shaped specimens were produced by cutting pieces with a thickness of 750 μm . Both sides of the specimen discs were prepared by grinding with SiC-paper and subsequently polishing using diamond paste down to 0.25 μm such that all specimens have approximately the same mass of about 100 mg. All specimens were cleaned ultrasonically in isopropyl. After the calorimetrical heat treatment the specimen discs were ground and polished again as mentioned above in order to reduce inhomogeneities of the surface as necessary for XRD and LM analysis.

8.3.2 Differential Scanning Calorimetry

The isochronal annealing was carried out with a power-compensated Differential Scanning Calorimeter (DSC) Pyris Diamond by Perkin Elmer. The temperature was calibrated using the melting temperature of zinc ($T_m = 692.15$ K [159]) measured for each heating rate used. Aluminum was used as pan material for both the specimen and reference container. Specimens of approximately the same mass were used in order to provide similar heat capacities. Pure argon gas with a constant flow was used as protective gas atmosphere. A measurement with empty pans served for determination of the baseline.

For each measurement in the temperature range from 523 K to 893 K at a heating rate varying from 10 K min^{-1} to 40 K min^{-1} a new specimen was used. In order to establish a microstructural reference state (see section 8.4), each specimen used for the kinetic analysis, was initially exposed to 60 isochronal transformation cycles with a cooling/heating rate of $\pm 50 \text{ K min}^{-1}$ in a temperature range from 523 K to 893 K. The microstructure and phase composition of the specimens in the initial state and after the 1st, 2nd, 3rd, 10th, 20th, 40th and 60th isochronal transformation cycles were analyzed by LM and XRD.

For the calculation of the cumulative enthalpy $\Delta H(T(t))$, as function of temperature (time), the heat signal $d\Delta H(T(t))/dt$ was integrated for cumulative times. Previous to this integration, it is necessary to perform a baseline correction. This was done by subtracting the above mentioned DSC signal recorded with empty pans from the DSC signal recorded with the Co specimen for each heating rate [159]. This implies that the heat capacities of both phases are the same in the temperature region of the transformation, as holds for cobalt. The transformed fraction $f_{exp}(T(t))$ as function of temperature then is given by:

$$f_{exp}(T(t)) = \frac{\Delta H(T(t))}{\Delta H_{hcp \rightleftharpoons fcc}} \quad (8.13)$$

where the total transformation enthalpy $\Delta H_{hcp \rightleftharpoons fcc}$ was obtained by integration of the baseline corrected DSC signal over the entire temperature range of the transformation.

8.3.3 X-Ray Diffraction

XRD was employed for phase analysis and to characterize the crystalline imperfection upon thermal cycling. The X-ray diffraction measurements

were performed with Mo K α radiation employing a Bruker D8 Discover diffractometer operating in parallel-beam geometry equipped with an X-ray lens in the incident beam, a parallel-plate collimator in the diffracted beam and an energy-dispersive detector. The 2θ -range of $15^\circ - 45^\circ$ was measured with a step size of 0.015° and counting time per step of 10 s.

8.3.4 Light Microscopy

The surface of the specimen discs before and after the 1st, 2nd, 3rd, 10th, 20th, 40th and 60th transformation cycles and of specimens used for the kinetic analysis were analysed using a Zeiss Axiophot light optical microscope. For that purpose the polished specimen discs were etched for 2–7 s using a fresh etching solution (14.3 vol.% H₂O, 14.3 vol.% CH₃COOH, 57.1 vol. % HCl and 14.3 vol.% HNO₃).

8.4 Results and Evaluation

A baseline corrected isochronal DSC-Scan of Co at a heating rate of 20 K min^{-1} showing a heat signal associated with the hcp \rightarrow fcc transformation is presented in Figure 8.4. T_{onset} denotes the peak onset temperature, T_{peak} is the peak maximum temperature and $\Delta H_{hcp\rightleftharpoons fcc}$ is the enthalpy of transformation (> 0 for the endothermic hcp \rightarrow fcc transformation) given by the (hatched) area enclosed by the DSC signal and the baseline (dashed).

In order to characterize the hcp \rightarrow fcc transformation behaviour and the microstructural evolution upon thermal cycling of initially heavily deformed Co, the change of the DSC heat signal (characterized by the parameters indicated above), XRD diffractograms and the change of the grain size were recorded as a function of the number of transformation cycles experienced (one cycle is hcp \rightarrow fcc followed by fcc \rightarrow hcp). Results are presented in Figure 8.5.

The variation of the parameters T_{onset} , T_{peak} and $\Delta H_{hcp\rightleftharpoons fcc}$ for the hcp \rightarrow fcc transformation (see Figure 8.4) is shown in Figure 8.5a as a function of the number of transformation cycles at a heating rate of 50 K min^{-1} between 523 K and 893 K. Starting from the heavily deformed initial state, the parameters T_{onset} , T_{peak} and $\Delta H_{hcp\rightleftharpoons fcc}$ decrease from the 1st to the 2nd transformation cycle from 736.3 K, 746.9 K and 406 J mol^{-1} to 717.1 K, 735.6 K and 385 J mol^{-1} , followed by an increase between the 2nd and 3rd transformation cycle to 721.9 K, 738.7 K and 452 J mol^{-1} , respectively. After the 3rd transformation cycle T_{onset} and T_{peak} pass through modest local maxima

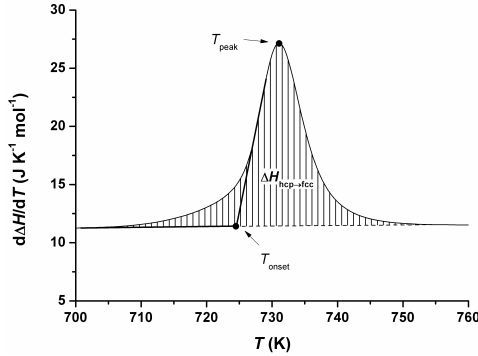


Figure 8.4: Heat signal corresponding to the endothermic hcp→fcc transformation in Co (after 61st cycles) obtained upon isochronal heating at a rate of 20 K min^{-1}

of about 722.3 K and 739.0 K , respectively. Eventually T_{onset} and T_{peak} approach asymptotically equilibrium values of about $735.7 \pm 0.2 \text{ K}$ (average of the last 40 transformation cycles) and about $726.5 \pm 0.2 \text{ K}$ (average of the last 20 transformation cycle), respectively.

The total transformation enthalpy, $\Delta H_{hcp \rightleftharpoons fcc}$, shows a steep increase from the 2nd to the 4th transformation cycle and approaches an equilibrium value after about 20 transformation cycles of about $500 \pm 3 \text{ J mol}^{-1}$ (average of the last 40 transformation cycles). The small values of $\Delta H_{hcp \rightleftharpoons fcc}$ observed in the first cycles suggest that the specimen only experiences a fractional hcp→fcc transformation during the first cycles.

XRD measurements of Co specimens at room temperature in the initial state and after the 1st, 2nd and 3rd transformation cycles (inset in Figure 8.5b) reveal 111 and 002 reflexes of the fcc Co phase after (only) the 1st and 2nd transformation cycle (Cards 89 4308 for hcp Co and 15 0806 for fcc Co of the powder diffraction file [160], were used for phase identification). In the initial state, after the 3rd transformation cycle and during further cycling no fcc Bragg peaks could be detected. These XRD results support the above interpretation of the $\Delta H_{hcp \rightleftharpoons fcc}$ changes during cycling.

Hence, the amount of hcp and fcc Co at room temperature after a specific number of transformation cycles can be deduced from the enthalpy data adopting direct proportionality of $\Delta H_{hcp \rightleftharpoons fcc}$ with the amount of hcp present before the hcp→fcc transformation takes place. The thus determined frac-

tional amounts of hcp and fcc phase at room temperature are shown in Figure 8.5b as function of the number of transformation cycles. The amount of fcc Co at room temperature reaches a maximum of about 25 % after two transformation cycles followed by a decrease towards nil reached at about the 5th transformation cycle.

The full width at half maximum (FWHM) was calculated for the 100, 002, 101, 102 110 and 103 reflexes of hcp Co. The FWHM results as obtained for the initial state and after the 1st, 2nd, 3rd, 10th, 20th, 40th and 60th transformation cycles are presented in Figure 8.5c as function of the corresponding transformation cycle number. For all reflexes a steep decrease can be observed from the values corresponding to the initial state to the values obtained after the 2nd/3rd transformation cycle. This decrease can be ascribed to a reduction of lattice defects in the initially heavily deformed state upon annealing (recovery), grain growth and transformation cycling. For all reflexes the FWHM and thus the defect structure remains about constant after the 3rd transformation cycle.

The change of the mean grain size, D , as determined by LM, is shown in Figure 8.5d as function of the number of transformation cycles. It was not possible to measure the grain size of Co in the initial stage because the etched microstructure did not allow a clear identification of grain boundaries: the highly deformed initial state leads to an uncontrollable etching process. The grain size increases upon thermal cycling from initially less than $10\ \mu\text{m}$ to about $87\pm 5\ \mu\text{m}$ after the 40th cycle and remains constant thereafter.

It has been concluded from the above results that, to assure the same initial state for each experiment used for kinetic analysis, each such specimen will be subjected to 60 transformation cycles before a kinetic analysis is performed. Important morphological characteristics are revealed by LM from the specimen surfaces, as shown for the 10th, 40th and 60th transformation cycles in Figures. 6a c. After the 10th cycle (Figure 8.6a) the etching suggests an underlying transformation structure exhibiting different, specific orientations of martensite plates within a Co grain. After the 40th cycle (Figure 8.6b) the etching suggests that only a single specific orientation is associated with the martensitic transformation experienced by a grain. After the 60th transformation cycle no such etch effect is observed (cf. Figure 8.10 and its discussion in section 8.6.1).

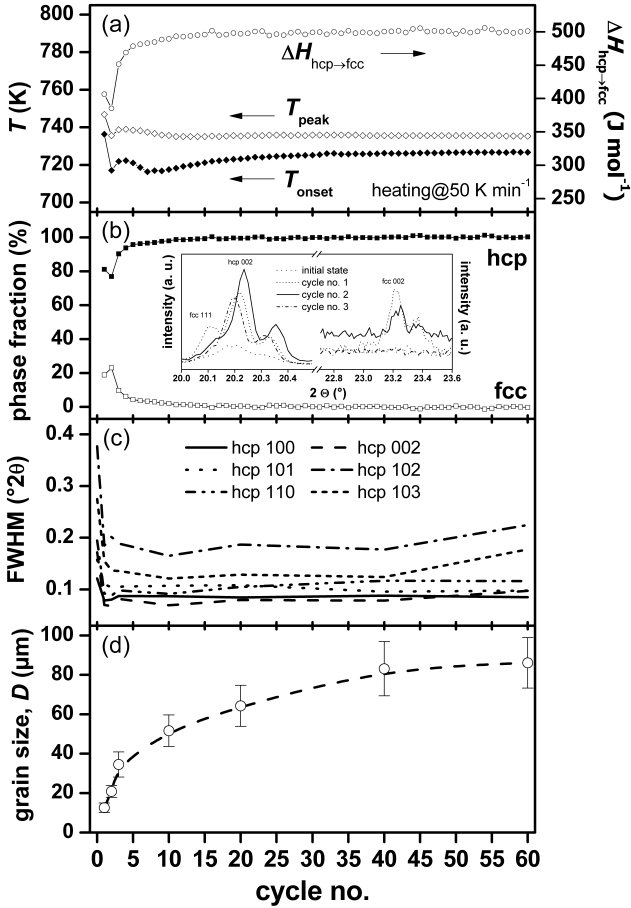


Figure 8.5: Results of DSC, XRD and LM analysis as function of the number of transformation cycles. (a) T_{onset} , T_{peak} and $\Delta H_{hcp \rightleftharpoons fcc}$ at a heating rate of $50 K min^{-1}$, (b) phase fraction as deduced from the enthalpy data in (a) (see text); inset: 111 and 002 reflexes of fcc phase and 002 reflexes of hcp phase before and after the 1st, 2nd and 3rd cycles, (c) FWHM of selected XRD reflexes as indicated and (d) grain size.

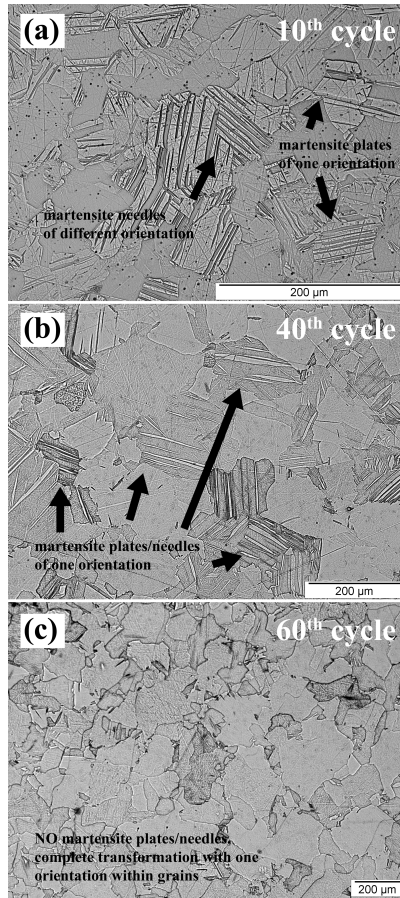


Figure 8.6: Light optical micrographs of the etched microstructure of the surface of Co specimens after the (a) 10th, (b) 40th and (c) 60th transformation cycle performed in the DSC at a rate of $\pm 50 \text{ K min}^{-1}$ in the temperature range from 523 K to 893 K. The etched microstructure suggests (see the arrows) that upon prolonged annealing the number of types of glide planes operating during the martensitic transformation (the fcc \rightarrow hcp experienced in the cooling part of the transformation cycle) in a single grain is reduced to one (see text and section 8.6.1).

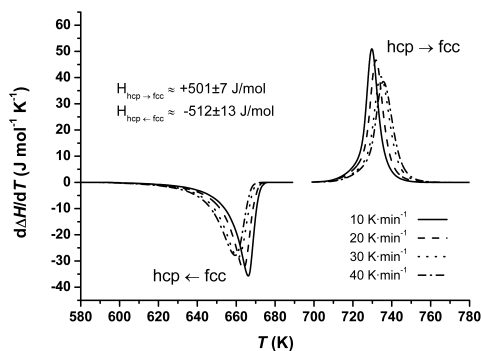


Figure 8.7: Isochronal baseline corrected DSC scans for Co (after 60 transformation cycles) at various heating rates as indicated.

8.5 Analysis of the Transformation Kinetics

Baseline corrected isochronal DSC scans for the allotropic hcp→fcc (upon heating) and fcc→hcp (upon cooling) transformations in Co measured at heating/cooling rates in the range from 10 K min^{-1} to 40 K min^{-1} are presented in Figure 8.7. The enthalpy of transformation for the hcp→fcc transformation (upon heating; independent of heating rate) is about $+501 \pm 7 \text{ J mol}^{-1}$ and for the fcc→hcp transformation (upon cooling; independent of cooling rate) about $512 \pm 13 \text{ J mol}^{-1}$, i.e. within the experimental accuracy the hcp→fcc and fcc→hcp transformations exhibit the same absolute value for the enthalpy of transformation.

The cooling curves in Figure 8.7, i.e. for the fcc→hcp transformation, have been included for the sake of completeness. Whereas the start temperature for the fcc→hcp transformation (upon cooling) clearly depends on the cooling rate applied, this is much less the case (if at all) for the dependence of the start temperature of the hcp→fcc transformation (upon heating) on heating rate (see Figure 8.7). In both cases, i.e. for the transformation upon cooling and the transformation upon heating, a cooling/heating rate independent start temperature is expected in view of the athermal value of the nucleation process (see section 8.2.2). It must be noted, that no temperature calibration of the DSC for the cooling part of the cycle is possible and that the DSC signal during cooling is smeared distinctly, as is well known for power compensated DSCs [159]. Therefore, the cooling-rate dependence of the start temperature of the transformation upon cooling has to be con-

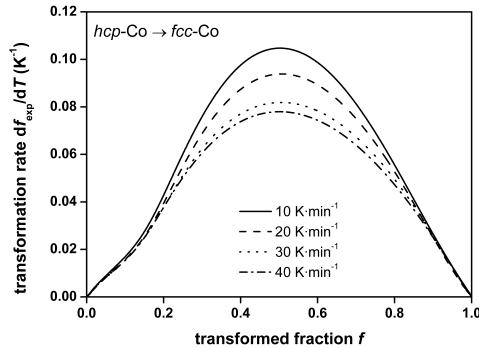


Figure 8.8: The experimental transformation rate df_{exp}/dT as function of the transformed fraction for the hcp \rightarrow fcc transformation for various heating rates. The plots show maxima at positions left with respect to the position $f = 1 - 1/e$, indicating an anisotropic impingement mode [161].

sidered as an artifact from the measurement and the cooling curves cannot be used for kinetic analysis.

The kinetic analysis of the allotropic hcp \rightarrow fcc transformation of Co was performed applying the modular phase transformation model in the form as described in section 8.2.

The experimental transformation rates df_{ex}/dT ($df_{ex}/dT = 1/\Phi df_{exp}/dt$) have been plotted in Figure 8.8 as function of the transformed fraction $f_{exp}(T(t))$ for the different heating rates. The corresponding curves for the experimentally determined transformed fractions $f_{exp}(T(t))$ (see section 8.3.2, equation (8.13)) are shown in Figure 8.9 as function of temperature $T(t)$. Evidently, the maximum transformation rate occurs at $f_{exp} < 1 - 1/e$. This is a strong indication for anisotropic growth [161] as expected for the hcp \rightleftharpoons fcc transformation in Co (cf. sections 8.2.2 and 8.2.3). The impingement mode for anisotropic growth (introduced in section 8.2.4) has thus been used in the kinetic model of the phase transformation.

The kinetic model parameters σ , Q and ξ were determined by numerically fitting of the model to simultaneously all isochronal heating runs obtained for various heating rates in the range from 10 K min^{-1} to 40 K min^{-1} . The mean square error (MSE) between the calculated (*calc*) and experimental (*exp*) transformed fraction curves was minimized by varying the fit para-

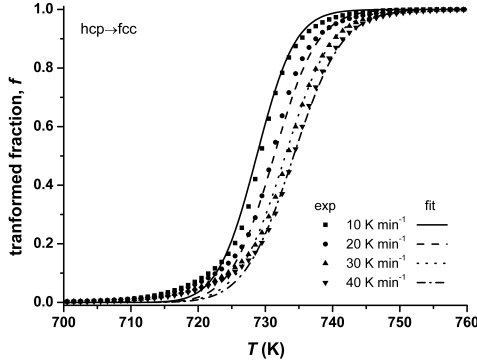


Figure 8.9: Isochronal DSC curves (symbols) and model fit (simultaneously to all runs) using the modular phase transformation model (σ , Q and ζ as fit parameters) for the allotropic phase transformation hcp \rightarrow fcc of Co.

eters using a multidimensional unconstrained nonlinear minimization fitting routine [162] as implemented in MATLAB for each ith of the applied heating rates

$$MSE = \sum_{i=1}^N \left(\frac{exp - calc}{exp} \right)^2 \quad (8.14)$$

The results of the fitting as described above are shown in Figure 8.9 (experimental data: symbols; fit: lines) and Table 1 (i.e. the values thus determined for σ , Q and ζ).

Values used for the constants in the model have (also) been given in Table 1. The total number of pre existing dislocations N_{tot} within a grain of mean size $D = 87 \pm 5 \mu\text{m}$ was calculated as described in section 8.2.2 as $6.5 \cdot 10^{17} \text{m}^{-3}$. The total enthalpy of transformation was taken as $\Delta H_{hcp \rightleftharpoons fcc} = 501 \pm 7 \text{J mol}^{-1}$, as determined experimentally (cf. section 8.4). The strain energy contribution expressed as E_m^{str} , corresponding with the macroscopic distortion discussed in sections 8.2.1 and 8.2.2, was estimated according to [143] at about 0.838J mol^{-1} under the assumption of linear elasticity and coherency (full elastic accommodation of volume misfit).

It is supposed that dislocation glide is rate controlled by thermal activation as it generally holds for materials with metallic bonding type. In pure metals it is assumed that the atomic structure within the closest packed glide

Table 8.1: Overview of the constants used in the adopted modular phase transformation model (see section 8.2), as well as the values obtained for the fit parameters by fitting this model to, simultaneously, all isochronal DSC scans upon heating.

	parameter	value	source
constants	enthalpy, $\Delta H_{hcp \rightleftharpoons fcc}$	$501 \pm 7 \text{ J mol}^{-1}$	experiment, this work
	grain size, D	$87 \text{ }\mu\text{m}$	experiment, this work
	lattice parameter, c	0.40686 nm	[157]
	equilibrium temperature, T_0	$690 \pm 7 \text{ K}$	[142]
	total number of pre existing dislocations, N_{tot}	$6.5 \cdot 10^{17} \text{ m}^{-3}$	$N_{tot} = 2/cD^2$; this work
	strain energy, E_{str}	0.838 J mol^{-1}	according to [143]
	mobility, M_0	$4.3 \text{ m mol J}^{-1} \text{ min}^{-1}$	$M_0 = v_0/RT$, v_0 estimated from [163]; this work
	interface energy, σ	$6.8 \pm 0.4 \text{ mJ m}^{-2}$	-
fit parameters	activation energy for growth, Q	$33 \pm 15 \text{ kJ mol}^{-1}$	-
	impingement parameter, ξ	1.35	-

plane represents a weak lattice resistance. The mobility of these dislocations is thus determined by thermal fluctuations characterized by an activation energy Q [164].

The temperature-independent dislocation/interface velocity v_0 was estimated by using the well-known (empirical) expression for the pre-exponential factor for lattice-resistance controlled glide of dislocations in metals (i.e. rate limited by weak discrete obstacles) (as validated for a wide range of metals [163]), which reads $\dot{\gamma} = v_0 \rho_m b = 10^6 \text{ s}^{-1}$ with ρ_m as the dislocation density and b as the Burgers vector taken equal to $1/2\sqrt{2}a_{fcc}$ with $a_{fcc} = 0.35447 \text{ nm}$ [157]. The density of mobile dislocations can be estimated according to [163] as 10^{13} m^{-2} lying in the range of values expected for fcc and hcp metals. The thus obtained value for v_0 is about 400 m s^{-1} . Thus the mobility $M_0 = v_0/RT$ [8] was assessed at $4.3 \text{ m mol J}^{-1} \text{ min}^{-1}$, adopting a mean value for the temperature $T = 700 \text{ K}$. Note that the temperature dependence of M_0 is small in comparison to the temperature dependence of the exponential term in M (see equation (8.9)) and thus the temperature dependence of M_0 can be neglected.

The influence of a variation of the constant parameters N_{tot} , T_0 and M_0 on the fit parameters, as indicated by $N_{tot} = 6.5 \cdot 10^{17 \pm 1} \text{ m}^{-3}$, $T_0 = 690 \pm 1 \text{ K}$ and $M_0 = 4.3 \cdot 10^{0 \pm 1}$, yielded variations of σ and Q as indicated in Table 1; the impingement parameter ξ is not influenced.

8.6 Discussion

8.6.1 Preceding transformation cycles

Each Co specimen used for kinetic analysis was subjected to a number of 60 preceding transformation cycles to assure similar starting conditions (same microstructure) and full transformation (see section 8.4). The phenomenon can be interpreted as that the preceding transformation cycles are needed to stabilize the dislocation configuration (cf. section 8.2.1) in the specimen that carries the forward (hcp→fcc) and backward (fcc→hcp) transformations. The initially incomplete transformation can partly be ascribed to the relatively strong interaction of the (partial) dislocations with the grain boundaries: upon increasing grain size during cycling (see Figure 8.5d) relatively more dislocations become available for establishing the transformation [126, 127, 133].

During the first transformation cycles the transformations occur in conjunction with recovery, possible (local) recrystallisation and grain growth in order to reduce the stored plastic deformation and grain boundary surface.

This leads to changes of the (initially disarranged) dislocation structure. A further complication is that after a first hcp→fcc transformation upon heating, that then, upon subsequent cooling, a completely reverse formation of hcp Co requires glide of SPs on the closest packed $\{111\}_{fcc}$ planes lying parallel to the previous $\{0001\}_{hcp}$ planes. However, at least initially SPs may be available as well on $\{111\}_{fcc}$ planes not parallel to the former $\{0001\}_{hcp}$ plane and thus the original hcp grain microstructure is not re-established (Note the variously orientated hcp Co martensite “plates” in a single grain in Figure 8.6a). As a consequence, this reasoning provides a further reason (see above) why the transformation cannot run to completion in such a grain; a small amount of parent phase is retained (see Figure 8.5b and its inset).

The above described transformation behaviour for the first transformation cycles is compatible with the DSC results. The decrease of T_{onset} and T_{peak} found for the 2nd transformation cycle can be understood such that during the first complete hcp↔fcc cycle the disordered dislocation structure of the initial state evolves into a more ordered (in the sense of the discussion in section 8.2.1) dislocation structure, thereby facilitating the transformation: less overheating is required (see section 8.2.2).

Prolonged thermal cycling leads to an increase of the thickness of the martensite “plates” (Figure 8.6b), i.e. the height of the operating dislocation array increases, and a single glide variant appears to become dominant (cf. Figure 8.6b and c) [133,135].

The above discussion leads to a summarizing schematic presentation of the evolving dislocation structure in a grain during hcp↔fcc (thermal) cycling as presented in Figure 8.10.

8.6.2 Kinetics

The evaluation of the kinetics of the allotropic hcp→fcc phase transformation in Co performed in section 8.5 demonstrates that this transformation can be well described as governed by the activation of pre existing nuclei (stacked dislocation sequences) and thermally activated interface controlled growth subjected to anisotropic impingement. The resulting values for the fit parameters σ , Q and ξ agree well with data provided by theory and experiment (see what follows). The investigation of dislocation nodes (the extension of a dislocation node depends amongst others on the stacking fault energy produced by the node) in pure Co [140] and Fe Cr Ni alloys [165] yielded stacking fault energy values from 5 to 10 mJ m⁻². This agrees very well with the here determined value for the interface (= stack-

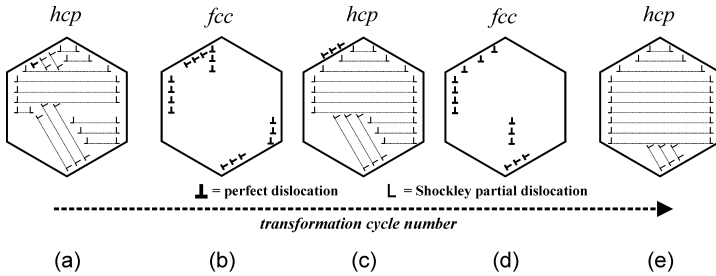


Figure 8.10: Schematic presentation of the dislocation structure development in Co upon $hcp \rightleftharpoons fcc$ (thermal) cycling. (a) The initial state represents (severely deformed) hcp Co as formed by dissociation of arrays of perfect dislocations and subsequent “ordered” glide of SPs on every second closest packed $\{111\}$ plane in the parent fcc Co. The whole grain could not transform to hcp Co because of blocking of the growing martensite “plates” growing by “ordered” glide of arrays of SPs; each stack of SPs glides along one of the four equivalent types of $\{111\}_{fcc}$ planes. (b) + (c) Upon continued thermal cycling the height of the (remaining, active) stacks of arrays of (partial) dislocations (perpendicular to $\{0001\}_{hcp} / \{111\}_{fcc}$ planes) increases, due to pick up of neighbouring dislocations, pushing aside unfavourably oriented smaller dislocation stacks, e. g. by limiting the associated SP glide, and by even driving them back (in associated form) into the grain boundaries (as illustrated in the figure; cf. (a) and (c)). (d) + (e) Eventually, upon prolonged thermal cycling, a dislocation structure emerges that realizes the $hcp \rightleftharpoons fcc$ transformation on the basis of (ideally) one single stack of ordered perfect dislocations (in fcc) = 2 parallel stacks of ordered Shockley partial dislocations (in hcp) implying that only one (instead of, maximally, four; see (a) + (b)) glide plane system operates within a single grain, e. g. $(111)_{fcc} \parallel (0001)_{hcp}$, $[\bar{1}\bar{1}0]_{fcc} \parallel [\bar{1}0\bar{1}0]_{hcp}$.

ing fault) energy resulting from model fitting of the transformation kinetics yielding $\sigma = 6.7 \pm 0.4 \text{ mJ m}^{-1}$.

The ratio of the activation energy for diffusion and the activation energy for dislocation glide controlled by lattice resistance is for metals about 7 [163]. The activation energy for self diffusion of Co is $Q_{Co} = 270 \text{ kJ mol}^{-1}$ [127]. Indeed, $1/7Q_{Co} \approx 38 \text{ kJ mol}^{-1}$ which is well compatible with the here determined value of the activation energy for growth, $Q = 33 \pm 15 \text{ kJ mol}^{-1}$, thereby validating the applied concept of growth controlled by dislocation glide.

8.7 Conclusions

- Extensive thermal cycling of Co in a fixed temperature range is necessary to establish full reversibility of the allotropic hcp \rightleftharpoons fcc phase transformation (i.e. reaching constant values of T_{onset} , T_{peak} and $\Delta H_{hcp\rightleftharpoons fcc}$). During thermal cycling stabilization of the dislocation structure is established such that in a single grain the hcp \rightleftharpoons fcc transformation is established by (ideally) only one single stack of ordered perfect dislocations (in fcc) = 2 parallel stacks of ordered Shockley partial dislocations (in hcp), implying that only one (of the maximally four) glide plane types operates within a single grain.
- The kinetics of the transformation can be well described on the basis of a modular transformation model adopting an athermal nucleation mode and an anisotropic interface controlled growth mode.
- Results obtained for the fit parameters σ ($= 6.7 \pm 0.4 \text{ mJ m}^{-2}$) and Q ($= 33 \pm 15 \text{ kJ mol}^{-1}$) are well compatible with the interpretation of the product/parent interface as a stacking fault and of the growth process as realized by thermally activated glide of Shockley partial dislocations.

Chapter 9

Summary

9.1 Summary in the English language

In this thesis, the interplay of phase transformation kinetics and the microstructure of materials is investigated. During a phase transformation, the parent microstructure is replaced by the product microstructure according to a specific phase transformation mechanism. Three different aspects of the interaction between microstructure and phase-transformation kinetics are considered. Firstly, the microstructure resulting from phase transformations with a known mechanism is investigated. Secondly, the influence of the parent microstructure on the resulting phase-transformation kinetics is studied. Thirdly, a combined knowledge about the product microstructure and the phase-transformation kinetics is used to identify suitable models for a specific phase transformation.

Several heterogeneous, nucleation-and-growth phase transformations in elemental metals are considered in this thesis, which all pertain to interface-controlled growth (i.e. growth without long-range diffusion).

The kinetics of such phase transformations can be modelled by employing mean-field approaches. The most widely used models of this type, the classical Johnson-Mehl-Avrami-Kolmogorov (JMAK) model and JMAK-like models, are only valid under certain circumstances, including a spatially random arrangement of nuclei and a homogeneous growth rate in the entire specimen. Within the framework of the modular kinetic model approach, empirical impingement equations are available which allow an approximate description of the transformation kinetics for phase transformations in which the above-stated restrictions are violated. Therefore, they broaden the range of treatable phase transformation mechanisms. For the special case of phase transformations for which nucleation occurs on parent-phase grain boundaries, a more “physical” model due to Cahn is available.

Without recourse to a kinetic model, the kinetics and the resulting microstructure of phase transformations can be simulated using various mesoscopic simulation algorithms. In the present thesis, geometrical simulations, which model the growth of product grains on the basis of global growth

rules, as well as Cellular Automata simulations, which model the growth of product grains on the basis of local growth rules, are employed.

In **chapter 2**, the microstructures resulting from nucleation-and-growth phase transformations occurring under various time-temperature programs are simulated and analysed. The transformation kinetics is described by a modular kinetic model and informations from this model are used to provide “global” rules for application in a geometric algorithm to simulate the microstructure. The microstructures for heating and cooling transformations, in particular as revealed by the grain-size distributions, differ distinctly as a consequence of the different temperature-dependencies of the nucleation and growth rates. The differences in grain-size distributions on the basis of volume-weighted, area-weighted and line-intercept grain sizes are discussed in the light of their sensitivity for revealing the kinetics of the underlying phase transformation.

In the **chapters 3 and 4**, the kinetics of phase transformations for which nucleation occurs on parent-microstructure grain boundaries, and the resulting microstructures, are investigated by means of geometric simulations. The influences of parent microstructure grain-boundary area density, parent grain-size distribution and parent→product kinetics are analysed.

In **chapter 3**, the simulated kinetics are compared with predictions from two kinetic models, namely a model proposed for spatially random nucleation and a model proposed for grain-boundary nucleation. It is found that the simulated transformed fraction as function of time lies in between the two model predictions for all investigated parent microstructures and parent→product kinetics.

In **chapter 4**, several mesoscopic kinetic models are investigated with respect to their ability to describe the simulated transformation kinetics, namely

- the classical JMAK model (i.e. assuming random nucleation),
- previously proposed empirical extensions of the JMAK model in the framework of the modular kinetic model approach,
- the Cahn model (assuming nucleation on randomly distributed planes), and
- a new, here proposed empirical extension of the Cahn model.

None of the models exactly predicts the real phase transformation kinetics. The classical JMAK model is unable to describe the simulated grain-boundary nucleated transformation kinetics. The Cahn model leads to er-

aneous results upon fitting to simulated transformation curves. It is concluded that the here proposed modified Cahn model is best suited to infer correct values of kinetic material parameters from experimentally obtained data about the kinetics of grain-boundary nucleated phase transformations.

Chapter 5 provides a summary of chapters 2–4. Additionally, results of recently published research on atomistic (kinetic Monte Carlo) simulations are reviewed. In particular, the atomic (jump) processes occurring during interface movement in the massive austenite→ferrite phase transformation in pure iron are discussed.

In the **chapters 6 and 7**, the kinetics and the resulting microstructure of the static recrystallisation of pure copper are investigated by experiments and by mesoscopic simulations.

In **chapter 6**, the kinetics of the recrystallisation is investigated by differential scanning calorimetry (DSC). The associated microstructural change is characterised by electron backscatter diffraction imaging (EBSD), by analysing deformed specimens before recrystallisation and specimens after partial recrystallisation and after completed recrystallisation. The experimental results acquired by the two methods are compared with each other and discussed in the context of the available body of literature results. The observed kinetics deviate from JMAK-like behaviour. The observed grain-area distribution is unusually broad and skewed towards large grains. Comparison with mesoscopic, geometric simulations shows that previously proposed (simple) models fail to correctly describe the microstructure resulting from recrystallisation, although they can successfully model the recrystallisation kinetics. It is concluded that the experimental results on both the kinetics and the microstructure can be reconciled employing a recrystallisation model incorporating ongoing (i.e. beyond time $t = 0$) nucleation and accounting for the inhomogeneous nature of the deformed material.

In **chapter 7**, the kinetics and microstructure of the recrystallisation were investigated on the basis of a comparison of mesoscopic, cellular automata simulations with experimental data from the previous chapter. Physical models for the nucleation rate and the growth rate of recrystallised grains were employed which require experimentally obtained informations about the deformed state as input. The orientation-distribution function and the misorientation-angle distribution for neighbouring grains of deformed specimens were used to set up the microstructure serving as start configuration for the simulations. The influence of a subgrain-size distribution, of an ongoing nucleation during recrystallisation, of an inhomogeneously distributed stored energy in the deformed state and of a misorientation-dependent interface mobility were investigated. The simulated microstructures after

recrystallisation exhibit a bimodal grain-size distribution instead of the very broad, monomodal grain-size distribution found in the experiments. It is argued that spatially resolved determination of crystal (subgrain) orientation and (deformation) energy is necessary to arrive at realistic descriptions of both the recrystallisation kinetics and the microstructure after completed recrystallisation.

In **chapter 8**, the allotropic, martensitic phase transformation $\text{hcp} \rightleftharpoons \text{fcc}$ in cobalt is investigated by DSC upon isochronal annealing at heating rates in the range from 10 K min^{-1} to 40 K min^{-1} . The microstructural evolution is traced by light optical microscopy (LM) and X ray diffractometry (XRD). The kinetics of the phase transformation from hcp to fcc Co upon isochronal annealing is described on the basis of a modular phase transformation model. Appropriate model descriptions for athermal nucleation and thermally activated, anisotropic, interface-controlled growth tailored to the martensitic phase transformation of Co are implemented into the modular model. Fitting of this kinetic model to simultaneously all isochronal DSC runs yields values for the energy of the interface separating the hcp and fcc Co phase and the activation energy for growth.

9.2 Zusammenfassung in der deutschen Sprache

In dieser Arbeit wird das Wechselspiel zwischen der Phasenumwandlungskinetik und dem Gefüge von Materialien untersucht. Während einer Phasenumwandlung wird das Ausgangsgefüge eines Materials durch das resultierende Gefüge gemäß dem vorliegenden Phasenumwandlungsmechanismus ersetzt. Es werden drei verschiedene Aspekte der Wechselwirkung zwischen Gefüge und Umwandlungskinetik betrachtet. Erstens wird das Gefüge ermittelt, das aus Phasenumwandlungen mit bekanntem Mechanismus resultiert. Zweitens wird der Einfluss des Ausgangsgefüges auf die resultierende Phasenumwandlungskinetik untersucht. Drittens werden Kenntnisse sowohl über das resultierende Gefüge als auch der Umwandlungskinetik benutzt, um geeignete kinetische Modelle für eine bestimmte Phasenumwandlung zu identifizieren.

Die Diskussion in dieser Arbeit ist beschränkt auf heterogene Keimbildungs- und -wachstumsumwandlungen in reinen Metallen, die grenzflächenkontrolliert, d.h. ohne langreichweitige Diffusion, ablaufen.

Die Kinetik von Phasenumwandlungen kann mit Hilfe eines *mean-field*-Ansatzes modelliert werden. Die bekanntesten Vertreter dieses Modelltyps, das klassische Johnson-Mehl-Avrami-Kolmogorov (JMAK) -Modell sowie

die JMAK-artigen Modelle, gelten nur für bestimmte Umwandlungsmechanismen. Unter anderem müssen die Keime räumlich zufällig in einer Probe verteilt sein und die vorliegende Wachstumsrate muss überall in der Probe identisch sein. Im Rahmen des modularen Modellansatzes sind empirische Zusammenstoß-Gleichungen verfügbar, die Näherungslösungen für Fälle darstellen, in denen gegen die eben genannten Beschränkungen verstossen wird. Für den Spezialfall der Keimbildung auf Korngrenzen im Ausgangsgefüge (d.h. einer räumlich nicht-zufälligen Keimbildung) ist ein "physikalisches" Modell nach Cahn verfügbar.

Ohne sich auf ein bestimmtes kinetisches Modell zu beziehen können die Phasenumwandlungskinetik und das resultierende Gefüge mit Hilfe von mesoskopischen Simulationen ermittelt werden. In der vorliegenden Arbeit werden geometrische Simulationen, die mit globalen Transformationsregeln operieren, sowie Zelluläre-Automaten-Simulationen, die mit lokalen Transformationsregeln operieren, verwendet.

In **Kapitel 2** wird das Gefüge, das sich aufgrund bestimmter Keimbildungs- und -wachstumsphasenumwandlungen ergibt, simuliert und analysiert. Die Umwandlungskinetik folgt dabei einem modularen Modell, dessen Bestandteile auch die "globalen" Transformationsregeln einer geometrischen Simulationsmethode darstellen. Die Gefüge, insbesondere die Korngrößenverteilungen, die sich aufgrund von Phasenumwandlungen während des Aufheizens und während des Abkühlens einer Probe ergeben, unterscheiden sich drastisch, da Keimbildungs- und -wachstumsrate unterschiedliche Temperaturabhängigkeiten aufweisen. Die Unterschiede zwischen Kornvolumenverteilungen, Kornflächenverteilungen und Sehnenlängenverteilungen werden verglichen und ihre Eignung zur Analyse der zugrundeliegenden Phasenumwandlungskinetik wird diskutiert.

In **Kapitel 3 und 4** wird die Kinetik von Phasenumwandlungen, deren Keimbildung auf den Korngrenzen der Ausgangsphase stattfindet, sowie das resultierende Gefüge, mit Hilfe von geometrischen Simulationen untersucht. Die Einflüsse der Korngrenzenflächendichte des Ausgangsgefüges, der Korngrößenverteilung des Ausgangsgefüges, sowie der eigentlichen Phasenumwandlungskinetik werden untersucht.

In **Kapitel 3** wird die simulierte Umwandlungskinetik mit den Vorhersagen zweier kinetischer Modelle verglichen; einerseits mit einem Modell das für räumlich zufällig verteilte Keime entwickelt wurde und andererseits mit einem Modell, das für Korngrenzenkeimbildung entwickelt wurde. Für alle untersuchte Ausgangsgefüge und Kinetiken liegt der simulierte Verlauf des Umwandlungsgrades zwischen diesen beiden Modellvorhersagen. Das Maximum der Korngrößenverteilung des resultierenden Gefüges

verschiebt sich zu umso kleineren Korngrößen, je ausgeprägter der Einfluss der Korngrenzenkeimbildung wird.

In Kapitel 4 wird untersucht, inwiefern verschiedene kinetische Modelle geeignet sind, um die Kinetik von Phasenumwandlungen, deren Keimbildung auf den Korngrenzen der Ausgangsphase stattfindet, zu beschreiben. Behandelt werden

- das JMAK-Modell, das von zufällig verteilten Keimen ausgeht,
- empirische Erweiterungen des JMAK-Modells, die im Rahmen des modularen kinetischen Modell-Ansatzes entwickelt wurden,
- das Cahn-Modell, das Keimbildung auf zufällig verteilten Ebenen behandelt, sowie
- eine neue empirische Erweiterung des Cahn-Modells.

Keines dieser Modelle kann die tatsächliche Umwandlungskinetik exakt vorhersagen. Das JMAK-Modell kann mit keiner der möglichen Parameterkombinationen die simulierte Umwandlungskinetik beschreiben. Das Cahn-Modell kann die Kinetik zwar beschreiben, liefert aber fehlerhafte, d.h. von den Input-Werten der Simulation abweichende Werte für die durch die Modellanpassung ermittelten kinetischen Parameter. Die neu vorgeschlagene Erweiterung des Cahn-Modells ist am besten geeignet um zuverlässig Materialparameter durch Modellanpassungen an experimentell ermittelte Phasenumwandlungskinetiken, deren Keimbildung auf Korngrenzen des Ausgangsgefüges stattfindet, zu bestimmen.

Kapitel 5 stellt eine Zusammenfassung der Kapitel 2–4 dar. Darüber hinaus werden Literaturdaten von atomistischen Simulationen der massiven Austenit→Ferrit-Umwandlung in reinem Eisen besprochen. Insbesondere wird diskutiert welchen Einfluss die atomaren Sprungprozesse an der Phasengrenzfläche auf die Mobilität der Grenzfläche haben.

In **Kapitel 6** wird die Kinetik der Rekristallisation von reinem Kupfer mit Hilfe von isothermer Differential-Scanning-Kalorimetrie (DSC) untersucht. Die dabei stattfindende Gefügeentwicklung wird mittels Elektronen-Rückstreu-Beugung (EBSD) verfolgt. Es werden verformte Proben vor der Rekristallisation, teilweise rekristallisierte Proben sowie vollständig rekristallisierte Proben untersucht. Die experimentellen Daten, die mit den beiden Methoden gewonnen wurden, werden miteinander verglichen und sie werden gemeinsam mit vorhandenen Literaturdaten diskutiert. Die beobachtete Rekristallisationskinetik zeigt Abweichungen von JMAK-artigem Verhalten. Die ermittelte Kornflächenverteilung ist ungewöhnlich breit und asym-

metrisch (mit einem Maximum bei kleinen Kornflächen). Vergleiche mit mesoskopischen, geometrischen Simulationen zeigen, dass bekannte (einfache) Modelle das aus der Rekristallisation resultierende Gefüge nicht korrekt beschreiben können, obwohl sie die Rekristallisationskinetik korrekt wiedergeben. Es wird geschlossen dass die experimentellen Daten bezüglich der Rekristallisationskinetik und des resultierenden Gefüges nur dann zusammengeführt werden können, wenn ein Rekristallisationsmodell aufgestellt wird, das anhaltende Keimbildung (d.h. auch nach Beginn der Rekristallisation) beinhaltet sowie das die Inhomogenität des Ausgangsgefüges berücksichtigt.

In **Kapitel 7** wird die Kinetik und das resultierende Gefüge der Rekristallisation von reinem Kupfer mit Hilfe von Zellulären-Automaten-Simulationen untersucht, sowie mit den experimentellen Daten des vorherigen Kapitels verglichen. Die eingesetzten "physikalischen" Modelle für die Keimbildungs- und -wachstumsrate der rekristallisierten Körner benötigen experimentelle Daten über das Ausgangsgefüge als Input. Die kristallographische Orientierungsverteilungsfunktion sowie die Misorientierungswinkelverteilung werden verwendet um das Ausgangsgefüge der Simulationen zu konstruieren. Der Einfluss von während der Rekristallisation anhaltender Keimbildung, von einer (räumlich) inhomogen verteilten Verformungsenergie, sowie von einer Misorientierungswinkelabhängigen Grenzflächenmobilität werden untersucht. Die simulierten resultierenden Gefüge nach erfolgter Rekristallisation zeigen eine bimodale Korngrößenverteilung anstatt der experimentell beobachteten breiten monomodalen Verteilung. Es wird argumentiert dass eine orts aufgelöste Kenntnis der Kristall- (Subkorn-) orientierungen und der Verformungsenergien notwendig ist, um zu einer realistischen Beschreibung sowohl der Rekristallisationskinetik als auch des resultierenden Gefüges nach vollständiger Rekristallisation zu gelangen.

In **Kapitel 8** wird die allotrope martensitische Phasenumwandlung zwischen der hexagonal dichtestgepackten (hdp) und der kubisch dichtestgepackten (kfz) Kristallstruktur in reinem Kobalt untersucht. DSC-Experimente während isochronem Heizen mit Heizraten von 10 K min^{-1} bis 40 K min^{-1} werden durchgeführt. Die Entwicklung des Gefüges wird mittels Lichtmikroskopie und Röntgebeugung verfolgt. Die Kinetik der hdp→kfz Phasenumwandlung wird im Rahmen des modularen kinetischen Modell-Ansatzes beschrieben. Dabei werden für die Beschreibung der martensitischen Umwandlung geeignete Modellbeschreibungen für athermale Keimbildung sowie thermisch aktiviertes, anisotropes und grenzflächenkontrolliertes Wachstum angepasst und in den modularen Ansatz integriert. Aus der simultanen Anpassung des Modells an experimentell (kalorimetrisch) ermittelte

Chapter 9 Summary

Phasenumwandlungskinetiken (bei verschiedenen Heizraten) werden die Grenzflächenenergie zwischen hexagonalem und kubischem Kobalt, sowie die Wachstumsaktivierungsenergie erhalten.

Bibliography

- [1] E. J. Mittemeijer. *Fundamentals of Materials Science*. Springer, Berlin, 2010.
- [2] J. W. Christian. *The Theory of Transformations in Metals and Alloys*. Pergamon, Oxford, 2nd edition, 2002.
- [3] J. L. Meijering. Interface area, edge length, and number of vertices in crystal aggregates with random nucleation. *Philips Research Reports*, 8:270–290, 1953.
- [4] E. N. Gilbert. Random subdivisions of space into crystals. *Annals of Mathematical Statistics*, 33:958–972, 1962.
- [5] A. N. Kolmogorov. Zur Statistik der Kristallisationsvorgänge in Metallen. *Izv. Akad. Nauk SSSR Ser. Mat.*, 1:355–359, 1937.
- [6] M. Avrami. Kinetics of phase change I (general theory). *The Journal of Chemical Physics*, 7:1103–1112, 1939.
- [7] W. A. Johnson and R. F. Mehl. Reaction kinetics in processes of nucleation and growth. *Trans. Am. Inst. Min. Metall. Eng.*, 135:416–442, 1939.
- [8] F. Liu, F. Sommer, C. Bos, and E.J. Mittemeijer. Analysis of solid state phase transformation kinetics: models and recipes. *International Materials Reviews*, 52(4):193–212, 2007.
- [9] B. S. Lement and M. Cohen. A dislocation-attraction model for the first stage of tempering. *Acta Metallurgica*, 4(5):469–476, 1956.
- [10] M. Hillert. The kinetics of the first stage of tempering. *Acta Metallurgica*, 7(10):653–658, 1959.
- [11] J. W. Cahn. The kinetics of grain boundary nucleated reactions. *Acta Metallurgica*, 4(5):449–459, 1956.

Bibliography

- [12] K. W. Mahin, K. Hanson, and J. W. Morris. Comparative analysis of the cellular and Johnson-Mehl microstructures through computer simulation. *Acta Metallurgica*, 28:443–453, 1980.
- [13] H. J. Frost and C. V. Thompson. The effect of nucleation conditions on the topology and geometry of two-dimensional grain structures. *Acta Metallurgica*, 35:529–540, 1987.
- [14] D. Juul Jensen. Modelling of microstructure development during recrystallization. *Scripta Metallurgica et Materialia*, 27:1551–1556, 1992.
- [15] A. D. Rollett and P. Manohar. *Continuum Scale Simulation of Engineering Materials*, chapter “The Monte Carlo Method”, pages 77–114. Wiley-VCH, 2004.
- [16] H. W. Hesselbarth and I. R. Göbel. Simulation of recrystallization by Cellular Automata. *Acta Metallurgica et materialia*, 39:2135–2143, 1991.
- [17] D. Raabe. Cellular automata in materials science with particular reference to recrystallization simulation. *Annual Review Of Materials Research*, 32:53, 2002.
- [18] L.-Q. Chen. Phase-field models for microstructure evolution. *Annual reviews in Materials Research*, 32:113–1304, 2002.
- [19] C. R. Hutchinson, M. Gouné, and A. Redjaimia. Selecting non-isothermal heat treatment schedules for precipitation hardening systems: An example of coupled process-property optimization. *Acta Materialia*, 55:213–223, 2007.
- [20] Y. C. Liu, F. Sommer, and E. J. Mittemeijer. Abnormal austenite-ferrite transformation kinetics of ultra-low nitrogen Fe-N alloy. *Metallurgical and Materials Transactions A*, 39A:2306–2318, 2008.
- [21] M. Avrami. Kinetics of phase change II (transformation-time relations for random distributions of nuclei). *The Journal of Chemical Physics*, 8:212–224, 1940.
- [22] T. Kiang. Random fragmentation in two and three dimensions. *Zeitschrift für Astrophysik*, 64:433–439, 1966.
- [23] J.-S. Ferenc and Z. Neda. On the size distribution of Poisson-Voronoi cells. *Physica A-Statistical Mechanics And Its Applications*, 385(2):518–526, 2007.

- [24] J. Farjas and P. Roura. Cell size distribution in a random tessellation of space governed by the Kolmogorov-Johnson-Mehl-Avrami model: Grain size distribution in crystallization. *Physical Review B*, 78(14):144101, 2008.
- [25] E. Pineda, P. Bruna, and D. Crespo. Cell size distribution in random tessellations of space. *Physical Review E*, 70(6):066119, Dec 2004.
- [26] D. Crespo and T. Pradell. Evaluation of time-dependent grain-size populations for nucleation and growth kinetics. *Physical Review B*, 54(5):3101–3109, 1996.
- [27] J. Farjas and P. Roura. Numerical model of solid phase transformations governed by nucleation and growth: Microstructure development during isothermal crystallization. *Physical Review B*, 75(18):184112, May 2007.
- [28] J. Farjas and P. Roura. Solid-phase crystallization under continuous heating: Kinetic and microstructure scaling laws. *Journal of Materials Research*, 23:418–426, 2008.
- [29] E. J. Mittemeijer. Analysis of the kinetics of phase transformations. *Journal of Materials Science*, 27:3977–3987, 1992.
- [30] Y. C. Liu, D. Wang, F. Sommer, and E. J. Mittemeijer. Isothermal austenite-ferrite transformation of Fe-0.04% C alloy: Dilatometric measurement and kinetic analysis. *Acta Materialia*, 56:3833–3842, 2008.
- [31] A. T. W. Kempen, H. Nitsche, F. Sommer, and E. J. Mittemeijer. Crystallization kinetics of amorphous magnesium-rich magnesium-copper and magnesium-nickel alloys. *Metallurgical and Materials Transactions A*, 33(4):1041–1050, 2002.
- [32] H. Nitsche, M. Stanislawski, F. Sommer, and E. J. Mittemeijer. Kinetics of crystallization of amorphous Mg₈₀Cu₁₀Y₁₀. *Zeitschrift für Metallkunde*, 96(12):1341–1350, 2005.
- [33] American Society for Testing and Materials. *Annual Book of ASTM Standards*, volume 03.01, chapter E112, pages 237–259. 1999.
- [34] J. C. Russ and R. T. Dehoff. *Practical Stereology*. Kluwer Academic, 2nd edition, 2000.

Bibliography

- [35] E. A. Jäggle and E. J. Mittemeijer. Predicting microstructures from phase transformation kinetics: The case of isochronal heating and cooling from a supersaturated matrix. *Modelling and Simulation in Materials Science and Engineering*, 18(6):065010, 2010.
- [36] R. Bauer, B. Rheingans, and Mittemeijer E. J. The kinetics of the precipitation of Co from supersaturated Cu-Co alloy. *Metallurgical and Materials Transactions A*, 42A(7):1750–1759, 2011.
- [37] P. Krüger and E. Woldt. The use of an activation energy distribution for the analysis of the recrystallization kinetics of copper. *Acta Metallurgica et Materialia*, 40:2933–2942, 1992.
- [38] S. J. Jones and H. K. D. H. Bhadeshia. Kinetics of the simultaneous decomposition of austenite into several transformation products. *Acta Materialia*, 45(7):2911–2920, 1997.
- [39] L. E. Levine, K. Lakshmi Narayan, and K. F. Kelton. Finite size corrections for the johnson-mehl-avrami-kolmogorov equation. *Journal of Materials Research*, 12:124–132, 1997.
- [40] M. Starink. On the meaning of the impingement parameter in kinetic equations for nucleation and growth reactions. *Journal of Materials Science*, 36(18):4433–4441, 2001.
- [41] S. Storm and D. Juul Jensen. Effects of clustered nucleation on recrystallization. *Scripta Materialia*, 60:477–480, 2009.
- [42] J. W. Cahn. The time cone method for nucleation and growth kinetics on a finite domain. In J. S. Im, B. Park, A. L. Greer, and G. B. Stephenson, editors, *Thermodynamics and Kinetics of Phase Transformations*, volume 398, pages 425–437, 1996.
- [43] P. R. Rios and E. Villa. Transformation kinetics for inhomogeneous nucleation. *Acta Materialia*, 57(4):1199–1208, 2009.
- [44] E. Villa and P.R. Rios. Transformation kinetics for surface and bulk nucleation. *Acta Materialia*, 58(4):2752–2768, 2010.
- [45] K. Marthinsen. Repeated grain boundary and grain corner nucleated recrystallization in one- and two-dimensional grain structures. *Modelling and Simulation in Materials Science and Engineering*, 4:87–100, 1996.

- [46] K. Marthinsen and N. Ryum. Transformation kinetics and microstructure for grain boundary nucleated recrystallization in two dimensions. *Acta Materialia*, 45:1127–1136, 1997.
- [47] J. M. Rickman, W. S. Tong, and K. Barmak. Impact of heterogeneous boundary nucleation on transformation kinetics and microstructure. *Acta Materialia*, 45(3):1153–1166, 1997.
- [48] W. S. Tong, J. M. Rickman, and K. Barmak. Impact of boundary nucleation on product grain size distribution. *Journal of Materials Research*, 12:1501–1507, 1997.
- [49] R. L. Goetz and V. Seetharaman. Static recrystallization kinetics with homogeneous and heterogeneous nucleation using a cellular automata model. *Metallurgical and Materials Transactions A*, 29A:2307–2321, 1998.
- [50] G. Kugler and R. Turk. Study of the influence of initial microstructure topology on the kinetics of static recrystallization using a cellular automata model. *Computational Materials Science*, 37:284–291, 2006.
- [51] A. Almansour, K. Matsugi, T. Hatayama, and O. Yanagisawa. Modeling of growth and impingement of spherical grains. *Materials Transactions JIM*, 37(10):1595–1601, 1996.
- [52] P. Uebele and H. Hermann. Computer simulation of crystallization kinetics with non-Poisson distributed nuclei. *Modelling and Simulation in Materials Science and Engineering*, 4:203–214, 1996.
- [53] M. Tomellini and M. Fanfoni. Impingement factor in the case of phase transformations governed by spatially correlated nucleation. *Physical Review B*, 78(1):014206, 2008.
- [54] M. J. Starink and A.-M. Zahra. Kinetics of isothermal and non-isothermal precipitation in an al-6 at.% si alloy. *Philosophical Magazine A*, 77(1):187–199, 1998.
- [55] J. B. Austin and R. L. Rickett. Kinetics of the decomposition of austenite at constant temperature. *Trans. Am. Inst. Min. Metall. Eng.*, 135:396–415, 1939.
- [56] K. Marthinsen, O. Lohne, and E. Nes. The development of recrystallization microstructures studied experimentally and by computer simulation. *Acta Metallurgica*, 37:135–145, 1989.

Bibliography

- [57] M. R. Riedel and S. Karato. Microstructural development during nucleation and growth. *Geophysical Journal International*, 125:397–414, 1996.
- [58] M. P. Anderson, G. S. Grest, and D. J. Srolovitz. Computer simulations of normal grain growth in three dimensions. *Philosophical Magazine B*, 59:293–329, 1989.
- [59] W. Yu, C. D. Wright, S. P. Banks, and E. J. Palmiere. Cellular automata method for simulating microstructure evolution. *IEE Proceedings – Science Measurement And Technology*, 150(5):211–213, September 2003.
- [60] F. J. Humphreys and M. Hatherly. *Recrystallization and Related Annealing Phenomena*. Elsevier, Amsterdam, 2nd edition, 2004.
- [61] E. A. Jäggle and E. J. Mittemeijer. Simulation of the kinetics of grain-boundary nucleated phase transformations. *Solid State Phenomena*, 172-174:1128–1133, 2011.
- [62] J. Sietsma and S. van der Zwaag. A concise model for mixed-mode phase transformations in the solid state. *Acta Materialia*, 52(14):4143–4152, 2004.
- [63] K. Fan, F. Liu, X. Liu, Y. Zhang, G. Yang, and Y. Zhou. Modeling of isothermal solid-state precipitation using an analytical treatment of soft impingement. *Acta Materialia*, 56(16):4309–4318, 2008.
- [64] M. Hillert and L. Höglund. Mobility of alpha/gamma phase interfaces in fe alloys. *Scripta Materialia*, 54(7):1259–1263, 2006.
- [65] R. Bauer, E. A. Jäggle, W. Baumann, and E. J. Mittemeijer. Kinetics of the allotropic hcp-fcc phase transformation in cobalt. *Philosophical Magazine*, 91:437–457, 2011.
- [66] C. Bos, F. Sommer, and E. J. Mittemeijer. A kinetic monte carlo method for the simulation of massive phase transformations. *Acta Materialia*, 52(12):3545–3554, 2004.
- [67] C. Bos, F. Sommer, and E. J. Mittemeijer. An atomistic analysis of the interface mobility in a massive transformation. *Acta Materialia*, 53(20):5333–5341, 2005.

- [68] C. Bos, F. Sommer, and E. J. Mittemeijer. Multi-lattice kinetic monte carlo simulation of interphase kinetics for an iron fcc to bcc transformation. *Modelling and Simulation in Materials Science and Engineering*, 14(2):273–282, 2006.
- [69] C. Bos, F. Sommer, and E. J. Mittemeijer. Atomistic study on the activation enthalpies for interface mobility and boundary diffusion in an interface-controlled phase transformation. *Philosophical Magazine*, 87(16-17):2245–2262, 2007.
- [70] W. H. Press, B. P. Flannery, S. A. Teukolsky, and W. T. Vetterling. *Numerical Recipes*. Cambridge University Press, 1986.
- [71] E. A. Jäggle and E. J. Mittemeijer. The kinetics of grain-boundary nucleated phase transformations: Simulation and modelling. *Acta Materialia*, 59:5775–5786, 2011.
- [72] W. G. Burgers. *Rekristallisation, Verformter Zustand und Erholung*. Akademische Verlags-Gesellschaft, Leipzig, 1941.
- [73] P. Cotterill and P. R. Mould. *Recrystallization and grain growth in metals*. Surrey University Press, London, 1976.
- [74] Y. Bréchet and G. Martin. Nucleation problems in metallurgy of the solid state: recent developments and open questions. *Comptes Rendus Physique*, 7:959–976, 2006.
- [75] R. D. Doherty. Nucleation processes in recrystallization: History and current status. In J. M. Howe, D. E. Laughlin, J. K. Lee, U. Dahmen, and W. A. Soffa, editors, *Solid-to-Solid Phase Transformations in Inorganic Materials*, volume 1. The Minerals, Metals & Materials Society, 2005.
- [76] T. O. Sætre, O. Hunderi, and E. Nes. Computer simulation of primary recrystallization microstructures: The effects of nucleation and growth kinetics. *Acta Metallurgica*, 34:981–987, 1986.
- [77] H. S. Zurob, Y. Bréchet, and J. Dunlop. Quantitative criterion for recrystallization nucleation in single-phase alloys: Prediction of critical strains and incubation times. *Acta Materialia*, 54:2983–3990, 2006.
- [78] A. Brahme, J. M. Fridy, H. Weiland, and A. D. Rollett. Modeling texture evolution during recrystallization in aluminum. *Modelling and Simulation in Materials Science and Engineering*, 17(1):015005, 2009.

Bibliography

- [79] E. Fjeldberg and K. Marthinsen. A 3D Monte Carlo study of the effect of grain boundary anisotropy and particles on the size distribution of grains after recrystallisation and grain growth. *Computational Materials Science*, 48:267, 2010.
- [80] Y. B. Chun, S. L. Semiatin, and S. K. Hwang. Monte Carlo modeling of microstructure evolution during the static recrystallization of cold-rolled, commercial-purity titanium. *Acta Materialia*, 54:6373–3689, 2006.
- [81] R. Bauer, E. Bischoff, and Mittemeijer E. J. Precipitation of Co from supersaturated Au₉₀Co₁₀: Microstructure and kinetics. *International Journal of Materials Research*, 102(8):1027–1041, 2011. Accepted for publication in the *International Journal of Materials Research*.
- [82] R. A. Vandermeer and D. Juul Jensen. Quantifying recrystallization nucleation and growth kinetics of cold-worked copper by microstructural analysis. *Metallurgical and Materials Transactions A*, 26A:2227–2235, 1995.
- [83] D. Juul Jensen. Growth rates and misorientation relationships between growing nuclei/grains and the surrounding deformed matrix during recrystallization. *Acta Metallurgica et Materialia*, 11:4117–4129, 1995.
- [84] R. A. Vandermeer and D. Juul Jensen. Effects of nuclei clustering on recrystallization kinetics. *Materials Science Forum*, 467–470:193–196, 2004.
- [85] D. P. Field, L. T. Bradford, M. M. Nowell, and T. M. Lillo. The role of twins during recrystallization of Cu. *Acta Materialia*, 55:4233–4241, 2007.
- [86] F. Scholz and E. Woldt. Ideas for a new kinetic model of the recrystallization of copper based on the experimental determination of nucleation and growth rate. In J. V. Carstensen, T. Leffers, T. Lorentzen, O. B. Pedersen, B. F. Sørensen, and G. Winther, editors, *Proceedings of the 19th Risø Symposium on Materials Science*. Risø National Laboratory, Roskilde, Denmark, 1998.
- [87] E. Woldt. New kinetic model for primary recrystallization of pure metals. *Metallurgical and Materials Transactions A*, 32A:2465–2473, 2001.

- [88] E. Woldt and D. Juul Jensen. Recrystallization kinetics in copper: Comparison between techniques. *Metallurgical and Materials Transactions A*, 26A:1717–1724, 1995.
- [89] N. Hansen, T. Leffers, and J. K. Kjems. Recrystallization kinetics in copper investigated by *in-situ* texture measurements by neutron diffraction. *Acta Metallurgica*, 29:1523–1533, 1981.
- [90] A. M. Wusatowska-Sarnek, H. Miura, and T. Sakai. Influence of deformation temperature on microstructure evolution and static recrystallization of polycrystalline copper. *Materials Transactions JIM*, 42:2452–2459, 2001.
- [91] L. Blaz and P. Kwapisinski. Simple mathematical model for prediction of recrystallization in copper. *Archives of Metallurgy and Materials*, 54:161–170, 2009.
- [92] Y. Amouyal, S. V. Divinski, L. Klinger, and E. Rabkin. Grain boundary diffusion and recrystallization in ultrafine grain copper produced by equal channel angular pressing. *Acta Materialia*, 56:5500–5513, 2008.
- [93] D. P. Field, M. M. Nowell, P. Triverdi, S. I. Wright, and T. M. Lillo. Local orientation gradient and recrystallization of deformed copper. *Solid State Phenomena*, 105:157–162, 2005.
- [94] B. Hutchinson, S. Jonsson, and L. Ryde. On the kinetics of recrystallization in cold worked materials. *Scripta Metallurgica*, 23:671–686, 1989.
- [95] M. J. Luton, R. A. Petrovic, and J. J. Jonas. Kinetics of recovery and recrystallization in polycrystalline copper. *Acta Metallurgica*, 28:729–743, 1980.
- [96] G. Benchabane, Z. Boumerzoug, I. Thibon, and T. Gloriant. Recrystallization of pure copper investigated by calorimetry and microhardness. *Materials Characterization*, 59:1425–1428, 2008.
- [97] F. Häßner. *Thermal Analysis in Metallurgy*, chapter Calorimetric Investigation of Recovery and Recrystallization Phenomena, pages 233–257. The Minerals, Metals and Materials Society, 1992.
- [98] M. J. Starink and A.-M. Zahra. Determination of the transformation exponent s from experiments at constant heating rate. *Thermochimica Acta*, 298:179–189, 1997.

Bibliography

- [99] T. Furu, K. Marthinsen, and E. Nes. Modelling recrystallisation. *Materials Science and Technology*, 6:1093–1102, 1990.
- [100] A. D. Rollett, D. J. Srolovitz, R. D. Doherty, and M. P. Anderson. Computer simulation of recrystallization in non-uniformly deformed metals. *Acta Metallurgica*, 37:627–639, 1989.
- [101] F. Häßner and K. Sztwiertina. Some microstructural aspects of the initial stage of recrystallization of highly rolled pure copper. *Scripta Metallurgica*, 27:1545–1550, 1992.
- [102] G. Bäro and H. Gleiter. The formation of annealing twins. *Zeitschrift für Metallkunde*, 63:661–663, 1972.
- [103] A. Berger, P.-J. Willbrandt, F. Ernst, U. Klement, and P. Haasen. On the generation of new orientations during recrystallization. *Progress in Materials Science*, 32:1–95, 1988.
- [104] F. J. Humphreys. Grain and subgrain characterisation by electron backscatter diffraction. *Journal of Materials Science*, 36:3833–3854, 2001.
- [105] E. E. Underwood. *Quantitative Stereology*. Addison-Wesley Publishing Company, Reading, MA, 1970.
- [106] R. A. Vandermeer and D. Juul Jensen. Microstructural path and temperature dependence of recrystallization in commercial aluminium. *Acta Materialia*, 49:2083–2094, 2001.
- [107] U. F. Kocks, C. N. Tomé, and H.-R. Wenk. *Texture and Anisotropy*. Cambridge University Press, Cambridge, UK, 1998.
- [108] M. Miodownik, A. W. Godfrey, E. A. Holm, and D. A. Hughes. On boundary misorientation distribution functions and how to incorporate them into three-dimensional models of microstructural evolution. *Acta Materialia*, 47(9):2661, 1999.
- [109] J. K. Mackenzie. Second paper on statistics associated with the random disorientation of cubes. *Biometrika*, 45:229–240, 1958.
- [110] G. Gottstein and L. S. Shvindlerman. *Grain boundary migration in metals*. CRC Press, Boca Raton, FL, 2nd edition, 2010.
- [111] E. A. Jäggle and E. J. Mittemeijer. Interplay of kinetics and microstructure in the recrystallisation of pure copper: comparing mesoscopic simulations and experiments. Submitted for publication.

- [112] D. J. Srolovitz, G. Grest, and M. P. Anderson. Computer-simulation of recrystallization. 1. homogeneous nucleation and growth. *Acta Metallurgica*, 34(9):1833, 1986.
- [113] Y. S. Seo, Y. B. Chun, and S. K. Hwang. A 3D Monte-Carlo simulation study on recrystallization kinetics in Zr with hypothetical stored energy gradients. *Computational Materials Science*, 43:512, 2008.
- [114] Y. Suwa, Y. Saito, and H. Onodera. Phase-field simulation of recrystallization based on the unified subgrain growth theory. *Computational Materials Science*, 44:286–295, 2008.
- [115] D. Raabe and R. Becker. Coupling of a crystal plasticity finite-element model with a probabilistic cellular automaton for simulating primary static recrystallization in aluminium. *Modelling and Simulation in Materials Science and Engineering*, 8(4):445, 2000.
- [116] B. Radhakrishnan, G. Sarma, and T. Zacharia. Modeling the kinetics and microstructural evolution during static recrystallization – Monte Carlo simulation of recrystallization. *Acta Materialia*, 46(12):4415–4433, 1998.
- [117] T. Takaki and Y. Tomita. Static recrystallization simulations starting from predicted deformation microstructure by coupling multi-phase-field method and finite element method based on crystal plasticity. *International Journal of Mechanical Sciences*, 52(2):320, 2010.
- [118] E. A. Jäggle and E. J. Mittemeijer. The kinetics of and the microstructure induced by the recrystallisation of copper. *Metallurgical and Materials Transactions A*, 2011. In press.
- [119] D. Juul Jensen. Simulation of recrystallization microstructures and textures: Effects of preferential growth. *Metallurgical and Materials Transactions A*, 28A:15–25, 1997.
- [120] D. Weygand, Y. Bréchet, and J. Lepinoux. Mechanisms and kinetics of recrystallisation: A two dimensional vertex dynamics simulation. *Interface Science*, 9(3-4):311, 2001.
- [121] K. G. F. Janssens. Random grid, three-dimensional, space-time coupled cellular automata for the simulation of recrystallization and grain growth. *Modelling and Simulation in Materials Science and Engineering*, 11(2):157, 2003.

Bibliography

- [122] C. Bos, M. Mecozzi, and J. Sietsma. A microstructure model for recrystallisation and phase transformation during the dual-phase steel annealing cycle. *Computational Materials Science*, 48:692–699, 2010.
- [123] E. A. Holm, M. A. Miodownik, and A. D. Rollett. On abnormal subgrain growth and the origin of recrystallization nuclei. *Acta Materialia*, 51:2701–2716, 2003.
- [124] A. Getis and B. Boots. *Models of Spatial Processes*. Cambridge University Press, Cambridge, UK, 1978.
- [125] V. Marx, F. Reher, and G. Gottstein. Simulation of primary recrystallization using a modified three-dimensional cellular automaton. *Acta Materialia*, 47(4):1219–1230, 1999.
- [126] F. Sebilliau and H. Bibring. The allotropic transformation of cobalt. In *Symposium on the Mechanism of Phase Transformations in Metals*, number 18 in The Institute of Metals Monograph and Rep. Series, page 209, London, 1956.
- [127] *Cobalt Monograph*. Centre d’Information du Cobalt, Brussels, 1960.
- [128] H. T. Hesemann, P. Müllner, O. Kraft, and E. Arzt. *Journal de Physique IV*, 112:107, 2003.
- [129] R. Hultgren, P. D. Desai, and D. T. Hawkins. *Selected Values of the Thermodynamic Properties of the Elements*. American Society of Metals, Ohio, 1973.
- [130] O. H. Knacke. *Thermochemical Properties of Inorganic Substances*. Springer, Berlin, 1991.
- [131] A. T. Dinsdale. *Calphad*, 15:317, 1991.
- [132] J. O. Nelson and C. J. Altstetter. *Trans. Metall. Soc AIME*, 230:1577, 1964.
- [133] A. Munier, J. E. Bidaux, R. Schaller, and C. Esnouf. *Journal of Materials Research*, 5:769, 1990.
- [134] Z. H. Kuang, J. X. Zhang, X. H. Zhang, K. F. Liang, and P. C. W. Fung. *Scripta Materialia*, 42:795, 2000.
- [135] E. Votava. *Journal of the Institute of Metals*, 90:129, 1961.

- [136] H. T. Hesemann, P. Müllner, and E. Arzt. *Scripta Materialia*, 44:25, 2001.
- [137] O. S. Edwards and H. Lipson. *Journal of the Institute of Metals*, 69:177, 1943.
- [138] E. A. Owen and D. Madoc Jones. *Proc. Phys. Soc. London Sec. B*, 67:456, 1954.
- [139] J. Y. Huang, Y. K. Wu, and H. Q. Ye. *Acta Metallurgica*, 44:1201, 1996.
- [140] T. Ericsson. *Acta Metallurgica*, 14:853, 1966.
- [141] T. Waitz and H. P. Karnthaler. *Acta Materialia*, 837, 1997.
- [142] J. B. Hess and C. S. Barrett. *Journal of the Institute of Metals*, 4:645, 1952.
- [143] G. B. Olson and M. Cohen. *Metallurgical Transactions A*, 7A:1897, 1976.
- [144] E. J. Mittemeijer and F. Sommer. *Zeitschrift für Metallkunde*, 93:352, 2002.
- [145] W. Baumann, A. Leineweber, and E. J. Mittemeijer. *Intermetallics*, 19:526, 2011.
- [146] A. T. W. Kempen, F. Sommer, and E. J. Mittemeijer. *Journal of Materials Science*, 37:1321, 2002.
- [147] A. T. W. Kempen, F. Sommer, and E. J. Mittemeijer. *Acta Materialia*, 50:1319, 2002.
- [148] H. Nitsche, F. Sommer, and E. J. Mittemeijer. *Metallurgical and Materials Transactions A*, 37A:621, 2006.
- [149] H. Nitsche. *Kinetics of Crystallization in Amorphous Alloys; Nucleation and Growth*. PhD thesis, University of Stuttgart, June 2005.
- [150] H. Nitsche, F. Sommer, and E. J. Mittemeijer. *Journal of Non-Crystalline Solids*, 351:3760, 2005.
- [151] F. Liu, F. Sommer, and E. J. Mittemeijer. *Acta Materialia*, 52:3207, 2004.
- [152] A. T. W. Kempen, F. Sommer, and E. J. Mittemeijer. *Acta Materialia*, 50:3545, 2002.
- [153] Y. C. Liu, F. Sommer, and E. J. Mittemeijer. *Acta Materialia*, 51:507, 2003.

- [154] Y. C. Liu, F. Sommer, and E. J. Mittemeijer. *Acta Materialia*, 54:3383, 2006.
- [155] A. H. Cottrell. *The Mechanical Properties of Matter*. John Wiley & Sons, New York, 1964.
- [156] O. Blaschko. *Materials Science and Engineering A*, A127:257, 1990.
- [157] P. Villars and L. D. Calvert. *Pearson's Handbook of Crystallographic Data for Intermetallic Phases 1*. ASM International, Materials Park, OH, 1997.
- [158] M. Lin, G. B. Olson, and M. Cohen. *Metallurgical Transactions A*, A23:2987, 1992.
- [159] G. W. H. Höhne, W. F. Hemminger, and H.-J. Flammersheim. *Differential Scanning Calorimetry*. Springer-Verlag, Berlin, 2003.
- [160] International Centre of Diffraction Data. Newton Square, PA, 1997–2007.
- [161] F. Liu, S. J. Song, F. Sommer, and E. J. Mittemeijer. *Acta Materialia*, 57:6176, 2009.
- [162] J. A. Nelder and R. Mead. *Comput. J.*, 308, 1965.
- [163] J. F. Frost and M. F. Ashby. *Deformation-Mechanism Maps*. Pergamon Press, Oxford, 1982.
- [164] J. E. Dorn. *Mechanical Behavior of Materials at elevated Temperatures*. McGraw-Hill, New York, 1961.
- [165] F. Lecroisey and A. Pineau. *Metallurgical Transactions A*, 3:387, 1972.

List of Publications

1. E. A. Jäggle, E. J. Mittemeijer: Predicting microstructures from phase transformation kinetics: The case of isochronal heating and cooling from a super-saturated matrix. *Modelling and Simulation in Materials Science and Engineering*, **18(6)**:065010, 2010. (Chapter 2 of this thesis)
2. E. A. Jäggle, E. J. Mittemeijer: Simulation of the kinetics of grain-boundary nucleated phase transformations. *Solid State Phenomena*, **172-174**:1128, 2011. (Chapter 3 of this thesis)
3. E. A. Jäggle, E. J. Mittemeijer: The kinetics of grain-boundary nucleated phase transformations: Simulation and modelling. *Acta Materialia*, **59**:5775, 2011. (Chapter 4 of this thesis)
4. E. A. Jäggle, E. J. Mittemeijer: Kinetics of interface-controlled phase transformations: atomistic and mesoscopic simulations. *International Journal of Materials Research*, **102(7)**:837, 2011. (Chapter 5 of this thesis)
5. E. A. Jäggle, E. J. Mittemeijer: The kinetics of and the microstructure induced by the recrystallisation of copper. *Metallurgical and Materials Transactions A*, 2011. In press. (Chapter 6 of this thesis)
6. E. A. Jäggle, E. J. Mittemeijer: Interplay of kinetics and microstructure in the recrystallisation of pure copper: comparing mesoscopic simulations and experiments. Submitted to *Metallurgical and Materials Transactions A*, 2011. (Chapter 7 of this thesis)
7. R. Bauer, E. A. Jäggle, W. Baumann, E. J. Mittemeijer: Kinetics of the allotropic hcp-fcc phase transformation in cobalt. *Philosophical Magazine* **91(3)**:437, 2011. (Chapter 8 of this thesis)

Danksagung

Die vorliegende Arbeit wurde am Institut für Materialwissenschaft der Universität Stuttgart und am Max-Planck-Institut für Intelligente Systeme (ehemals Max-Planck-Institut für Metallforschung), Stuttgart, angefertigt. An dieser Stelle möchte ich all denen danken, die zum Gelingen dieser Arbeit beigetragen haben.

An erster Stelle möchte ich mich bei Herrn Prof. Dr. Ir. E. J. Mittemeijer, meinem Doktorvater, für die Aufnahme in seine Abteilung und die Überlassung des Themas bedanken. In den über sechs Jahren in denen ich als wissenschaftliche Hilfskraft, als Diplomand und schliesslich als Doktorand Mitglied seiner Abteilung war hat er stets viel Zeit und Energie aufgewandt um mich gutes wissenschaftliches Arbeiten (sowie den korrekten Gebrauch der englischen und manchmal auch der niederländischen Sprache) zu lehren. Für diese Lektionen, die Freiheit, meine Arbeit zu einem grossen Teil selbst gestalten zu können, sowie für die immer freundliche und konstruktive Zusammenarbeit in vielen Besprechungen möchte ich mich herzlich bedanken.

Herrn Prof. Dr.-Ing. C. Miede danke ich für die freundliche Übernahme des Mitberichts, sowie Herrn Prof. Dr. T. Schleid für die Bereitschaft den Prüfungsvorsitz zu übernehmen.

Eine Doktorarbeit ist ohne die Unterstützung von Kollegen nicht möglich. Für ihre ständige Diskussions- und Hilfsbereitschaft danke ich vor allem Bastian Rheingans, Sairam Meka und Rico Bauer, aber auch allen anderen Kollegen der Abteilung Mittemeijer. Gemeinsam mit allen Mitarbeitern des Instituts sorgten sie stets für eine konstruktive und angenehme Arbeitsatmosphäre.

Zu guter Letzt möchte ich meiner Frau und meiner ganzen Familie herzlich für ihre beständige Unterstützung und ihren Rückhalt danken.

—

Meine Dankbarkeit gilt auch Jürgen Köhler, der kurz nach Fertigstellung dieser Arbeit unerwartet verstarb. Wie schon vielen anderen Doktoranden zuvor half Jürgen auch mir auf viele große und kleine Arten und Weisen bei meiner Arbeit. Seine selbstverständliche Hilfsbereitschaft und seine anpackende Art werde ich sehr vermissen.

Curriculum Vitae

Persönliche Angaben:

Name: Eric A. Jägle

geboren am 31. Juli 1982 in Tuttlingen

Schulbildung:

1988–1992: Grund- und Hauptschule Tuttlingen-Möhringen

1992–2001: Otto-Hahn-Gymnasium Tuttlingen, mit dem Abschluss der allgemeinen Hochschulreife

Universitäre Bildung:

2001–2006: Universität Stuttgart, Studiengang Werkstoffwissenschaft mit dem Abschluss Diplom-Ingenieur. Diplomarbeit über das Thema “Kinetik von Phasenumwandlungen unter Lastspannung” bei Prof. Dr. Ir. E. J. Mittemeijer.

2006–2007: University of Cambridge, UK, Studiengang Materials Modelling mit dem Abschluss Master of Philosophy. Masterarbeit über das Thema “Modelling of microstructural banding during transformations in steels” bei Prof. Dr. H. K. D. H. Badheshia.

Promotion:

2007–2011: Max-Planck-Institut für Metallforschung, Stuttgart. Promotion zum Dr. rer. nat. über das Thema “Microstructure development during phase transformations: simulations and experiments” bei Prof. Dr. Ir. E. J. Mittemeijer.